Technical University of Łódź

Department of Microelectronics and Computer Science

Dariusz Makowski

THE IMPACT OF RADIATION ON ELECTRONIC DEVICES WITH THE SPECIAL CONSIDERATION OF NEUTRON AND GAMMA RADIATION MONITORING

WPŁYW PROMIENIOWANIA NA PRACĘ UKŁADÓW ELEKTRONICZNYCH ZE SZCZEGÓLNYM UWZGLĘDNIENIEM POMIARU PROMIENIOWANIA NEUTRONOWEGO I GAMMA

Ph.D Dissertation

Thesis supervisor:
Prof. Andrzej Napieralski

Łódź, 2006

I would like to express my deep gratitude to my supervisor Prof. Andrzej Napieralski for the inspiration and guidance, that helped me immensely in the preparation of this dissertation.

Special thanks are addressed to Dr. Mariusz Grecki, who has encouraged me to take part in the CARE project for his helpful suggestions and long-lasting cooperation.

I would like to thank Dr. Stefan Simrock from DESY for his invaluable comments and constant support.

I would like to express special thanks to Dr. Bhaskar Mukherjee from DESY for his continuous support in the execution of radiation tests, experiments and his precious comments.

Special thanks are addressed to Dr. Grzegorz Jabłoński and Dr. Robert Szczygieł for their valuable remarks and comments regarding the dissertation.

Finally, I would like to express my gratitude to my Parents, who have encouraged me to continue my studies. I would like to greatly appreciate my wife Aleksandra for her patience, support and inspiration.

I acknowledge the support of the European Community-Research Infrastructure Activity under the FP6 "Structuring the European Research Area" program (CARE, contract number RII3-CT-2003-506395), and Polish National Science Council Grant "138/E-370/SPB/6.PR UE/DIE 354/2004-2007"

Contents

1 The influence of radiation on electronics of an accelerator **1**

1.1 The X-ray Free Electron Laser 1

1.1.1 The VUV-FEL - the pilot facility of X-FEL 2

1.1.2 The main control system of the free electron laser 4

1.2 Radiation environment of a linear accelerator 5

1.3 Radiation monitoring in a linear accelerator 6

1.4 Theses 8

2 Influence of radiation on electronic devices **9**

2.1 Gamma-ray damage effects 10

2.1.1 Degradation of MOS transistor parameters 12

2.2 Neutron damage effects 17

2.2.1 Displacement damage in bipolar transistors 20

2.2.2 Displacement damage in MOS transistors 21

2.2.3 Single Event Effects 22

2.3 Conclusions 28

3 Radiation mitigation techniques **30**

3.1 Hardening on the design stage 31

3.1.1 Modification of the crucial technological parameters and circuit's layouts 31

3.1.2 Modification of integrated circuits electrical construction 34

3.2 Shielding 35

3.2.1 Shielding against gamma radiation 35

3.2.2 Shielding against neutrons 36

3.3 Design radiation tolerant circuits and systems 37

3.3.1 Redundancy 37

3.3.2 Error detection and correction 39

3.3.3 Memory scrubbing 41

3.3.4 Reinitialization recovery 42

3.3.5 SEL mitigation . . . 42
3.4 SEU mitigation techniques for FPGA devices . . . 42
3.4.1 Evolutionary fault recovery . . . 43

4 State of the art of the radiation dosimetry 44
4.1 Neutrons and gamma dosimetry . . . 45
4.1.1 Gaseous detectors . . . 45
4.1.2 Semiconductor detectors . . . 49
4.1.3 Scintillators . . . 51
4.1.4 Activation foils . . . 52
4.1.5 Bubble dosimeters . . . 52
4.1.6 Chemical dosimeters . . . 53
4.1.7 Calorimetric dosimeters . . . 53
4.1.8 Thermoluminescent materials . . . 54
4.1.9 Photographic dosimetry . . . 55
4.2 Real-time radiation monitoring systems . . . 56
4.3 Conclusions . . . 56

5 The on-line radiation monitoring system 58
5.1 Requirements for the radiation monitoring system RadMon . . . 58
5.2 The architecture of the RadMon . . . 60

6 Neutron fluence and gamma radiation sensors 62
6.1 SRAM-based neutron detector . . . 62
6.1.1 Radiation sensitivity tests . . . 63
6.1.2 NVRAM-based neutron detector . . . 64
6.1.3 SRAM devices . . . 73
6.1.4 The methods to increase the sensitivity of the neutron sensor . . . 79
6.2 The gamma radiation detector . . . 83
6.3 Conclusions . . . 86

7 RadMon – the rad-tolerant radiation monitoring system 88
7.1 A review of radiation-tolerant readout systems . . . 89
7.1.1 The application of redundancy to design radiation-tolerant systems 89
7.1.2 An application of programmable circuits to design readout system 91
7.1.3 The RadFET readout subsystem . . . 101
7.1.4 The prototype of the RadMon device installed in VUV-FEL . . . 103
7.2 Conclusions . . . 104

8 SUMMARY AND CONCLUSIONS **108**

8.1 Neutron dosimetry 108

8.2 An application of COTS elements to design rad-tolerant devices 110

8.3 The optimal architecture of the neutron fluence sensor 113

9 APPENDICES **116**

9.1 SRAM and NVRAM devices used during the experiments 116

9.2 Americium-Beryllium neuron source 116

9.2.1 A water moderated Americium-Beryllium neuron source 116

9.3 Cesium gamma source 119

Acronyms

ASIC - Application Specific Integrated Circuit
BOX - Buried Oxide
BPSG - BoroPhosphoSilicate Glass
CARE - Coordinated Accelerator Research in Europe
CMOS - Complementary Metal Oxide Semiconductor
COTS - Commercial Off The Shelf
CRAM - Configuration Random Access Memory
DESY - Deutsche Elektronen-Synchrotron
DOOCS - Distributed Object Oriented Control System
DRAM - Dynamic Random Access Memory
DMR - Dual Modular Redundancy
DUT - Device Under Test
ECC - Error Correction Code
EDAC - Error Detection And Correction
FOXFET - Field Oxide Transistor
FPGA - Field Programmable Gate Array
FSM - Finite State Machine
FLASH - Free electron LASer in Hamburg
GA - Genetic Algorithm
GPIO - General Purpose Input-Output
IEL - Ionizing Energy Loss
ILC - International Linear Collider
KERMA – Kinetic Energy Released in Medium
LET – Linear Energy Transfer
LLRF - Low Level Radio Frequency
LUT – Look–Up Table
NIEL – Non–Ionizing Energy Loss
NVRAM – Non–Volatile static Random Access Memory
MOSFET – Metal-Oxide Semiconductor Field-Effect Transistor
PIN – P-Intrinsic-N junction diode

RadMon – Radiation Monitor
RC – Reader Circuit
RISC – Reduced Instruction Set Computer
RS – Reed–Solomon
SASE - Self-Amplification Spontaneous Emission
SEE – Single Event Effect
SM – Sense Mode
SEU – Single Event Upset
SEL – Single Event Latch–up
SET – Single Event Transient
SEFI – Single Event Functional Interrupt
SEB – Single Event Burnout
SEGR – Single Event Gate Rupture
SER – Single Error Rate
SES – Single Event Snapback
SOI – Silicon On Insulator
SOS – Silicon On Sapphire
SPI – Serial Peripheral Interface
SRAM – Static Random Access Memory
STMR – Selective Triple Modular Redundancy
SV – Sensitive Volume
TC – Temperature Coefficient
TESLA - TeV-Energy Superconducting Linear Accelerator
TID – Total Ionizing Dose
TVL – Tenth Value Layer
TMR – Triple Modular Redundancy
TTF – Tesla Test Facility
ZTC – Zero Temperature coefficient Current
UART – Universal Asynchronous Receiver Transmitter
VHDL – Very high speed integrated circuit Hardware Description Language
VUV-FEL – Vacuum Ultraviolet Free Electron Laser
X-FEL – X-ray Free Electron Laser

Introduction

The negative influence of radiation on electronic devices was discovered during above-ground nuclear bomb tests in 1954. A spurious signal and malfunctions in the operation of the measuring equipment utilized during explosion tests were observed. The energy of a nuclear explosive is released in the form of neutrons, gamma rays, alpha particles and electrons. Neutrons are produced because of fission and fusion reactions. Gamma radiation accompanies above-mentioned reactions and is generally produced from the decay of short-lived fission products. Temporary errors are mainly caused by neutron-generated single event effects (SEEs), while gamma radiation is responsible for the permanent destruction because of the modification of crucial parameters of electronic components. Since 1960 further anomalies have been registered in electronic components and systems operating in space. Electronics of satellites were found to be unreliable at that time. Heavy-ions present in space generated soft errors in electronic systems and therefore disturbed the operation of transmitting modules of Explorer 1 in 1958. However, the separation of errors caused by noise and errors generated by radiation was difficult. Finally, data were sent in smaller packets secured using additional correction codes to improve the communication with the satellite.

The occurrence of SEUs on the ground level was observed first time in a 2 kB dynamic random access memory. Malfunctions were not induced because of particles coming from space. SEUs were induced by alpha particles from the decay of trace concentrations of uranium and thorium present in some integrated circuit packaging materials. In that time, IBM noticed a serious problem with memories' reliabilities. IBM group initiated further research to understand the problem better and find a solution. Modelling allows to design a suitable shielding against alpha particles, responsible for the SEU generation. The development of a fabrication technology of microelectronic circuits increased their vulnerability to SEUs. Errors were seen in many applications including space, military and avionics. James Ziegler working for IBM noticed the problem of SUEs induced in commercial devices operating at ground level that were caused by energetic particles originated from space.

The influence of parasitic radiation produced during the operation of high-energy accelerators used for physical experiments and research were also observed when the

electronic control devices were placed together with the main beam pipe inside a single tunnel. Electronics of the recently constructed in DESY free electron laser, called X-FEL, is subjected to the neutron and gamma radiation influence. The on-line monitoring system able to gauge neutron fluence and gamma radiation was required to investigate the radiation environment of Vacuum UltraViolet Free Electron Laser VUV-FEL (and later X-FEL), control radiation levels and help to design a reliable radiation-tolerant electronic system of the laser.

The author participated in the design of the radiation monitoring system and main control hardware dedicated to VUV-FEL within the confines of CARE project.

This thesis reports the work done in the development of a new neutron fluence sensor and a radiation-tolerant readout system. The presented SRAM-based neutron fluence dosimeter is particularly useful to design of a real time monitoring system, whereas the readout system enables its operation in the radioactive environment. The well-known RadFET dosimeter was utilized for gamma radiation measurement. Despite the fact that, the design of the radiation monitoring system is dedicated to VUV-FEL, both the neutron fluence detector and the readout system can be utilised in other applications. The system can be employed to gauge neutron and gamma radiation doses in various accelerators, colliders and detectors used for the analysis of high-energy collisions products.

The thesis is divided into eight chapters. The description of their contents is presented below:

- **Chapter 1:** A short introduction describing the operation of X-FEL and VUV-FEL lasers is gathered in the first chapter. The main problem of the radiation influence on the accelerator control system is presented basing on the SimCon 3.1L controller. The origin of radiation and its real-time monitoring are also discussed.
- **Chapter 2:** Effects of radiation present in a linear accelerator tunnel, i.e. neutrons and gamma radiation, on various electronic components and circuits are discussed in chapter 2. The ionizing, displacement and single event effects are crucial to understand the operation of radiation dosimeters and radiation-tolerant systems.
- **Chapter 3:** The techniques used for the design of radiation-hardened devices and system are presented. Mitigation techniques applied on the design stage were employed to build the radiation tolerant readout system composed exclusively of COTS elements.
- **Chapter 4:** A review of modern radiation gauging methods and devices is given to select the most suitable sensors for neutron and gamma radiation dose measurement.

- **Chapter 5:** The desired architecture of the readout system and applied dosimeters are presented in Chapter 5. Requirements for the radiation monitoring system RadMon are also specified.
- **Chapter 6:** Radiation sensitivity tests of different NVRAM and SRAM devices were carried out to find out a chip that is the most sensible to SEUs. Memories were irradiated from americium-beryllium neutron source, exposed to radiation in Linac II and VUV-FEL tunnels. Suitable techniques were applied to design a dosimeter sensitive enough to measure neutron fluence in the VUV-FEL.
- **Chapter 7:** A few radiation-tolerant readout systems were designed and tested. Systems were irradiated from different sources and therefore the most suitable architecture of the readout system was finally chosen. Systems were constructed using commercially available components and radiation hardening techniques mentioned in Chapter 3.
- **Chapter 8:** Research allows to design a novel neutron fluence detector and design a suitable readout system. Obtained results allow to draw conclusions, which are presented in Chapter 8.

Chapter 1

The influence of radiation on electronics of a linear accelerator

Radiation produced during operation of high-energy accelerators could be detrimental to electronic components and systems used to control the machines. Therefore, electronic systems and power devices utilised by linear accelerators are usually placed in a safe non-radiation area. Hence, two parallel tunnels are usually built: one for the main accelerating modules and another one for control hardware and systems. The International Linear Collider (ILC), based on TeV-Energy Superconducting Linear Accelerator (TESLA) technology, is going to be housed in two separate tunnels. However, a single circular cross-section tunnel is built for the X-ray Free Electron Laser (X-FEL), therefore most of electronic devices used to control the machine are going to be placed in the same vault as the main beam pipe [1, 2]. Thus, devices will be exposed to bremsstrahlung gamma radiation and photoneutrons produced during the operation of a linear accelerator [1-A, 2-A, 3-A].

1.1 The X-ray Free Electron Laser

The European project X-ray Free Electron Laser (X-FEL) is a 4^{th} generation of synchrotron light source capable of producing high-intensity ultra-short wavelength X-ray laser light [3]. The laser produces X-ray flashes in the wavelength range from 0.15 to 1.5 nm that are shorter than 100 femtoseconds. Short-wavelength radiation interacts with matter in different way than visible light of optical lasers. Therefore, application of the X-ray wavelength radiation gives a new opportunity to study electron dynamics of atomic, molecular and cluster targets irradiated at different X-ray wavelengths and power densities [4]. The wide range of scientific applications from many different areas have been proposed including molecular, cluster and plasma physics, material investigations, chemistry, life sciences and non-linear optics [5].

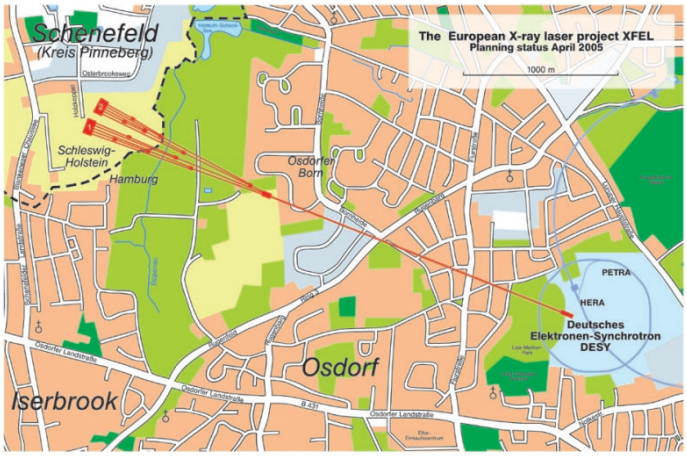

Figure 1.1: *The location of the X-FEL, DESY Hamburg [5].*

The X-ray laser is going to be built in a German national research and accelerator centre Deutsche Elektronen-Synchrotron DESY in Hamburg. The linear accelerator driving X-FEL starts on the DESY site and has a facility in a rural area approximately 3.1 km west-northwest from DESY [6]. The location of the X-FEL facility is presented in Figure 1.1. The laser is composed of an injector, a superconducting electron linear accelerator and undulators. Superconducting radio frequency cavities, based on TESLA technology, are used to accelerate electrons up to approximately 20 GeV [1, 2, 4, 7–10]. The accelerated beam of electrons is passed through undulators to produce coherent light [3]. Extremely short and intense X-ray flashes are emitted because of the self-amplification spontaneous emission (SASE) effect [11]. Finally, the remaining beam, not converted into synchrotron radiation, is damped.

The accelerator operates in a pulsed mode with the maximum repetition rate equal to 10 Hz [4]. A maximum number of bunches in a single bunch train is equal to 4000. Each bunch has a length equal to 80 fs and 1 nC charge.

The whole machine will be housed in a 3.1 km long tunnel, having a cross-section diameter of 5.2 m. Electronic hardware that controls the laser will be installed in the main tunnel. The construction of X-FEL is scheduled for years 2008–2012.

1.1.1 The VUV-FEL - the pilot facility of X-FEL

The successful operation of the first Tesla Test Facility (TTF) accelerator confirmed the suitability of the TESLA technology for FEL applications in 1997. The facility was upgraded and the tunnel was extended up to 260 m within next two years [2, 5]. The pilot facility of X-FEL, called Vacuum UltraViolet Free Electron Laser (VUV-FEL), has already been in operation at DESY. The top view and the sketch of the tunnel layout of the VUV-FEL are depicted in Figure 1.2. The facility enables to carry

a)

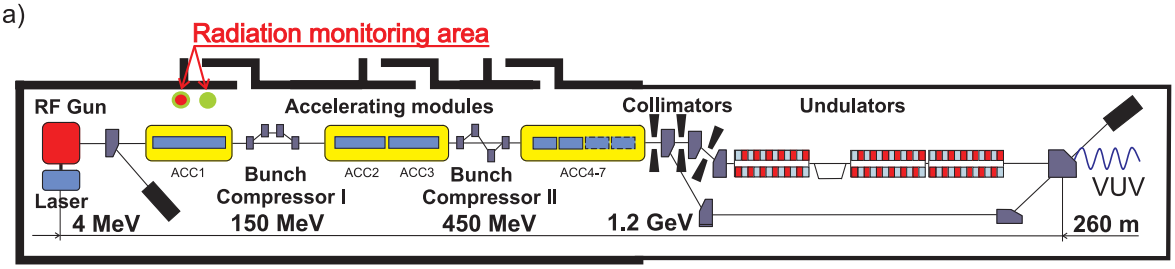

b)

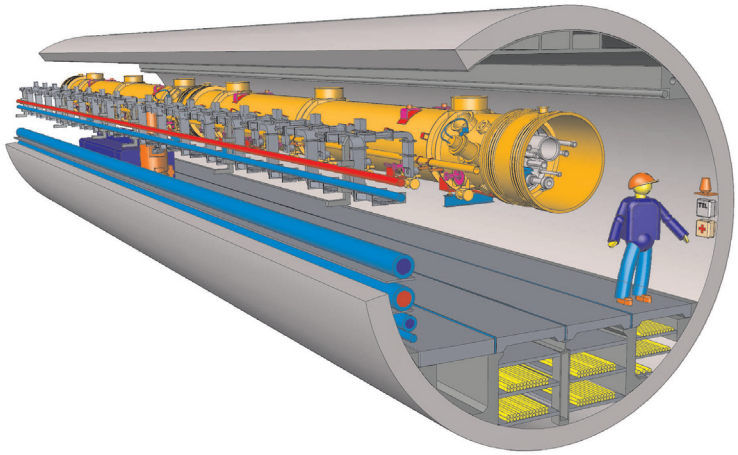

Figure 1.2: *The top view of the VUV-FEL a) and the layout of its tunnel b).*

out initial tests of the control system, investigate the radiation environment of the linear accelerator and execute first physical experiments. The installed cavities, based on TESLA technology, grouped in 5 cryogenic modules (ACC1–ACC5) accelerate the electron beam up to 0.73 GeV, see Figures 1.2 and 1.4. A further increase of the beam energy up to 1.2 GeV is planned when the ACC6 and ACC7 modules will be installed [2, 4]. The 30 m long undulator was installed to supply vacuum ultraviolet radiation from 10 to 200 nm according to the SASE principle [12]. However, the name of the facility was changed into FLASH (Free electron LASer in Hamburg) when the lasing at 13.1 nm was achieved for the first time[1]. The obtained radiation energy was up to 5 µJ using the maximum available energy equal to 0.73 GeV. The further upgrading of the laser is in progress. New cryogenic modules ACC6 and ACC7 that will be equipped with eight high-gradient cavities are going to be installed in the second half of 2006.

[1]The free electron laser facility VUV-FEL in DESY is currently called FLASH, however the VUV-FEL name is used in the thesis.

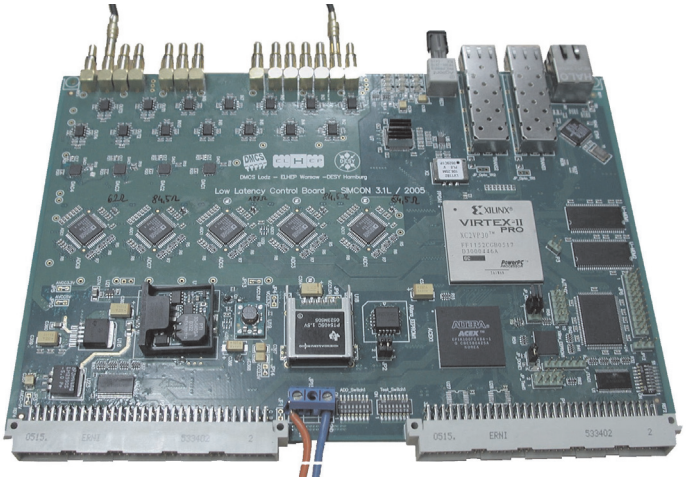

Figure 1.3: *An exemplary FPGA–based control board SimCon 3.1L.*

1.1.2 The main control system of the free electron laser

A powerful digital Low Level Radio Frequency (LLRF) system is required to fulfill sharp demands of the control system that allows for a reliable operation of the accelerator. The RF phase and amplitude stability must be better than 0.01° and 0.1%, respectively [13]. Accelerating cavities are supplied with 1.3 GHz signal produced by 5 MW klystrons controlled by actuators that act on its amplitude and phase. The digital controller detects accelerating field in cavities using pick-up antennas and generates the signal driving klystron [14]. Digital data processing is performed in the control system and therefore the driving signal for the klystron is produced. The distributed control system of the VUV-FEL is composed of 5 subsystems supervising klystrons supplying 40 cavities. Currently, DSP microcontrollers and FPGA devices are used to design a digital LLRF subsystem that is able to supervise eight cavities. A photograph of an exemplary LLRF system built with an application of high-density FPGA circuits is presented in Figure 1.3. The module based on the Xilinx Virtex II pro FPGA is able to collect a signal from eight cavity modules. The complex system utilizes additional digital circuits, like static and dynamic random access memories (SRAMs/DRAMs), Altera FPGA, digital-to-analog (DAC) and analog-to-digital (ADC) converters [4-A]. A VersaModule Eurocard bus (VME) is employed for the communication between the digital controller and a main computer with UltraSPARC processor. The accelerator control system is a distributed device that utilizes various digital and analogue submodules. A single subsystem board should collect signals from 32 cavities in the future, therefore the accelerator driving VUV-FEL will require only two boards. However, the number of control subsystem boards will be enormous for the X-FEL or ILC, see

Machine name	Accelerator length	Number of cavities	Number of subsystem boards
VUV-FEL	130 m	56	7
X-FEL	2.1 km	928	116
ILC	approx. 30 km	approx. 10000	1250

Table 1.1: *Comparison of electronic systems required for various accelerators [2].*

Table 1.1[2] .

Both types of radiation produced in the tunnel can pose a threat to the complex control system. Gamma radiation is mainly responsible for continuous degradation because of total ionizing dose effect (TID), while neutrons cause displacement damage and generate single event effects (SEE). Both types of radiation are presented in Chapter 1.2, whereas their influence on electronic components is described in Chapter 2.

The digital control system must be designed in such a way that it can tolerate errors generated by radiation present in a tunnel. Techniques used to mitigate influence of radiation on electronic devices and systems are presented in Chapter 3.

1.2 Radiation environment of a linear accelerator

A mixed neutron and gamma radiation field is present in the linear accelerator environment. The beam loss pattern in a linear accelerator is difficult to predict because of its strong dependence on machine operation conditions [15]. Therefore, the precise spectra of radiation produced in VUV-FEL are not known.

Radioactive nuclides are mainly generated in high-energy linear accelerator environments because of interactions between the electron beam with cavities, accelerator components and shielding elements[3] [16]. Moreover, electrons accelerated by cavities produced by the dark current from the RF gun are able to gain energy high enough to generate radiation during collisions. However, the major share of radiation comes from the interaction of field emission electrons with walls of the cavity itself [17].

One can distinguish two main types of radiation produced during the operation of high-energy linear accelerators: bremsstrahlung photons and photoneutrons [1-A]. Bremsstrahlung photons have energy in range from zero to the maximum energy of beam particles. Photoneutrons are produced during interactions of bremsstrahlung photons with the structure of the accelerator facility mainly in three different ways:

[2]The amount of the subsystem boards was calculated assuming that one board can supervise eight cavities.

[3]The cavities of the superconducting linacs driving X-FEL or VUV-FEL are produced of pure niobium.

giant dipole resonance (GDR) interactions and decay that dominates in the energy range up to tens of MeV, quasi-deuteron production and decay ($50<E_\gamma>300$ MeV) and intranuclear cascades ($E_\gamma>140$ MeV) [18]. The GDR neutrons with 2 MeV peak energy have a isotropic distribution, while neutrons produced by quasi-deuteron decay and the intranuclear cascade are emitted in the forward direction [18]. The cross-section of GDR reaction is approximately one order of magnitude lower than quasi-deuteron decay and the intranuclear cascade. Moreover, the production of higher energy bremsstrahlung photons is several orders of magnitude lower than the intensity of photons responsible for the GDR cascade [1-A]. Therefore, high energy-photons and GDR photoneutrons dominate in the linear accelerator tunnel such as VUV-FEL. The fluence of neutrons with energy higher than 30 MeV is significantly lower. Additionally, GDR photoneutrons interact with the shielding and concrete walls of the accelerator tunnel and yield a further energy reduction (thermalisation) [5-A].

Therefore, thermal neutrons and neutrons with a peak energy distribution near a few MeV can be observed in the high-energy linear accelerator tunnel, like the above-mentioned VUV-FEL. An exemplary neutron energy spectrum, calculated for a high energy linear accelerator Linac II using MCNP 4A, is presented in Figure 6.2.

1.3 Radiation monitoring in a linear accelerator

Bremsstrahlung gamma radiation and photoneutrons are produced during the operation of high-energy linear accelerators. Therefore, generated radiation could run a risk of radiation damage of electronic devices installed in the accelerator tunnel.

Ionizing radiation continuously damages electronic components because of the total ionizing dose (TID) effect. Non-ionizing particles are responsible for the displacement or non-ionizing energy loss (NIEL) damage. Moreover, neutrons can affect mainly digital components by single event effects (SEEs). Radiation effects on electronic devices are described in Chapter 2.

Knowledge of neutron and gamma doses are crucial to understand and interpret radiation effects on electronic devices dedicated to the operation in the environment of high-energy linear accelerators. Indeed, it is advisable to monitor radiation produced in the VUV-FEL or X-FEL tunnels in real time to estimate the danger and the life-time of electronic components and devices. Additionally, tough safety regulations support the need to control the radiation environment in the tunnel in real-time. The system could be also helpful to choose a suitable place for crates with electronics in the accelerator when the radiation levels are the lowest. The appliance might be also useful to design a correct gamma and neutron shielding.

The radiation monitoring system was designed to enable measuring gamma radia-

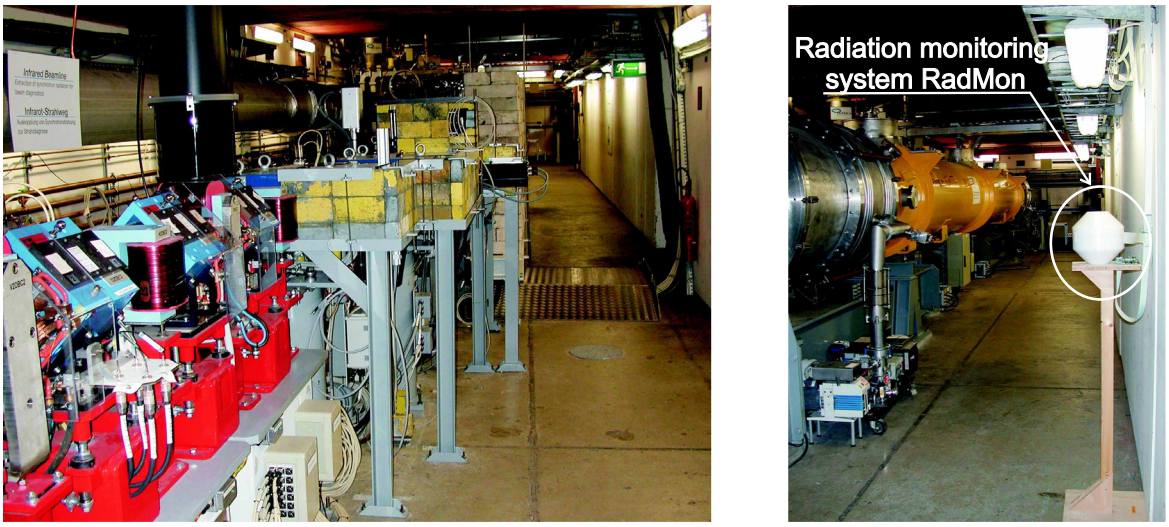

Figure 1.4: *The interior of the VUV-FEL tunnel: the gamma and neutron shielding of the Bunch Compressor II on the left and the accelerating module ACC1 with the accompanying on-line radiation monitoring system RadMon on the right.*

tion and neutron fluence in real-time. The photograph of the VUV-FEL tunnel and a prototype of the radiation monitoring system is shown in Figure 1.4. The system is composed of two dosimeters: neutron fluence and gamma radiation sensors, see Chapter 6. The radiation tolerant system was built to allow a long-term reliable operation in the radiation environment of VUV-FEL and later X-FEL, see Chapter 7. Radiation-hardened components were not used to design the system because of their exorbitant costs. Instead, commercial-of-the-shelf (COTS) devices were employed to design a cost-effective distributed system, which can be installed in various places of the accelerator. The radiation monitoring system may also help to minimize neutron fluence and gamma radiation doses generated during the operation of the linear accelerator.

1.4 Theses

Bearing in mind the presented issues the author would like to prove the following theses:

1. **The commercially available SRAM chip can be used as a calibrated neutron fluence dosimeter.**

2. **The non-volatile version of a random access memory is a suitable solution for an off-line dosimeter that can be competitive with bubble or TLD detectors.**

3. **Commercial electronic circuits that are not dedicated to tolerate radiation-caused malfunctions can be utilized to design cost-effective radiation-tolerant digital circuits when the modified approach to system's design is applied.**

4. **An application of a chained first-input first-output memory structure allows for the design a cost-effective ASIC dedicated to neutron fluence dosimetry.**

Chapter 2

The influence of radiation on electronic devices

Photons and particles in a form of radiation can basically generate two different types of effects on silicon components:

- ionizing effect,
- displacement damage.

Therefore, radiation can modify electrical parameters of the device, deteriorate its characteristics and finally lead to the functional failure of the components or the whole system. Moreover, ionizing particles can produce photocurrent in active regions of devices and provoke upsets, called single event effects (SEEs). The influence of neutrons and gamma radiation on electronic components with the emphasised interactions are depicted in Table 2.1.

Radiation type	**Energy range**	**Main type of interaction**	**Primary effects in Si and SiO_2**	**Secondary effects in Si and SiO_2**
Photons	Low energy	Photoelectric effect	Ionizing phenomena	Displacement damage
	Medium energy	Compton effect		
	High energy	Pair production		
Neutrons	Low energy	Capture and nuclear reaction	Displacement damage	Ionizing phenomena
	High energy	Elastic scattering		

Table 2.1: *Neutron and gamma radiation effects on silicon devices [19, 20].*

High energy incident particles can interact with matter (e.g. silicon or silica) mainly in three different ways:

1. Ionization of the latter through the interaction with shell electrons.
2. Displacement of atoms nucleus, assuming that the incident particle has enough energy.
3. Nuclear reaction with the target nucleus.

The above-mentioned effects can be triggered by different particles. Moreover, all the phenomena can coexist, for example an interacting neutron can first collide with the nucleus creating displacement damage, then generate secondary charged particles and ionize the material, assuming that the secondary particle has enough energy. However, primary particles have higher energy and thus the first effect predominates. Highly energetic and charged particles cause that ionizing dose effect predominates [19]. Therefore, only a small fraction of their energy is utilized for displacement damage. On the other hand neutral particles (neutrons) are mainly responsible for displacement damage or displacement cascades. Therefore, when a high-energy particle interacts with matter, some of its energy is consumed by the ionizing process and the other part by displacement damage. One can define stopping power S of the particle as rate of the energy loss along the path normalized to the material density, see Equation 2.1.

$$S = \frac{1}{\rho}\frac{dE}{dR} = NIEL + IEL, \tag{2.1}$$

where ρ is the mass density of the interacting material, dE/dR is the rate of the energy loss along the path. NIEL corresponds to non-ionizing energy loss and IEL stands for ionizing energy loss. NIEL is usually expressed as a normalised effect of equivalent 1 MeV neutrons.

Devices and electronic components placed in a linear accelerator tunnel, e.g. installed in VUV-FEL or X-FEL, are exposed basically to two types of radiation: bremsstrahlung gamma and photoneutrons. Therefore, the effect of gamma radiation and neutrons on electronic components will be discussed in the following sections.

2.1 Gamma-ray damage effects

This chapter describes the influence of gamma radiation on electronic components. Gamma-ray photons deposit energy in the components mainly by ionization [21]. The energy used for ionizing phenomenon is called the ionizing dose, however the portion of energy absorbed by the circuit during the whole exposure is determined as a total ionizing dose (TID). The ionizing effect can be caused by different kinds of ionizing radiation, e.g. gamma, X-ray, Ultra-Violet radiation or indirectly through secondary recoil particles [22]. The principal ionizing-based damage effects in a bulk material are: enhancement of conductivity through production of excess charge carriers, trapped

charge, electric and magnetic fields and chemical effects [21]. The phenomena connected with the increased conductivity of silicon and trapped charges in silicon dioxide are discussed in present chapter. The effects of radiation on other components can be found in the literature [19, 22–24].

Photons interact with matter, depending on their energy, in at least three different ways [25]:

1. Photoelectric effect.
2. The Compton effect.
3. Electron-positron pairs production.

Photovoltaic effect is triggered by low energy photons, like X-ray. The Compton effect and pairs production occur for higher-energy photons, like gamma radiation. Free electrons produced during ionizing damage, which have enough energy, span to the forbidden gap and create electron-hole pairs. Therefore, the conductivity of the bulk material is temporarily enhanced. Electron-hole pairs can be also produced in the non-conducting structure like silicon dioxide. Energy necessary to produce an electron-hole pair and generation rate for silicon and silicon dioxide are presented in Table 2.2. Generation rate g_0 expresses the ionization capability of unit volume for the given material. The pairs created in conductive or semiconductive materials, for instance

Material	$\mathbf{E}_{ion}$ **[eV]**	$\mathbf{g}_0$ **[electron-hole pairs·Gy^{-1}·cm^{-3}]**
Silicon	3.6	4×10^{15}
Silicon Dioxide	18	8.2×10^{14}

Table 2.2: *The ionisation energy and ionization-induced generation rate for silicon and silica [19].*

silicon, can recombine or diffuse, according to present electrical field. The charge deposited in silicon can provoke one of possible SEE effects, which are described in Chapter 2.2.3. The damage brought about by ionizing radiation is primarily due to the trapping of the charge in SiO_2 and secondarily because of anomalies in the Si/SiO_2 interface. The charge build-up process in an electronic component under a steady dose rate is depicted in Figure 2.1. Incident gamma radiation produces electron-hole pairs in the insulator. A fraction of generated pairs quickly recombines with other carriers. However, only electrons can leave silica instantaneously according to an electric field as a part of a normal circuit operation. The electrons mobility is much higher that holes in silicon dioxide, therefore only a small fraction of holes can move to silicon through the interface. Holes remaining in the insulator result in the charge built up in SiO_2. The amount of charge generated in silica strongly depends on the electric field across the

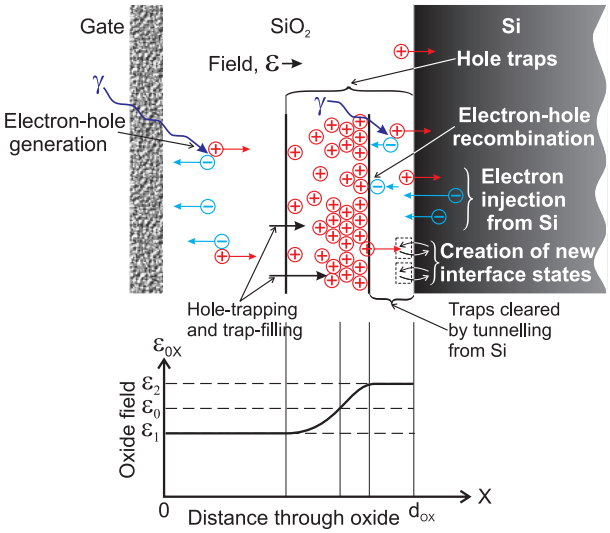

Figure 2.1: *The charge creation process in silicon dioxide, oxide-silicon interface (upper part of the drawing) and the strong disturbance of the electric field in the region of built charge sheet [22].*

oxide during the exposure. Some of the positive traps can recombine, because of the tunneling effect, migrate and drift under the action of an electric field and differences in diffusion. Some of them can partially anneal with time, but others are trapped as electrically active defects. The second effect concerns the rearrangement of the atomic bonds at the oxide-silicon interface and production of new interface states [22]. The trapped charge and created anomalies have a significant influence on the electrical properties of electronic components. A part of generated traps can be located in the nearest vicinity of the Si/SiO_2 interface, therefore they can act as a border traps or slow interface states. Border traps become more important for sub-micron technologies when the silicon dioxide thickness decreases below 5-6 nm [26].

2.1.1 Degradation of MOS transistor parameters

The ionizing radiation effects described in Chapter 2.1 are responsible for the building-up of charge in silica and at Si/SiO_2 interface. This phenomenon results in changing a few important electronic parameters of MOS transistors. The most important parameter of MOS, which can be modified by ionizing radiation, is a threshold voltage V_t. Other parameters affected by gamma radiation are as follows [19]:

- a decrease of transconductance,
- an increase of leakage currents,
- a reduction of drain-source breakdown voltage,
- a deterioration of noise parameters,
- a reduction in surface mobility,

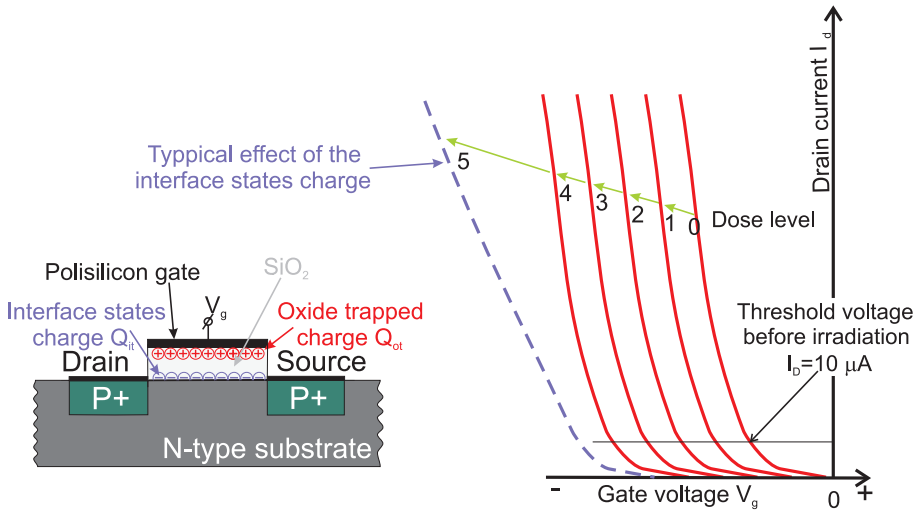

Figure 2.2: *Oxide and oxide-silicon trapped charges in PMOS transistor along with the $I_D - V_G$ curves reflecting shifts in the threshold voltage. The dashed line represents the influence of silicon and oxide-silicon interface anomalies [22].*

- an increase of the surface recombination velocity.

Threshold voltage shift

The change of the threshold voltage for the MOS transistor substantially depends on the electric field in the silicon oxide [27]. Therefore, the biasing voltage of the transistor has a significant influence for generated and trapped charge, e.g. the positive-charged build-up can be attracted to a negatively-biased gate electrode, see Figures 2.2 and 2.3. The ionizing radiation generated charge causes the threshold voltage shift, which can be expressed as the sum of two voltage changes: caused by the increase of the charge in silica Q_{ot} and the interface-trapped charge Q_{it}, see Equation 2.2.

$$\Delta V_{th} = -e \cdot \frac{1}{C_{ox}} \cdot \Delta N_{ot} \pm e \cdot \frac{1}{C_{ox}} \cdot \Delta N_{it}, \tag{2.2}$$

where e is an elementary charge, C_{ox} is an oxide capacitance expressed per unit area, ΔN_{ot} and ΔN_{it} are the densities of oxide-trapped charges and interface states, respectively. The voltage shift caused by the modification of interface states can be positive for p-type MOS transistor and negative for NMOS. Charges trapped in PMOS transistor's oxide and the threshold voltage shifts are exemplified in Figure 2.2. The fraction of holes generated in the oxide layer is trapped as a Q_{ot} and causes the same effect as an application of a negative voltage to gate electrode. The threshold voltage shifts towards the negative gate voltage according to the absorbed dose (the threshold voltage can be measured for the same drain current equal to 10 µA, therefore in order to keep a constant drain current the absolute value of the gate voltage must be increased.

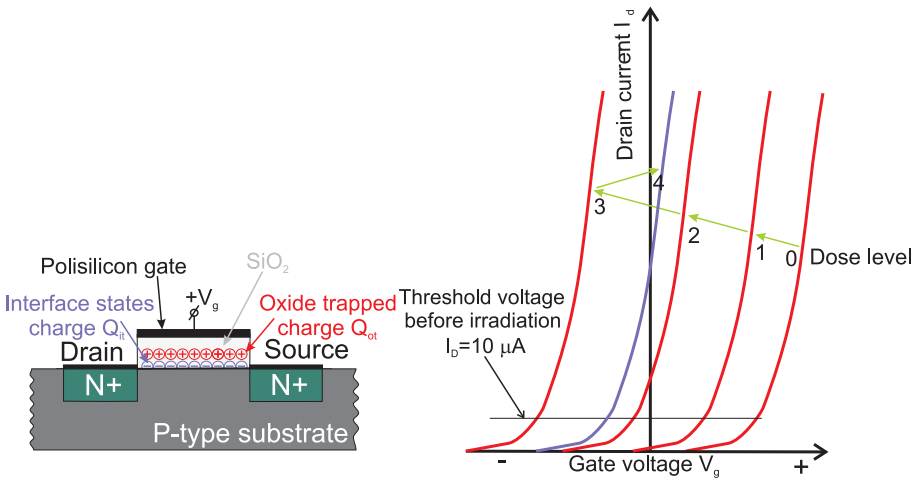

Figure 2.3: *Oxide and oxide-silicon trapped charges in NMOS transistor together with the $I_D - V_G$ curves reflecting shifts in the threshold voltage [22].*

The position of the built-up charge strongly depends on the gate bias voltage, thus the smaller the distance between gate terminal and the charge sheet, the less the additional electric field is observed and less the threshold voltage is shifted. The distance is greater for the PMOS transistor, because of negative biasing, thus PMOS is more radiation resistant than NMOS [21]. The anomalies created in the oxide-silicon interface resulting in the further shift of the threshold voltage and decrease the transistor gain. The influence of the N_{it} is presented in Figure 2.2 as a dashed curve. The positive threshold voltage of the NMOS transistor can be decreased, as well as increased during the exposure. The characteristics presenting the threshold voltage shift are depicted in Figure 2.3. The positive gate bias brings about the move of the charge sheet towards the interface. The threshold voltage in initially decreased as Q_{ot} effect dominates. When enough charge will be accumulated into oxides and oxide-silicon interface, the situation can change and the second effect can start predominating and threshold voltage can be moved towards the positive value.

It should be emphasized that the threshold voltage shift depends mainly on the gate silicon dioxide thickness. Radiation induced V_t shifts are significantly reduced for the oxides thickness lower than 10 nm due to tunneling effect [28].

Decrease of transconductance

The SiO_2 and Si/SiO_2 interface trapped charges result in a change of carriers' mobility in the transistor channel and thus lead to a decrease in its transconductance. This phenomenon depends on densities of trapped charges and can be expressed using Equation 2.3 [29].

$$\mu = \frac{\mu_0}{1 + \alpha_{it}\Delta N_{it} + \alpha_{ot}\Delta N_{ot}}, \tag{2.3}$$

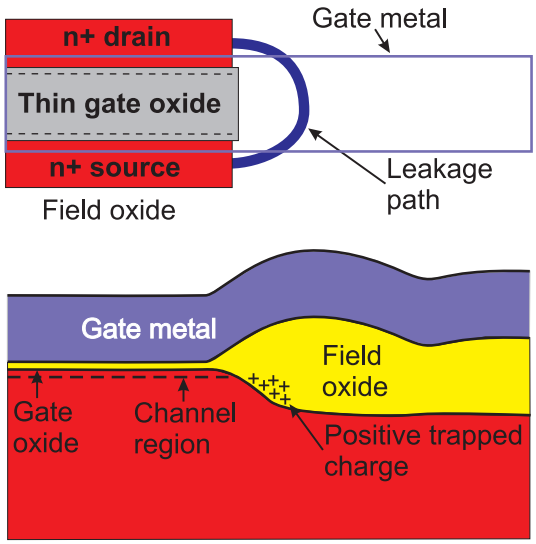

Figure 2.4: *The source-drain leakage path created by built-up charge in oxide [30].*

where α_{it} and α_{ot} are the coefficients describing the effects of oxide-trapped charges and interface states respectively. The density of interface states also causes the increase of the leakage current in the subthreshold region. The decrease of the carriers' mobility has a negative influence on the transistor's conductivity.

An increase of quiescent currents

Modern devices use thick silicon dioxide as spacers and isolation elements. The accumulated charge in the silicon dioxide or the oxide-silicon interface can be the main source of a quiescent current increase. The parasitic effect concerns both CMOS and bipolar devices using SiO_2 isolation. The growth of the leakage current is caused by the build-up charge in lateral oxide structures and results in creation of parasitic channel between drain and source of a NMOS transistor [28]. Hence, a constant current flow between the source and drain can be observed. The sketch of MOS structure with the emphasised drain-source leakage path is presented in Figure 2.4. Moreover, the leakage between different MOS transistors or other electronic parts is also possible. The characteristics presenting an increase of quiescent currents of exemplary CMOS circuits is demonstrated in Figure 2.5. It represents the supply current for a stable state of devices' inputs. The effect is particularly visible for submicron-CMOS devices [31]. This effect alters as well the junction breakdown voltage [32]. Therefore, multiguard structures can be used to enhance the breakdown voltage.

Ionizing-generated charges can also affect the gate oxide stability and breakdown voltages for a thin oxide layer. Oxide leakage current and breakdown voltage decreasing were observed for thin oxide layers (less than 4 nm) and doses above 10 kGy. Radiation

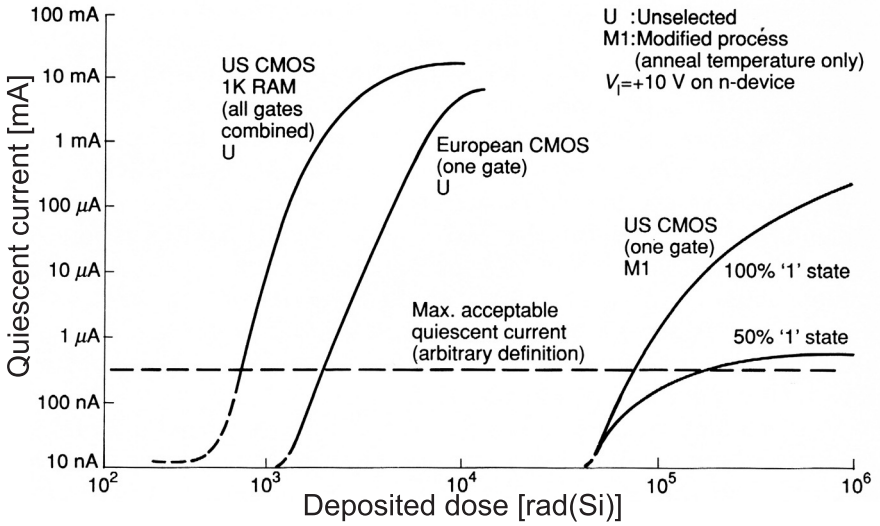

Figure 2.5: *An increase of a quiescent current as a function of absorbed dose for CMOS devices [22].*

induced electrons in silicon dioxide and tunneling effects are mainly responsible for this phenomena [28].

A noise increase, especially 1/f, was correlated with SiO_2 and Si/SiO_2 interface trapped charges [28,33]. The noise measured for n-channel MOS transistor is presented in Figure 2.6. The devices with a 48 nm oxide were fabricated in 3 µm technology (W32 G1916A). The gate voltage of the transistor was connected to 6 V bias during exposure. The characteristics was collected for the pre-irradiated device and after the exposure with four different doses. One can see increasing 1/f noise with the absorbed dose. Three large "spikes" are caused by the power line fundamental and higher harmonics [33].

Recovering of MOS parameters

During the exposure a positive charge trapped in SiO_2 and at Si/SiO_2 interface plays as electrically active defects. The trapped charge is placed in a semi-stable state or even can be trapped very firmly, however its continuous fluctuations can be observed. Moreover, most of the trapped holes undergo an annealing process with time [30, 34, 35]. The annealing is a complex phenomenon, which depends on many parameters: a temperature, trap depth, gate bias voltage, radiation level and dose rate [28]. The external electric field exerts an influence on the charge. The relaxation has usually logarithmic time dependence. The literature gives a few descriptions for an annealing process. The thermal model explains the hole relaxation Q_{ot} through the thermal migration of trapped holes within the oxide to the oxide valence band. The annihilation of trapped holes with tunneled electrons from the substrate can be also seen. The tunnel annealing dominated for lower temperatures, however at temperatures above

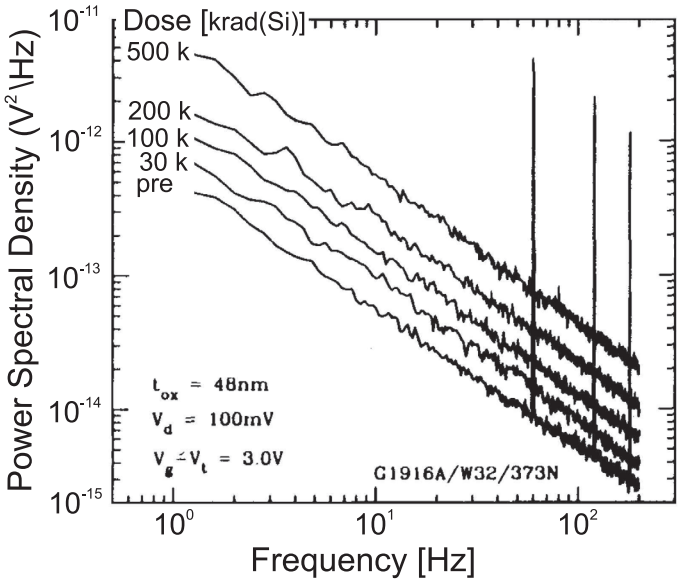

Figure 2.6: *1/f noise spectra as a function of total ionizing dose for W32(G1916A) wafer [33].*

75 °C thermal detrapping becomes more significant [28].

There are two types of annealing that can be distinguished: a high and room temperature. The high temperature process is usually characterized by a high recovery rate. Examples of high-temperature annealing for oxide trapped charge and interface states are presented in Figure 2.7. MOS capacitors were irradiated with X-ray or vacuum UV light. The annealing processes were carried out using 10 minutes steps. Room temperature annealing for different MOS devices is illustrated in Figure 2.8. The devices were irradiated with different doses and the ionizing degradation was rescaled to emphasize the annealing effect. The recovering time is different for devices manufactured in various technologies. The recovery time is short for radiation-hardened MOS with aluminium gate, curve (a), however for ultra-soft PMOS transistor used as a RadFET dosimeter, time is a few orders of magnitude longer. Moreover, another p-channel MOS reveals further degradation with time, curve (e).

2.2 Neutron damage effects

Neutrons are relatively heavy particles, therefore they mainly affect lattice atoms of a semiconductor device through collisions. Neutrons interact with matter in two different ways:

1. Colliding with other particles.
2. Through a capture process.

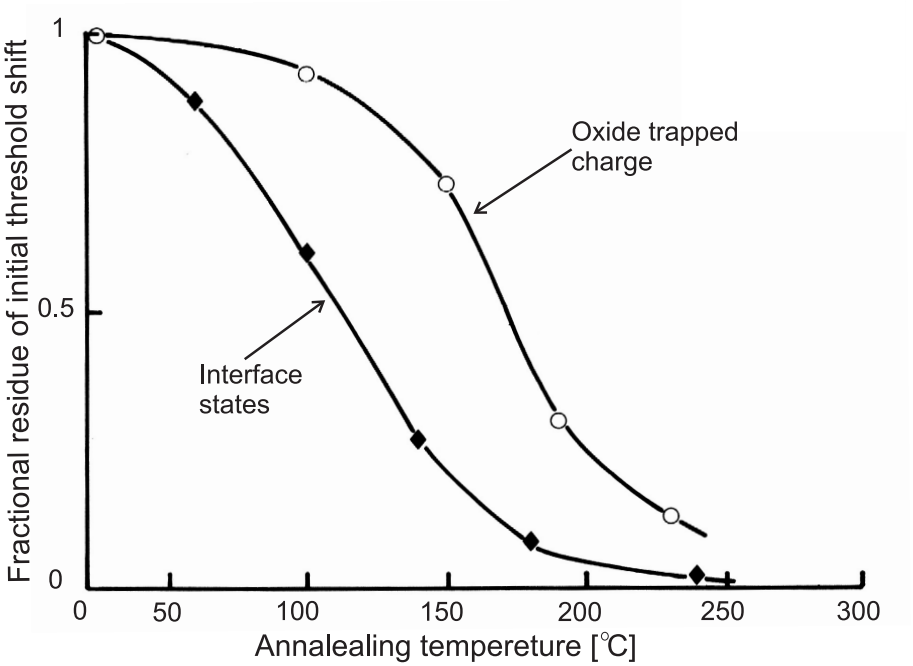

Figure 2.7: *Experimental results of thermal annealing of the shift in threshold voltage [22].*

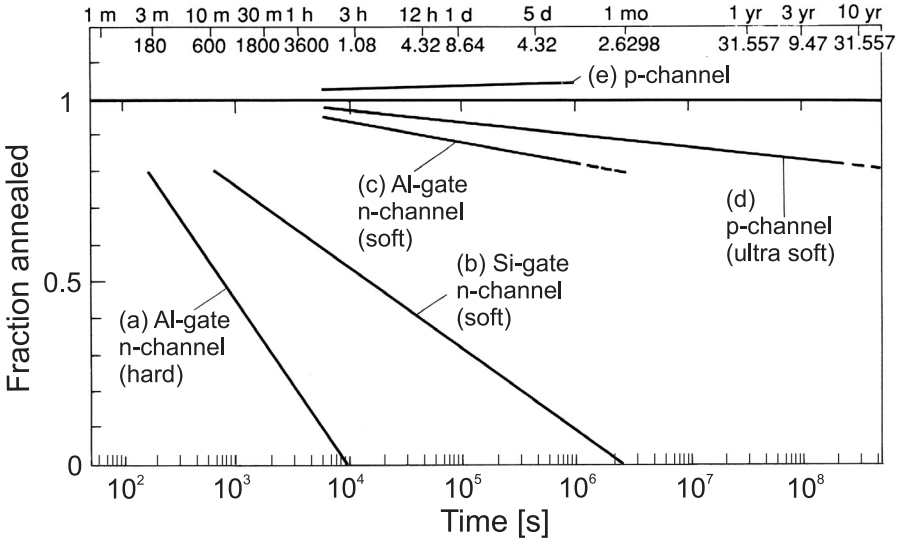

Figure 2.8: *Typical changes in post-radiation annealing for various MOS devices [22].*

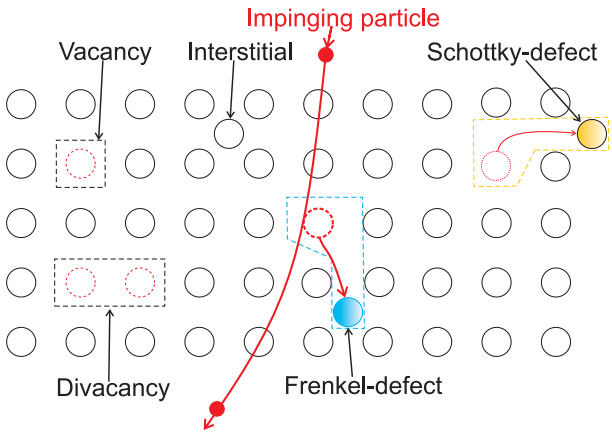

Figure 2.9: *Various intrinsic defects created by atoms displacement [19].*

It should be emphasized that the elastic scattering process predominates for high-energy neutrons and capture effect is more probable for low-energy [19].

An atomic displacement can be compared to a collision between two hard spheres. If the transferred energy is higher than the displacement energy E_d, the lattice atom will be removed from its original position in the lattice and the defect will be created. The recoil atom could be capable of displacing other atoms or producing electron-hole pairs assuming that it has enough energy. For highly energetic particles a cascade of distortions or disruptions of the silicon lattice could be generated.

Various types of displacement defects, like: vacancy, divacancy, interstitial, Schottky and Frenkel defects, are presented in Figure 2.9. Vacancies, interstitial and Frenkel defects are the most probable to appear [19]. Moreover, primary defects are unstable in a room temperature. They have a tendency to migrate, annihilate or induce more complex secondary defects. Extrinsic constituents present in a semiconductor, like impurities or doping atoms, are conducive to form permanent cluster defects in a room temperature [36]. Permanent defect complexes act as a recombination and charge trapping centres and thus the resistivity of the material might be increased [21]. However, mobile vacancies pose a potent recombination agent for trapping minority carriers and therefore reduce their lifetime. Defects responsible for electron trapping are called E defects and H defects behave like hole traps [19]. Displacement damage mainly affect electrical parameters of semiconductor substrates and therefore exert influence on the electrical characteristics of the electronic components.

Even if neutrons are neutral and cannot interact with charged particles in electrical way, they are capable of ionizing atoms mainly in three different ways:

1. Via a previously mentioned collisions and production of recoil products.
2. Production of gamma rays through the de-excitation process of excited atomic nuclei.

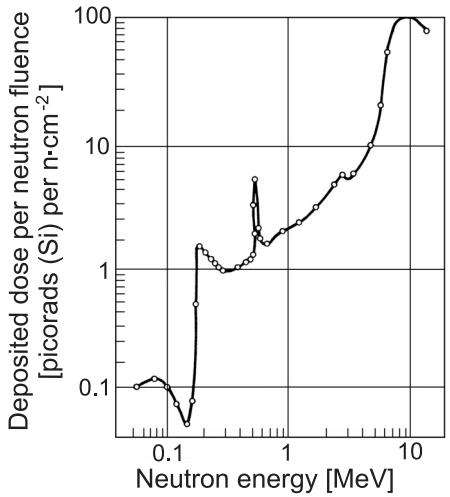

Figure 2.10: *An experimentally determined neutron-induced ionization is silicon [21].*

3. Because of neutron collisions, where the neutron is absorbed by the target atomic nucleus.

The neutron-induced ionization for silicon determined using experimental approach is depicted in Figure 2.10.

Despite the fact that elastic scattering is more probable, neutron can be captured by nuclei through one of the following nuclear reactions: (n,p), (n,α), (n,γ), (n,f) nuclear fission. The electrically neutral neutron can yield ionizing particle through one of the following reactions: He^3(n,p)H^3, B^{10}(n,α)Li^7 [19]. It is worth noting that secondary particles created in such a way, e.g. alpha particles have a high linear energy transfer (LET). Particularly, alpha particles have a short range in silicon, therefore they can deposit their whole energy and ionize significantly the material. The influence of ionizing particles was described in Chapter 2.1.

2.2.1 Displacement damage in bipolar transistors

Charge trapping centres created during the irradiation affect negatively main parameters of the bipolar transistor. Firstly, recombination centres are responsible for decreasing of the minority carriers' lifetime [37]. Accordingly minority carrier's lifetime damage coefficient K_τ can be expressed by Equation 2.4.

$$\Delta\left(\frac{1}{\tau}\right) = \frac{1}{\tau_1} - \frac{1}{\tau_0} = K_\tau \cdot \phi, \tag{2.4}$$

where τ_0 is the minority carrier's lifetime before the irradiation, τ_1 being the minority carrier's lifetime after the irradiation and ϕ corresponds to the particle fluence. The common-emitter current gain β (h_{FE}) of the transistor will be decreased according to

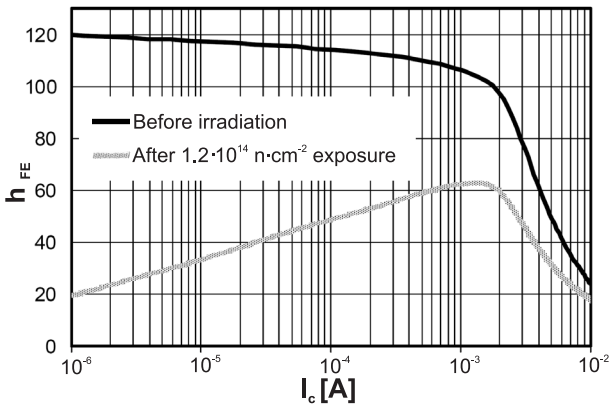

Figure 2.11: *Gain degradation of npn transistor after neutron irradiation [23].*

Equation 2.5.

$$\Delta\left(\frac{1}{h_{FE}}\right) = \frac{1}{2}\cdot\frac{w_B^2}{D_{pB}}\cdot K_\tau\cdot\phi = K_{h_{FE}}\cdot\phi, \tag{2.5}$$

where w_B is the base width of bipolar transistor, D_{pB} is the diffusion coefficient of holes within the base. The gain degradation is therefore proportional to the particle fluence during the irradiation and the damage coefficient associated with carrier's lifetime $K_{h_{FE}}$ [19] [1]. According to Equation 2.5, transistors exposed to radiation should operate in the region with a narrow base width, therefore high-frequency transistors opt to be more radiation resistant. Moreover, degradation depends on the collector current and as a result of this, is lower for high collector currents [19, 23]. The gain degradation for npn transistor fabricated in Rhbip1 technology from ST Microelectronics is presented in Figure 2.11. The transistor was irradiated from the neutron source with a dose 1.2×10^{14} n·cm^{-2}. The saturation voltage $V_{CE(sat)}$ may be significantly decreased because of the gain degradation of the transistor and increased silicon resistivity. The characteristics showing increased saturation voltage of a bipolar transistor after neutron-gamma irradiation is presented in Figure 2.12. Another parameter of a bipolar transistor affected by ionizing radiation is a collector-base leakage current I_{CB0}. A strong increase of the current is caused by the build-up charge in the oxide layer near the junction [22].

2.2.2 Displacement damage in MOS transistors

The operation of MOS transistors bases on minority carriers' transport, thus radiation exerts an imperceptible influence in displacement damage meaning [19, 21]. Displacement damage mainly affects minority carriers' lifetime. However, MOS devices are

[1] This equation is true assuming that transistor is homogeneously dropped. However, most experimental results confirmed that this equation can be used as well for graded doping.

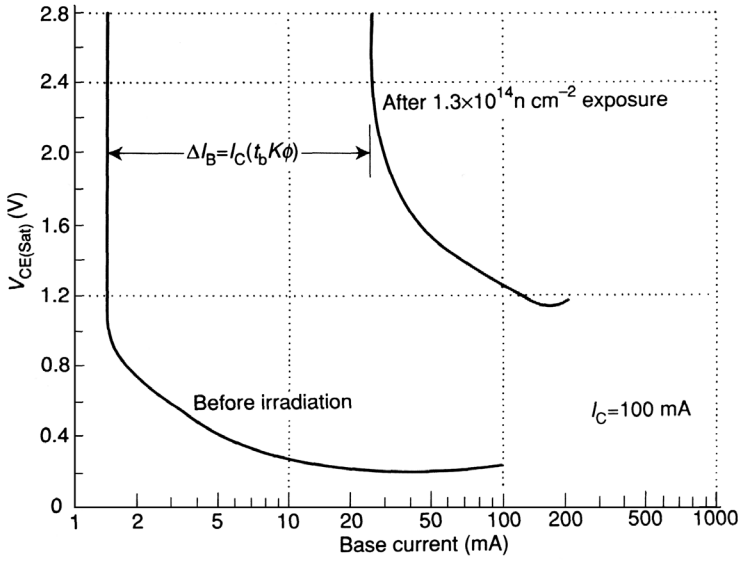

Figure 2.12: *Increase of the saturation voltage of 2N1613 bipolar transistor, irradiated from a neutron-gamma source up to dose 1.3×10^{14} n·cm^{-2} [22].*

profoundly amenable to ionizing effects. The impact of ionising radiation on silicon devices is described in Chapter 2.1. During the neutron interaction with a component the secondary ionizing particles may be produced. These particles are of much lower energy than the original, therefore ionizing damage cased by neutrons is relatively small, e.g. devices may be degraded at very high neutron fluences in the range of 10^{15} neutrons per cm^2 [21].

2.2.3 Single Event Effects

Apart from the ionizing phenomenon and displacement damage, radiation can affect electronic components by triggering single event effects (SEEs). Electron-hole pairs are produced when a semiconductor material is exposed to ionizing radiation. The number of generated pairs is proportional to the energy deposited in the material (see Table 2.2). The ionizing part of the deposited energy IEL defined by Equation 2.1 is called linear energy transfer (LET). LET is expressed in MeV· µm^{-1} or MeV·cm^2·g^{-1} when it is normalized to the specific mass of the absorbing material. LET can be calculated using the Bethe-Bloch equation [19,38,39]. LET is dependent on the incident particle type, atomic mass and its energy. Critical LET or LET threshold LET$_{th}$ is the maximum LET value deposited by the high-energy particle coming through the semiconductor device for which failure is not yet observed. When the created electron-hole pairs are expressed as a charge, the minimum charge necessary to create a SEE called the critical charge, can be found [40]. The critical charge as a function of the feature size for various technologies is presented in Figure 2.13.

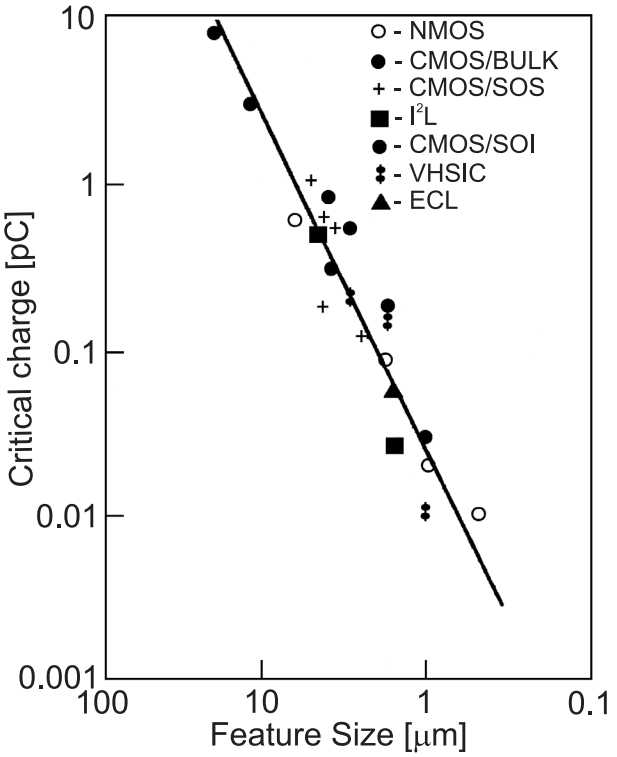

Figure 2.13: *Critical charge plotted as a function of the feature size for different technologies [19].*

One can distinguish two main groups of SEE: non-destructive when the device failure can be recovered by the system restart or reprocessing of affected data and firm or hard errors when the failure leads to permanent damage of the device or the system.

Non-destructive effects

Single Event Upsets (SEUs) affect mainly digital devices, e.g. microprocessors, field programmable gate arrays (FPGAs), memories and others stable or bistable elements. This phenomenon affects both bipolar and MOS technologies. SEU is a change of a device state induced by an energetic particle, which has enough energy to induce a error, i.e. ions, protons, recoil particles of neutrons nuclear reactions. Charged particles can directly ionize the sensitive volume of the electronic component and therefore create electron-hole pairs [41]. Furthermore, neutral particles, like neutrons can also generate SEEs through the secondary ionizing fragments, e.g. produced during an elastic or inelastic collision with silicon nuclei. Figure 2.14 presents a MOS transistor affected by the neutron. Most particles pass through silicon, however only a few interact with nuclei and produce ionizing particles (alpha particles, protons or heavy ions). High-LET particles lose their energy along a short path, heavily ionizing the silicon material. The radius of the ionization path is typically less than 1 µm. Even if carriers' density decreases with the inversely square proportion along the radius, CMOS devices can be

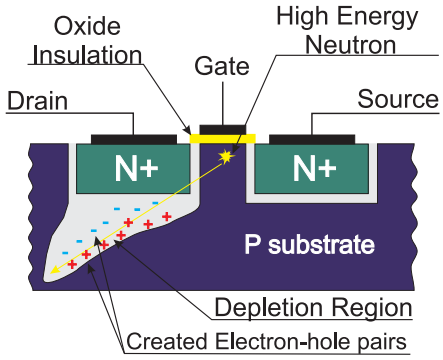

Figure 2.14: *SEU generated in a MOS transistor affected by high-energy neutron [42].*

affected by SEU. When the energy is deposited near the sensitive node of the device, e.g. drain of a MOS transistor, spike of the drain current can be observed, assuming that enough energy has been delivered. The induced current pulse is around hundreds of microamperes and lasts after nanoseconds. The critical charge created in a form of excited carriers, calculated using Equation 2.6, is dependent on the device's fabrication technology. The critical charge corresponds to the deposited energy LET_{th}.

$$Q_{crit} = \int_0^{tf} I_D(t)dt, \tag{2.6}$$

The critical charge is roughly in range of femtocoulombs for 0.5 µm technology, according to Figure 2.13. The SEU sensitivity of a device is expressed as a cross-section σ and can be calculated as relationship between the number of detected SEU N_{SEU} and a particle fluence Φ, see Equation 2.7.

$$\sigma = \frac{N_{SEU}}{\Phi}, \tag{2.7}$$

The cross-section is usually different for various particles. Furthermore, it is desired to measure the cross-section of electronic components for particles with different LET energy and characterize LET_{th} [25]. The exemplary cross-section for the configuration memory of Xilinx Virtex XQVR300 obtained using heavy ions beam is presented in Figure 2.15. The experimental data were fitted using the Weibull equation [43]. The saturated cross-section is defined for high-LET particles when all incident ions are capable of producing SEU and the cross-section is constant.

Single Event Functional Interrupt (SEFI) is a subgroup of SEU effects concerning high-density programmable devices, like CPLDs or FPGAs. The SEFI can result in a malfunction of control logic of a device and/or system. Finally, the device is stopped

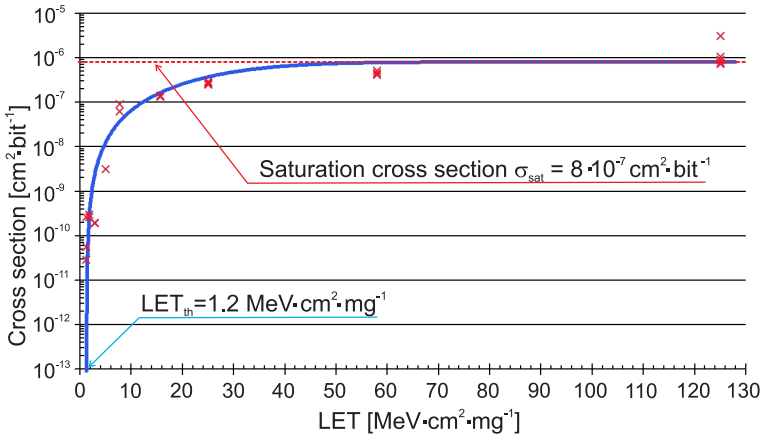

Figure 2.15: *SEU cross-section of Xilinx Virtex VQVR300 FPGA [44].*

and the external reset is necessary to recover the normal operation [45, 46].

Single Event Transient (SET) effects are in a form of voltage or current spurious pulses caused by the charge collected through the ionizing event. The generated transient can propagate through the digital or analogue circuit and bring about the disturbance in the output signal [47, 48]. SEU can be detected and corrected, however SET mitigation techniques are still within research [49–51]. The created malfunction can be difficult to diagnose since the SET effect can be detected in other system's path or module than the generated event [52]. Furthermore, SET is a crucial problem for modern technologies, when the transistor's dimensions and critical charges necessary to generate SEE are significantly decreased. Multiple, large transient disturbances can be created from single particle interactions. SET depends on the fabrication technology and varies essentially with the device parameters, the amplitude of the initial current pulse, and the duration of the event with the respect to the circuit operation frequency. Moreover, the operation frequency of current devices and circuits is continuously going up, therefore the probability that SET will be triggered, is increased. The exemplary SETs registered in the LM139 comparator with different loads are presented in Figure 2.16. SETs were generated using 815 nm laser. The comparator was supplied from 5 V and the differential input was equal to +100 mV. Typical examples of SET events are spurious pulses observed in voltage comparators, operational amplifiers and digital high-density devices [45, 47].

Destructive effects

Single Event Latch-up (SEL) is a potentially destructive event that can affect CMOS-based devices. CMOS integrated circuits consist of two types of transistors: NMOS and PMOS. CMOS devices contain two parasitic lateral bipolar transistors p-

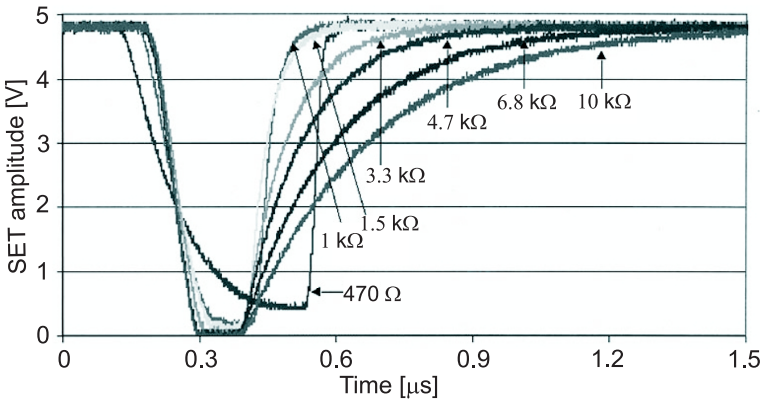

Figure 2.16: *SETs observed in LM139 comparator excited with 815 nm laser [53].*

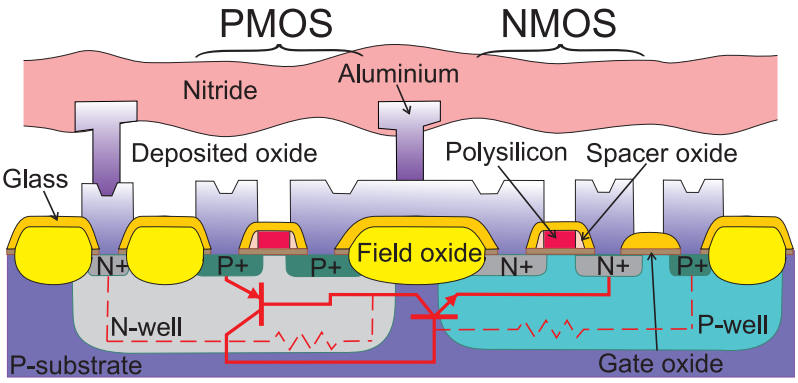

Figure 2.17: *A parasitic thyristor structure responsible for SEL in CMOS inverter [54].*

n-p and n-p-n, which can represent a parasitic thyristor structure pnpn (or npnp), see Figure 2.17.

During the normal operation the thyristor is disabled because of reverse-biased well-substrate junctions, therefore no current flow between the thyristor anode and cathode is observed. When the following conditions will be fulfilled, the thyristor can be activated by the high-LET particle:

1. The gain $\beta_{npn} \cdot \beta_{pnp}$ product of parasitic transistors must be greater than 1.
2. Enough current must be injected into base-emitter junctions of parasitic transistors.
3. Power supply must assure the holding current to maintain the latch process.

When the thyristor is activated and latch-up is observed, high current will flow through the low-impedance patch and the component can be locally overheated and destroyed. The only possible solution is to disconnect the power supply and disable the parasitic thyristor and recover the normal operation. The channel length and the epitaxial layer thickness have a crucial influence on the SEL susceptibility. Therefore, devices produced in new technologies can exhibit a greater susceptibility to SEL [55]. SEL

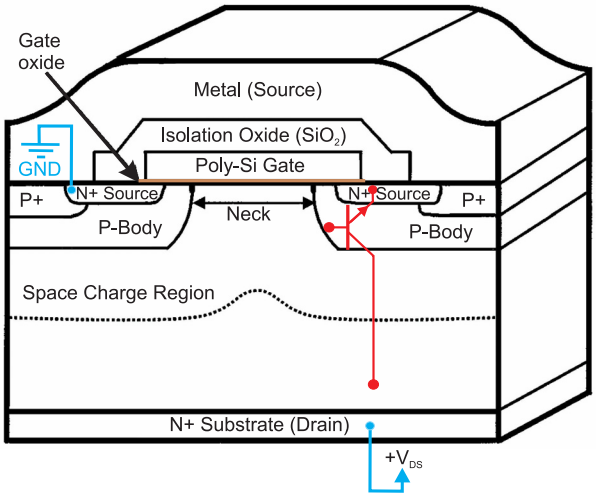

Figure 2.18: *The cross-section of the VDMOS transistor [58].*

cross-section increases sharply with the temperature. The gain of lateral bipolar transistor enhances and therefore the latch-up can occur for the greater base thickness [19].

Single Event Burnout (SEB) affects mainly high-power MOS transistors, like VDMOS or DMOS. The cross-section of VDMOS transistor is illustrated in Figure 2.18. The device is only sensitive in the disabled mode when the voltage drop across the source-drain is large. The trajectory of the high-energy particle must come through the parasitic bipolar transistor. Then the particle may generate the high-density tail of electron-hole pairs along its track. The large current density in range of 10^4 A·cm^2 can be generated in the presence of the high drain-source voltage [56, 57]. When the voltage drops on the base-emitter junction of inherent parasitic bipolar transistor and exceeds 0.7 V, the transistor may be turned on because of the avalanche multiplication of the BJT collector current. The local power density may be large enough to result in the excessive junction heating and eventual device's burnout.

Single Event Gate Rupture (SEGR) refers to dielectric breakdown brought about by an energetic particle and concerns mainly power MOS transistors [59]. When the particle comes through the thin gate, oxide electron-holes are generated and divided by the electric field towards the drain and gate. The generated carriers, the positive charge collected near Si/SiO_2 interface, increase the electric field in the gate oxide. The oxide leakage current is also increased because of the trapped charge and disturbed electric field. When the transient disturbance is large enough a significant charge collected in gate oxide can be discharged. The temperature in the nearest vicinity can increase and locally destroy the oxide [19, 58]. SEGR can be observed in non-volatile memories, like EEPROMs, during the write or erase procedures when relatively high voltage is

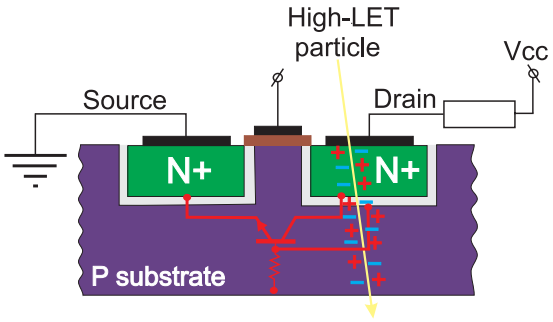

Figure 2.19: *The inherent bipolar transistor of NMOS structure affected by the high-LET ion [45].*

applied to the transistor's gates.

Single Event Snapback (SES) is similar to the SEL effect, which affects mainly NMOS transistors. High-LET particle can strongly ionize the MOS structure and therefore turn on the inherent parasitic bipolar transistor, which is illustrated in Figure 2.19. Contrary to SEL, the circuit can recover its operation by sequencing electrical signals without reducing the main supply voltage. However, SES may be destructive when the local current density is high enough. SES can mainly affect devices manufactured in standard CMOS technology and much more resistant to radiation silicon-on-insulator (SOI) [60, 61].

2.3 Conclusions

Both ionizing and displacement damage affects different electronic components including bipolar and MOS-based devices. Moreover, the effects can also affect passive elements, i.e. resistors, capacitors. Negative effects are discussed in Chapters 2.1 and 2.2. Radiation also exerts an influence on CMOS circuits, where both NMOS and PMOS parameters are modified. The change of MOS parameters has a following effect on CMOS devices:

- a reduction of digital L and H output levels,
- a decrease of the maximum output current,
- an increase of propagation time,
- an increase of the quiescent current.

The devices suffer mainly because of the ionizing effect. The influence of radiation strongly depends on the fabrication technology, characterised by the feature size, which

is getting smaller, whereas the technology is developed. The most important parameters of the current and predictions for future technologies are collected in Table 2.3. The old technologies with the feature size larger than 0.35 µm suffer mainly because

Parameter	2001	2002	2003	2004	2005	2008	2011
Channel length [nm]	100	85-90	80	70	65	45	30-32
Oxice thickness [nm]	1.5-1.9	1.5-1.9	1.5-1.9	1.2-1.5	1.0-1.5	0.8-1.2	0.6-0.8
Supply voltage [V]	1.2-1.5	1.2-1.5	1.2-1.5	0.9-1.2	0.9-1.2	0.6-0.9	0.5-0.6

Table 2.3: *The comparison of main parameters for the following fabrication technologies of CMOS integrated circuits.*

of ionizing effects, yet displacement damage effects are negligible. The devices are able to operate up to hundreds of Gy(Si) of total dose within an acceptable increase of power consumption. Digital devices are sensitive to SEE, especially to SEU and SEL. When the dimensions of MOS transistors get smaller, the devices are more susceptible to SEU as a result of decreased supply voltage and critical charge [28, 62]. The probability of SET and SETI effects increases with the operation frequency of electronic devices. However, modern submicron CMOS technologies generally seem to be more resistant to ionizing radiation due to very thin oxide [63]. Accumulated charges in the gate-oxide can be removed by tunneling. The devices in 0.35 µm can tolerate TID in range of 0.5–3 kGy(Si), whereas components produced in 0.25 and 0.18 µm process are able to operate up to dozens of kGy(Si) [63, 64]. These devices manifest themselves in good SEL resistance. Further scaling creates new problems with thin gate oxide. High electric field in the gate oxide is conducive to induce SEGR [32, 65].

Chapter 3

Radiation mitigation techniques

The term "radiation-hard" or "radiation-hardened" is often employed to describe different forms of devices' tolerance to radiation [22]. Therefore, in the following chapter, this term will be applied to denote devices immunized against the radiation effects during the design and fabrication process. Accordingly, the component or system designed using radiation-sensitive devices in such a way that it can tolerate radiation-induced errors, will be called radiation-tolerant.

Electronic components employed to design systems dedicated to operate in radioactive environments can be divided into three groups taking their tolerance to radiation into consideration, see Table 3.1. Consequently, radiation resistance of electronic cir-

Radiation tolerance	**Groups of materials**
High	Metals, ceramics and inert gases
Fair	Bipolar ICs, rectifying diodes, hardened MOS circuits
Poor	Commercial MOS circuits, analogue devices, solar cells, power transistors and CCD

Table 3.1: *Radiation tolerance of materials and components used to design systems dedicated to operate in radioactive environment [22].*

cuits strongly depends on materials used to manufacture the devices. Silicon-based devices are relatively cost-effective and therefore widely used. For that reason the following chapter is devoted to silicon components, although some of the presented radiation hardening techniques can be also adopted for devices composed of different materials.

One can distinguish three main groups of radiation mitigation techniques:

- methods implemented during the design and fabrication process,
- shielding of the most critical subsystems or components,
- techniques applied to design rad-tolerant circuits or systems.

Only modification of the electronic devices fabrication process or shielding can allow to protect devices against TID effect and displacement damage. The last group allows to immunize devices or systems against SEE, in particular SEU and SEL.

3.1 Hardening on the design stage

The hardening during the design and fabrication of integrated circuits gives extensive freedom and therefore allows to design rad-hard devices that are able to tolerate errors provoked by neutrons and gamma radiation (described in Chapter 2). One can distinguish three levels on which the devices can be designed [66]:

1. Modification of crucial technological parameters.
2. Application of additional layout processing.
3. Modification of their electrical construction.

Moreover, during the fabrication stage one can aim to enhance the tolerance against TID or SEE. The hardening techniques discussed in the following chapter concern chiefly bulk CMOS, except the subsection dedicated to the silicon-on-insulator (SOI).

3.1.1 Modification of the crucial technological parameters and circuit's layouts

Hardening of the TID encompassed mainly understanding, optimising and modifying oxide and silicon-oxide interface defects [67–71].The main objective is therefore to minimize the growing charge Q_{ot} and Q_{it}. Larger volume of oxide allows to cumulate a greater number of holes. The threshold voltage shift depends on the oxide thickness in the relationship t_{ox}^{n}, where n is usually between 1 and 3 [22]. Hence, radiation-hardened device should have as thin oxide as possible to allow a trapped-hole annihilation by the electron tunneling from oxide-silicon interface and polysilicon gate [21]. Modern submicron fabrication technologies use oxide in range of nm allowing to design devices resistant to gamma up to hundreds of kGys [64, 72–74].

The removal of impurities during preparation and cleaning process of gate oxide's material may also help to improve their immunity to TID [22]. In addition, the mechanical and chemical preparation of the starting material helps to remove contaminations, impurities and surface damage, like dislocations and stacking faults. A well-prepared surface allows to obtain high quality Si-SiO_2 interface and therefore obtain the component more resistant to radiation.

Field-oxide leakage tends to be dominating in CMOS technologies because of positive charge accumulation and presence of field oxide transistors (FOXFETs) [66, 69,

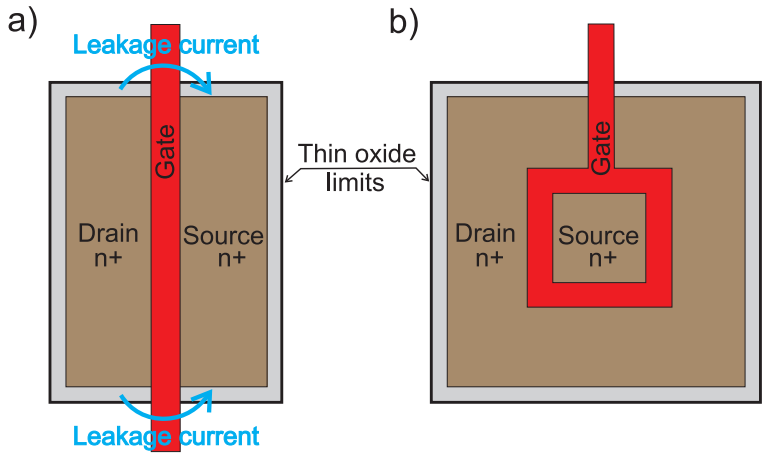

Figure 3.1: *A standard MOS transistor and its hardened version [76].*

71, 75]. Therefore, the modifications of layouts, e.g. application of additional guard rings surrounding MOS transistors and technological parameters, allow to modify the transconductance of parasitic FOXFETs and eliminate their number [66, 76]. The comparison of layouts of a standard MOS transistor and the radiation-hardened version is exemplified in Figure 3.1. Furthermore, an additional substrate bias can be used to turn off FOXFETs and therefore improve the parasitic leakage current [77].

The modification of fabrication parameters and the device structure have also influence on SEL and SEU sensitivity. Various process modifications can be used to reduce the possibility of SEL. An increase in substrate doping and profiling the impurity doping in MOS-wells help to reduce the sensitivity to both effects. Another method to enhance SEL immunity is to diminish the positive feedback of the parasitic transistors presented in Figure 2.17. The suitable doping profile allows to decrease the minority carrier's lifetime in the parasitic base region [19,28,66]. Finally, one can place wells into additional guard rings and apply extra well contacts [78, 79]. Single-event susceptibility can be reduced by manipulation of the W/L aspect ratio of the MOS transistor [80–85]. A change in W/L allows to increase the node's capacitance and thus enhances the critical charge necessary to induce SEU. A soft error phenomenon can be easily simulated and consequently the minimum transistor's size required to improve the CMOS gate resistance to SEUs can be found [28, 81]. An application of different layout techniques allows to obtain a higher immunity to both SEL and SEU although more silicon space is necessary. The best results of integrated circuits hardening can be obtained when a thin silicon layer including electronic circuits is placed on the top of relatively thick insulator. This method is called the silicon-on-insulator. CMOS circuits can be constructed on substrates consisting of epitaxially grown silicon on sapphire when the Silicon-On-Sapphire (SOS) is used or on the silicon dioxide insulator for the Silicon-

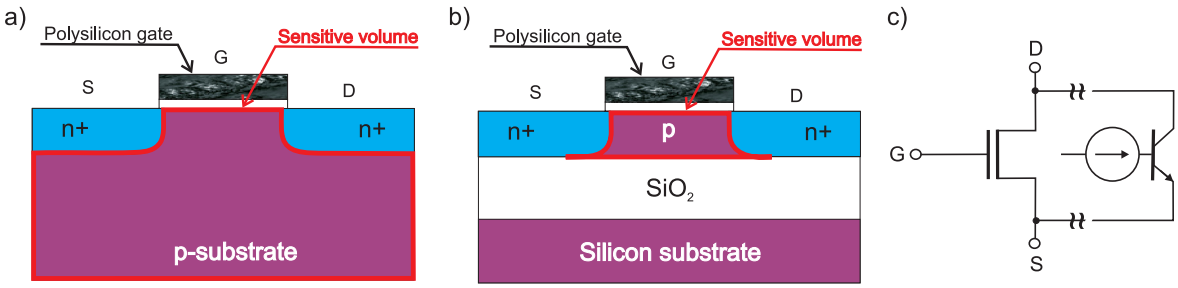

Figure 3.2: *A comparison of bulk CMOS and SOI transistors. Figure a) presents the sensitive volume of a bulk transistor, b) SV of SOI MOS and c) parasitic bipolar transistor in SOI structure [68].*

On-Insulator (SOI) technology [86][1]. Both techniques have advantages for reducing transient induced current and charge collection areas. The sensitive volumes (SVs) of MOS transistors are significantly decreased because of transistors' placement in a thin silicon layer on the insulator, contrary to bulk-silicon ICs, where the charge can be collected in a deep substrate along the particle track [87]. The comparison of SV for single MOS structures between traditional CMOS and SOI is shown in Figure 3.2. In practice, the sensitive area of a SOI transistor is larger than the one presented in Figure 3.2 because of presence of a bipolar parasitic transistor. The transistor has a floating base, therefore the radiation-induced current may be multiplied. Despite the presence of the bipolar transistor, the SOI technology is much more resistant to SEU than a bulk CMOS. The second most important destructive SEE - SEL effect is eliminated because there is no parasitic thyristor structure, see Figure 3.2.

The main disadvantage of both technologies is their high production cost. Lattice parameters' mismatch between the sapphire substrate and the grown silicon layer causes additional problems in the presence of radiation. SOI technology has attracted designers' attention because of its high total dose tolerance, an inherent SEU immunity, absence of a latch-up mechanism and lower production costs in comparison to SOS [88, 89]. High-density devices like hardened memories or microcontrollers can be fabricated in SOI [90, 91, 91].

In spite of a good immunity to SEU and SEL, SOI has a serious drawback – the sensitivity to build up radiation-induced charge in the buried oxide (BOX) [92]. The accumulated positive charge in the oxide of a partially depleted back transistor causes an inversion in the bottom part of the channel and an increase in parasitic source-drain leakage current [93]. The accumulated charge leads to shifts in the threshold voltage and therefore can cause excess circuit leakage and finally circuit failure [90, 94]. However, the sensitivity to total ionizing dose can be reduced by optimizing and

[1]Both Silicon-On-Sapphire and Silicon-On-Insulator belong to the fabrication technology of integrated circuit, where the main circuit is placed on the insulator (SOI). However, the author uses the term SOI referring to the technology in which silicon dioxide is applied as an insulator.

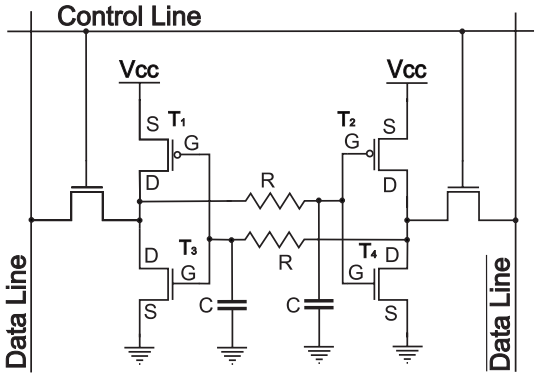

Figure 3.3: *Schematic diagram of the hardened SRAM cell [91].*

modifying oxide and silicon-oxide interface defects [95]. Moreover, an additional bias of the substrate can help to force away the radiation-induced positive charge [95].

3.1.2 Modification of integrated circuits electrical construction

The best radiation-hardened devices can be gained while all above-mentioned techniques will be used. SEU hardening can be also obtained by the modification of the electrical connection of circuits. Digital circuits chiefly suffer because of SEUs generated in latches and digital-value storage elements, which can be represented as a single SRAM cell or simple flip-flop. Thus, design changes in storage cells or sense amplifiers can be helpful to improve the resistance against such errors. A modification of the electrical design of storage cells and sense amplifiers is often used to construct radiation-hardened static random access memory (SRAM) cells [73, 96]. SEU tolerance can be improved when critical charge is enhanced. Firstly, additional resistors can be added into the memory component feedback path to create a low pass filter together with the capacitance of MOS gate. The filter can attenuate the SEU-generated signal, slowdown the regenerative feedback and therefore prevent the change in the SRAM-cell's state. Moreover, passive RC low pass filter can be implemented for longer duration transients. A standard 6T SRAM cell with added gate resistors and capacitor filters, designed for fabrication in a SOI process, is depicted in Figure 3.3. The main advantage of the resistive feedback is the little impact on the silicon area occupied by the SRAM. The main drawbacks are strong dependence on the temperature, degradation of the speed performance and the additional mask in the production process [97].

A radiation immune latch can be also designed using redundant nodes for its feedbacks [97]. Standard SRAM-cell nodes which represent logical zero can be affected by particles (transition from 0 to 1). Therefore, a radiation resistant structure can be obtained using redundant latches connected to sensitive nodes through adequately rescaled transistors. The exemplary redundant radiation-immune memory cell is pre-

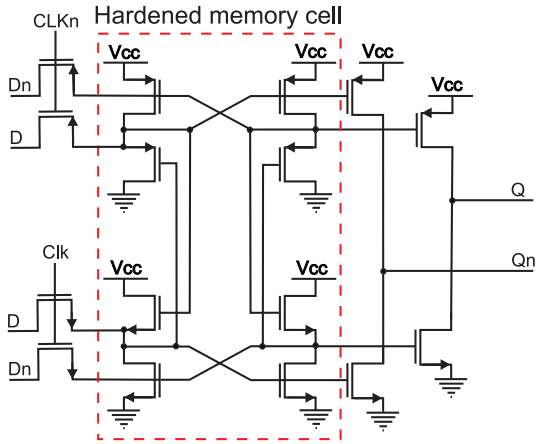

Figure 3.4: *Schematic diagram of hardened SRAM cell with output buffers [98].*

sented in Figure 3.4. The cell consists of two sections: nMOS-based structure used to store safely logical 0's and pMOS circuit dedicated to logical 1's [98]. During the operation only disabled nMOS transistors can be activated by ionizing particles. When the particle hits the sensitive node a conflict will arise and the redundancy provides additional feedback to recover data. The conflict will be resolved because of scaled transistors and therefore the state of the hardened flip-flop is not changed [73, 99]. The main drawback of the presented SRAM cell is the power consumption because of degraded voltage levels in both sections. Other hardened memory cells, e.g. Whitaker, Dice or Barry-Dooley designs, HIT cell, can be found in the literature [97, 98, 100].

3.2 Shielding

Radiation shielding may be a good solution for increasing the reliability and lifetime of electronic systems' operation in the radiation environment. Neutron and gamma radiation shielding usually requires using of heavy and large shielding blocks, therefore they can be applied only when there is enough room. However, shielding is occasionally more suitable from the economic point of view. The type of shielding material depends on final desired attenuated radiation levels, resistance to radiation damage, required thickness and weight, uniformity of shielding capability, permanence of shielding and availability [21]. For that reason, lead and concrete are the most commonly used.

3.2.1 Shielding against gamma radiation

Incident photons lose their energy chiefly because of ionization. Gamma radiation is subjected to the exponential law describing its attenuation within the material depth

x, see Equation 3.1.

$$I(x) = I(0)e^{-\mu x} \tag{3.1}$$

where I and I(0) are calculated radiation and initial intensity expressed as photons per cm^2 respectively, μ is the linear attenuation coefficient of the material in units of cm^{-1} [21]. The attenuation is dependent upon the atomic number Z of the used material and its density. Therefore, high Z dense shield materials are used to attenuate gamma radiation. Tenth value layer (TVL) coefficients for 0.5 and 0.8 MeV gamma rays, expressed in centimeters for a few different materials are presented in Table 3.2. Tantalum and tungsten are both high Z materials suitable for shielding against gamma

Shield material	**Atomic number** Z	**Tenth value layer [cm]**	
		0.5 MeV	0.8 MeV
Lead	82	1.4	2.6
Copper	29	4.0	5.0
Iron	26	4.8	5.9
Alluminium	13	14.0	16.0
Concrete	-	15.0	18.0

Table 3.2: *Atomic numbers and TVL coefficients for 0.5 and 0.8 MeV gamma rays.*

radiation. Nevertheless, their price is exorbitant, hence they are dedicated to special-purpose shielding. Lead is readily available and can be easily manufactured for the lower costs.

3.2.2 Shielding against neutrons

Neutrons are not charged, relatively heavy particles, therefore shielding is in this case not as easy as for gamma. The design of the neutron shielding is a complex process because the materials' absorption depends on the neutron energy. Besides, accurate design shielding requires the application of computational simulations. Codes, such as MCNP or SCALE, are used for that purpose [16].

The neutron shielding process involves three steps [21]:

1. Slowing down fast high-energy penetrating neutrons.
2. Absorbing the slowed down neutrons.
3. Attenuating the accompanying gamma radiation created during the activation of the shielding material.

Lead has an extremely low absorption of neutrons and therefore neutrons can easily penetrate this kind of shielding. The slowing-down process requires materials in which energy losses caused by collisions are the highest. Thus, neutrons should collide with

particles which have similar mass, e.g. hydrogen nuclei (protons). Therefore no high-Z materials, like water, plastic, paraffin, concrete or other hydrogen-rich hydrocarbons can be used to slow down (thermilize) neutrons. Thermal neutrons, with energy below 1 eV, can be absorbed by boron or cadmium materials, which have very high absorption cross-section for slow neutrons. Moreover, boron can be mixed with slowing down-materials in adequate proportions in order to obtain better attenuation, e.g. borated concrete, polyethylene [6-A] . One has to be careful as the application of a high rate of the neutron capture material will result in its high activation [21].

3.3 Design radiation tolerant circuits and systems

Radiation mitigation techniques used during the design stage allows to obtain radiation-hard devices, highly-resistant to TID and SEE phenomena. However, the modification of the fabrication process parameters and implementation of electrical improvements on the design level usually yields increased production expenses. Hardened devices are widely used in space when a high reliability is required and the total cost of electronics is of a minor priority. The application of hardening techniques on the system design level together with commercial-of-the-shelf (COTS) components enables to diminish radiation influence and keep the cost of the whole system on a reasonable level. Hardening by the system can be obtained by the duplication in logic modules and correcting or preventing failures [101]. In addition, methods implemented in software allow to mitigate SEUs without any modification of the hardware [102–104], [7-A, 8-A, 9-A, 10-A, 11-A]. Only SEU and SET effects may be mitigated while the destructive SEL can be tolerated. Notwithstanding, hardening-by-system requires usually additional resources and does not guarantee an error-free operation in the radioactive environment. As a consequence, hardening at the system level can be only applied when the requirements do not conflict with other restrictions.

3.3.1 Redundancy

Redundancy is one of the most effective hardening techniques applied during the system and software design [105, 106]. The application of redundancy in modules provides additional, useful information for the detection and correction of soft errors. One can distinguish dual or triple modular redundancy (DMR, TMR) depending on the amount of used additional resources. The comparison between DMR and TMR is presented in Figure 3.5. The usage of two similar devices (DMR) allows only to detect errors, however TMR supplies enough information to detect and correct single errors [107]. When errors occur in circuit secured by DMR, data can be rewritten in the memory or

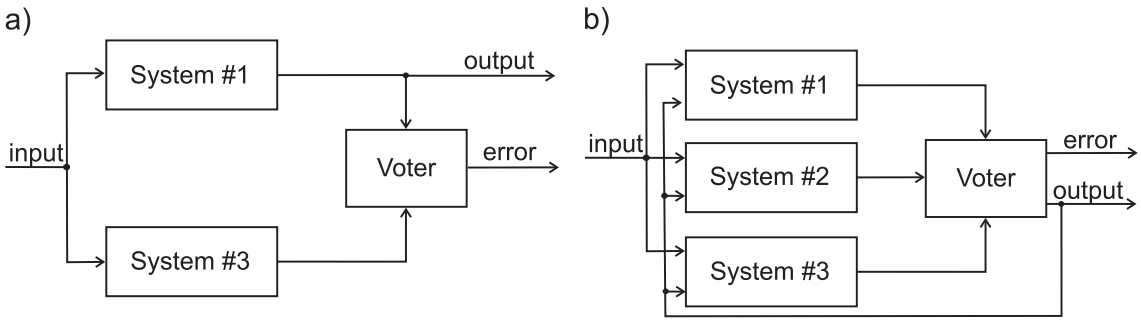

Figure 3.5: *The comparison between a) dual and b) triple modular redundancy.*

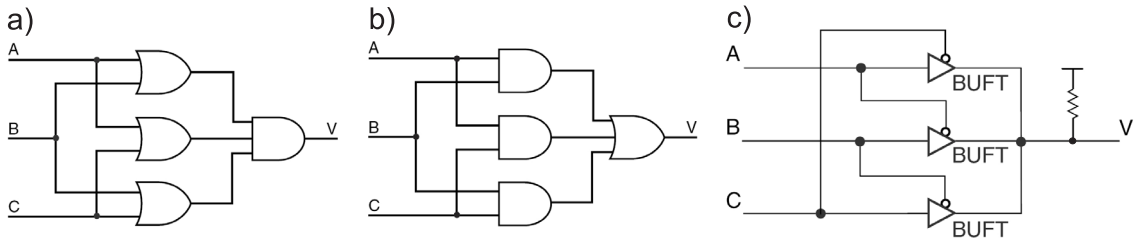

Figure 3.6: *Exemplary voters: a) OR-NAND, b) NAND-OR, c) tristate voter of Xilinx Virtex FPGA.*

system can be restarted. However, correct data can be voted when TMR is used [108]. In such a case, the recovered data are rewritten to all subsystems and there is no need to restart the system. A dedicated radiation resistant majority voter must be applied to make the decision process possible [109]. Redundancy can be applied to different modules, blocks or even to a whole system [97]. When a shortage of spare resources is observed, SEU-sensitive nodes can be found and selective redundancy can be applied [105]. The main drawback of the redundancy is a large consumption of additional resources, e.g. three times more flip-flops must be used to immunize a latch, not counting a voter. The voter should be designed using one of the techniques described in Section 3.1. Possible implementations of SEU tolerant voters are presented in Figure 3.6. The presented simplified schematic of Virtex FPGA tristate voter has a contentious state for inputs, consisting of two low and one high logic state. The real implementation in Xilinx Virtex FPGA results in the correct operation of the majority voter [110].

A fast and reliable voter can be also built using look-up table (LUT) present in FPGA [110]. LUTs are dedicated to implement various logical structures in programmable devices, therefore the performance and SEU immunity is strongly dependent on the FPGA architecture.

Time redundancy can be applied to conserve spare resources at the expense of the system speed. The critical operation is executed a few times using the same resources, results are latched and then compared [111].

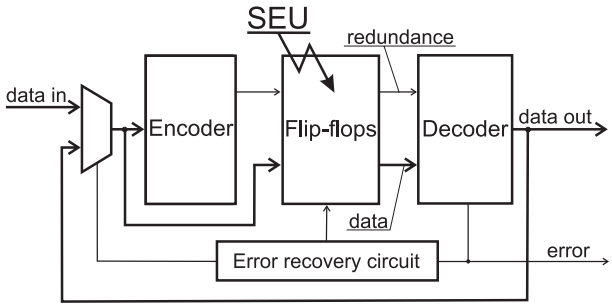

Figure 3.7: *The error detection and correction technique.*

3.3.2 Error detection and correction

Error detection and correction (EDAC) methods require a certain amount of redundancy to detect an error. When an error is found, the correct value can be recovered using error correction codes (ECC). The application of EDAC is depicted in Figure 3.7. Next, the decoded and corrected value is written to the storage structure to avoid accumulating errors [112]. The application of EDAC, therefore, improves the immunity to SEU or SETI. The system can incessantly operate, however the implementation of EDAC affects its effectiveness. The method can be used to improve the reliability of elements including storage structures, like finite state machines (FSMs), static and dynamic memories (SRAMs, DRAMs), etc. Depending on the ECC method, EDAC is able to detect and correct single or multiple errors.

Parity checking

The simplest ECC and therefore requiring the low level of redundancy, is parity checking. The implementation of a single parity bit for a given block of data enables detection of a single error, however the decoder is not able to repair the damage. The XOR operation can produce a parity bit during coding. The same operation can provide information about a possible error during decoding. Simple parity checking is rather not powerful enough to protect devices against SEU, however can be applied in a modified form as Rectangular or Hamming codes. Moreover, parity checking can be employed as an auxiliary operation, e.g. to determine, which module or device is in an erroneous state when DMR is utilised [113].

Rectangular Codes

Rectangular codes can be applied to a block of data to provide single errors correction and detection of double faults. The codes are more efficient for a large amount of data because of a better parity codes–codeword ratio. However, their error detecting efficacy decreases when a block of data increases. Control parity bits can be calculated

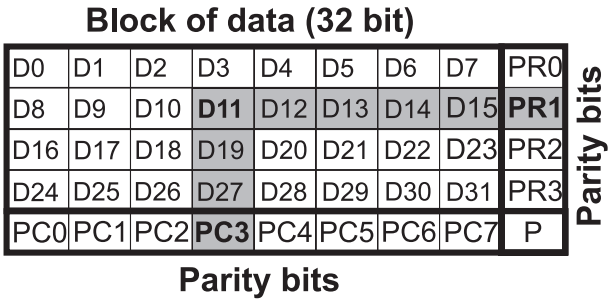

Figure 3.8: *The idea of rectangular codes [114].*

for every row and column of the rectangular data block [114]. Parity bits calculated for a 32-bits word is presented in Figure 3.8. When a single data bit is inverted, two parity bits are affected (PC3 and PR1). The knowledge allows to find and correct an erroneous bit. Only double errors can be detected. However, triple errors can be malignant as they can mimic a single error offending an innocent bit. The rectangular codes can be implemented in hardware as well as software [12-A].

Hamming codes

Error correction is more useful than detection, but requires a greater number of redundant bits and therefore is less efficient. Hamming codes take an advantage of additional information to detect and correct errors. However, the Hamming codes' efficiency in the meaning of required redundancy is optimal for correcting of all single errors and detecting double ones [115,116]. The formula (n, k, d_{min}) is usually used to denote the parameters of the Hamming code of the total length n with k bits of the codeword, which has a minimum Hamming distance equal to d_{min}. Therefore, the length of the binary single-bit correcting code can be calculated from Equation 3.2, according that d_{min} is equal to 3.

$$n \leq 2^m - 1 \tag{3.2}$$

where m is the number of redundant check bits, $m = n$ - k [117]. For a 32-bit codeword one has to use 7 check bits to detect and correct single errors. The eighth bit must be added to enable the detection of double errors. The Hamming code's encoder can be easily implemented in the FPGA device using XORs. The decoding operation is more complicated, first a syndrome must be calculated, then an error is located and corrected. The operation can be realized using XORs and decoders [118–120]. The technique is very efficient and can be applied for SEU mitigation at hardware as well [121, 122] as software levels [104, 116, 123], [12-A].

Reed–Solomon codes

Reed–Solomon (RS) codes are used to detect and correct multiple errors [116, 124]. The codes are dedicated to protect large blocks of data against a long error burst. A RS code can be represented as RS(n,k) with s-bit symbols for a encoder operating on k-data symbols of s-bit each and generates a n-symbols codeword. Therefore, $n - k$ parity symbols are added to the generated codeword. The redundancy allows to recover t erroneous symbols, assuming that $2t = n - k$. The maximum codeword length n is expressed by Equation 3.3.

$$n = 2^s - 1 \tag{3.3}$$

The RS decoder is able to correct up to s errors or r erasures, given in Equation 3.4.

$$2s + r < 2t \tag{3.4}$$

Thus, an error can correspond to the reparable SEU and erasure to permanent bit damage. The position of the erasure must be known.

The RS technique needs a significant amount of memory for complicated calculations and therefore the main drawback of RS is the speed and latency [125]. Moreover, the implementation becomes complicated because of the presence of registers [126]. Therefore, the encoder and decoder must be SEU tolerant. The implementation of RS coder and decoder in hardware is much more complex than Hamming codes' and therefore needs more resources. The RS codes are primarily implemented in software.

3.3.3 Memory scrubbing

Although EDAC methods allow to tolerate single or multiple upsets in memory structures, SEUs can accumulate in high capacity memories, and therefore decrease the efficiency of the recovery process. Periodic scrubbing can be used to avoid the accumulation of errors, thereby reducing the probability of multiple errors. Memory scrubbing consists of periodic reading of codewords from the memory block or segment. The data are corrected when an error is detected and rewritten into the same memory address. One of the above mentioned ECC can be used to check the data correctness. The scrubbing period must be carefully tuned to the system requirements taking SEU generation rate into consideration. A well-matched scrubbing interval does not allow to develop two errors before subsequent memory accesses. Consequently, less hardware-consuming ECC can be applied to correct single errors [127]. Scrubbing employs an additional resource, therefore an increase in the hardware's overhead is observed. Moreover, scrubbing does not guarantee an error-free operation. Scrubbing used together with other SEU mitigation techniques allows to design efficient mechanisms, especially

for environment with high error rates [128, 129].

3.3.4 Reinitialization recovery

In spite of the application of hardening techniques at different stages, SET can be generated [130]. The implementation of an external timer circuit acting as a watchdog could be desired, if the functional upset probability is important [107]. The circuit allows to restart the system when all other hardening methods fail [131].

3.3.5 SEL mitigation

Fast current-monitoring and current-sensing techniques can be used to counteract SEL. When SEL is detected, the supply current of the circuit should be limited and the submodule must be disconnected from the power supply. The current detection and limiting device must be characterized by a fast response in a range of ms or even faster to avoid destructive SEL [132].

3.4 SEU mitigation techniques for FPGA devices

FPGAs are very attractive programmable circuits because of their performance, flexibility, and production costs. SRAM-based FPGAs are widely used in applications where high performance is the major priority [133]. However, their configuration is usually kept in a SRAM memory. On the one hand the application of SRAM allows to modify comfortably the configuration and assure the high-speed operation. On the other hand, the main disadvantage of the device is its sensitivity to single event upsets generated by radiation. Radiation can change the contents of the SRAM, and therefore modify its configuration and result in a loss of a system's functionality. Radiation-hardened FPGAs use the antifuse technology to store their configuration [134]. As a result of this, antifuse-based FPGAs are much more immune to SEU, however such a device can be programmed only once. The alternative is an electrically reprogrammable FLASH memory, which is much more immune to radiation. Despite the SEU sensitivity, SRAM-based FPGAs can be still used in the radioactive environment when at least one of the hardening by system methods, described in Chapter 3.3, is used. Scrubbing can be applied to verify and refresh the configuration of FPGA [135, 136]. This method can be simplified. SRAM segments can be periodically rewritten from an external SEU-insensitive memory without time consuming comparisons [135]. In such a case, a scrubbing control circuit is also simplified. Instead of the address generator, which supervises FPGA configuration memory and reference SRAM, a simple

counter can be used. However, better results can be obtained when a full or partial configuration readback is implemented [105, 118].

Some of the FPGAs are equipped with the internal scrubbing system. Altera FPGAs uses 32-bit CRC IEEE 802 standard, polynomial code to check continuously the configuration random access memory (CRAM) contents [137]. The scanning time depends on the amount of CRAM and the error detection clock frequency [137]. The CRC_ERROR output signal is driven high when an error in a calculated CRC signature was detected. The CRAM can be easily reloaded and thus the proper operation of the circuit can be maintained.

Moreover, TMR can be applied to avoid SET and enable an uninterrupted operation of a FPGA. Reliable voters can be implemented in some FPGAs, therefore latches and a SRAM block can be tripled. Moreover, the circuit can be hardened against SEU by selectively applying TMR (STMR) to sensitive submodules, thus the size of the protected circuit is much smaller than the obtained using TMR [105].

3.4.1 Evolutionary fault recovery

Circuits implemented in FPGA devices always use accessible resources with some redundancy. For example, the implementation of a single NAND gate requires using of a single block, e.g. look-up table (LUT). Therefore, the inherent redundancy can be exploited to design a fault-tolerant description of a given circuit [13-A]. Firstly, the device can be implemented in such a way, that the changes in the CRAM connections or faults induced by radiation does not cause noticeable SEU or SET, because of the inherent logical excess. Secondly, the running device can be reconfigured dynamically during the operation to facilitate the repair through the reuse of damaged parts [116, 138]. Both approaches take advantages of the genetic algorithms (GAs) to evolve an error-tolerant implementation. Faults correspond to the mutation operation during the evolution, and therefore faults can be masked. Nevertheless, the technique is suitable for very simple digital circuits [139, 140].

The development of the evolutionary fault-recovering FPGAs is still in progress. The main disadvantages of evolutionary methods are a long time necessary to find a satisfactory error-resistant implementation and difficulties with supplying solutions that produce a nearly correct repair for on-line systems [141].

Concluding, the best results in hardening electronic devices can be obtained when different approaches are used concurrently: modifications during design phase, the fabrication process, hardening by shielding, and applied when the system is designed [129].

Chapter 4

State of the art of the neutron and gamma radiation dosimetry

Devices and components installed in linear accelerator tunnel operate in a mixed neutron-gamma radiation field. The primary and secondary ionizing radiation are responsible for damage of devices, which has been described in Chapter 2. The nature of electronic components or systems' damage depends on the radiation type and its energy. Therefore, IEL damage is usually quantified in the terms of the ionizing dose released in SiO_2 and the NIEL in the terms of Kinetic Energy Released in Medium (kerma) K, which can be specified by Equation 4.1 [22, 142, 143].

$$K = \frac{d\overline{E}_{tr}}{dm} \tag{4.1}$$

where $d\overline{E}_{tr}$ is the energy released in a volume element whose mass is dm [142]. From this point of view it is desired that the radiation monitoring system measures both the IEL and NIEL damage. The absorbed dose of ionizing gamma radiation can be easily quantified using commercially available dosimeters. Contrary to gamma, neutrons as a particles devoided of charge cannot be detected directly. Therefore, their mensuration is more complicated. Thus, the neutron fluence is usually determined via detection of secondary ionizing particles. Nuclear reactions suitable to neutron dosimetry are depicted in Table 4.1[1]. Radiation levels should be monitored in real-time, because of this dosimeters must be able to deliver signals with a minimum delay. Moreover, detectors should supply output signal, which can be easily integrated using electronic readout system.

[1] $^{7}Li^{*}$ and Gd^{*} correspond to unstable nuclei in excited states. The nucleus comes to a stable state when it releases a quantum of energy in the form of the gamma ray.

Nuclear reaction	Secondary particles energy
$^{3}He + n \rightarrow {}^{3}H + {}^{1}H$	0.764 MeV
$^{6}Li + n \rightarrow {}^{4}He + {}^{3}H$	4.79 MeV
$^{10}B + n \rightarrow {}^{7}Li^{*} + {}^{4}He \rightarrow$	$^{7}Li + {}^{4}He$ + 0.48 MeV γ + 2.3 MeV (93%)
	$^{7}Li + {}^{4}He$ + 2.8 MeV (7%)
$^{155}Gd + n \rightarrow Gd^{*} \rightarrow \gamma$-ray $\rightarrow$	conversion electron spectrum
$^{157}Gd + n \rightarrow Gd^{*} \rightarrow \gamma$-ray $\rightarrow$	conversion electron spectrum
$^{235}U + n \rightarrow$ fission fragments	160 MeV
$^{239}Pu + n \rightarrow$ fission fragments	160 MeV

Table 4.1: *Nuclear reactions used for the neutron detection [144].*

4.1 Neutrons and gamma dosimetry

A large number of different instruments able to measure gamma radiation, utilizing electrical, photographic, thermal, luminescent, chemical and biological effects of radiation, can be applied to determine the absorbed dose or just for particles' detection [145]. Most of detectors used for gamma dosimetry can be adapted for the neutron fluence measurement when a suitable converter is applied, see Table 4.1. Converters are used in different forms: liquid, gaseous or solid.

Dosimeters are only able to detect or precisely measure radiation depending on the used method, sensitivity, energy dependence and temperature stability. The comparison of various types of dosimeters is presented in Table 4.2[2]. Detectors can be divided into two groups: designed for passive and dedicated to on-line dosimetry.

4.1.1 Gaseous detectors

The principle of radiation detection with gas-filled chambers is based on the direct or indirect ionization of the material of which the detector is made. The detector is chiefly composed of a gas-filled chamber surrounded by electrically conducting walls. An exemplary cylindrical in shape device is presented in Figure 4.1. The central, inner electrode is the anode and the outer one acts as the cathode [151]. Exterior and collecting electrodes are isolated with a highly resistive insulator to minimize the current leakage. When the applied DC voltage is high enough, a charged particle passing through the volume ionises the filling gas.

Produced ions pairs are attracted to electrodes because of an electric field distributed across gas and as a result the pulse or increase of current is generated. The production and movement of ions is accompanied by the recombination process. In-

[2]The measuring range and dose rate units of the following radiation detecting methods have been unified with regards to doses of radiation deposited in air and are presented in grays (Gy) or neutrons per cm square.

Dosimeter type	Detection principle	Measuring range or dose rate
Ion chamber	Ionization of air or another filling gas	10 nGy·h^{-1} – 10 Gy·h^{-1}
Geiger-Müller and proportional counters	Ionization of gas with multiplication of electrons in a detector medium	10 nGy·h^{-1} – 100 Gy·h^{-1}
Scintillator	Ionization and excitation followed by light emission	10 nGy·h^{-1} – 100 mGy·h^{-1}
TLD	Excitation of crystals, charge trapping and light emission	10 µGy – 1 kGy
Bubble dosimeter	Evaporation and formation of bubbles via nucleation process	100 nGy – 50 µGy
Activation foils	Production of radioactive daughter nuclei	10^3 n·cm^{-2} – 10^{19} n·cm^{-2}
Solid state or silicon detector	Ionisation of semiconductors, semiconductor damage	1 µGy – 100 Gy
Calorimetric	Heating of a reference mass	1 Gy – 1 MGy
Photographic film	Ionisation of silver compounds (AgBr or AgCl), nuclear reaction	1 mGy – 100 Gy
Chemical	Inducing of chemical reactions (ions)	0.1 kGy – 1 MGy

Table 4.2: *The comparison of radiation dosimeters methods [16, 21, 22, 142, 145–150].*

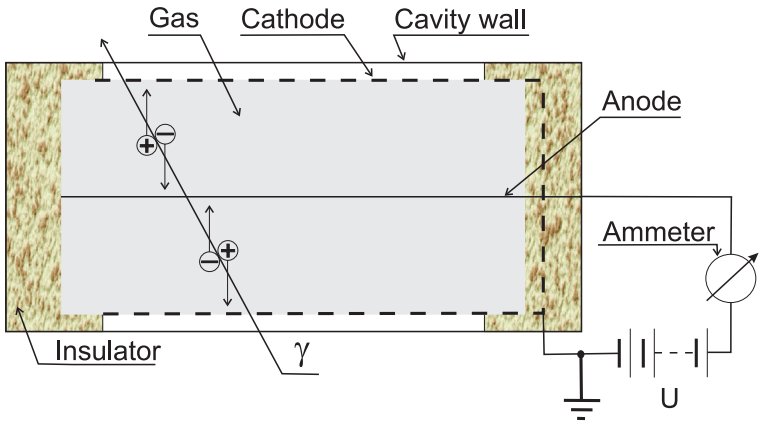

Figure 4.1: *A cross-section of the cylindrical ionizing chamber filled with gas.*

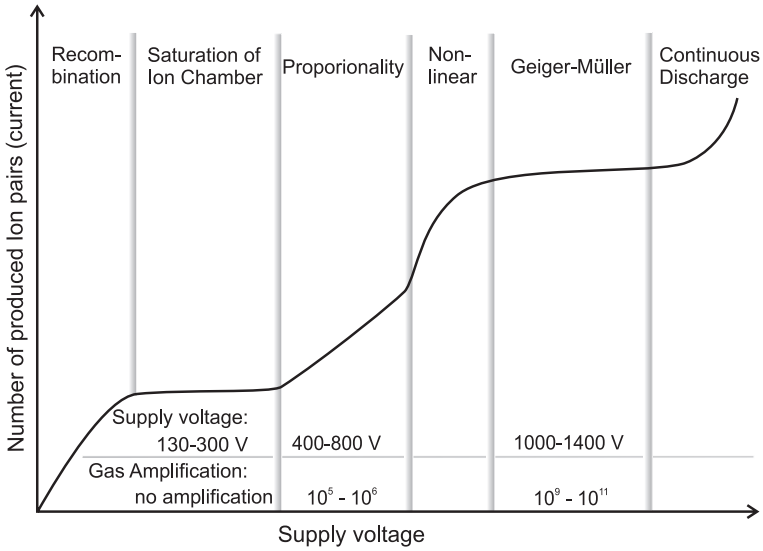

Figure 4.2: *A possible regions of the gas-filled detector operation [153, 154].*

creasing the supply voltage allows to decrease the recombination. When the electric field reaches a suitable amplitude, the recombination of ions can be neglected and almost all produced ions can be collected by electrodes [152]. One can distinguish three main types of gaseous detectors, depending on the level of the applied voltage and its operation mode:

- ionizing chamber,
- proportional counter,
- Geiger-Müller counter.

The characteristics of the gas-filled detector with possible regions of its operation is presented in Figure 4.2. The ion chamber operates in the saturation region, when the recombination process can be neglected, see Figure 4.2 [153]. The number of produced ion pairs is independent on the voltage. Therefore, the output current is proportional to the deposited energy in detector's sensitive volume. No gas amplification is observed,

thus the current is relatively small. An increase in the supply voltage causes gas amplification of the produced charge proportional to the voltage (see Figure 4.2) [151]. This operation mode is characteristic for proportional counters. The measured radiation can be determined upon the output current or counting the number of generated pulses for a given period of time.

A further increase of voltage causes a much higher amplification of the Geiger-Müller (GM) mode, which results in its sensitivity enhancement [146]. The operation of the device is similar to the ionizing mode, however the amplitude of a generated signal is independent of the intensity of incident particle energy. Therefore the detected radiation can be only calculated by counting the number of generated pulses for a given period of time. 60 second periods are usually used, thus the common unit for the GM counter output signal is Counts Per Minute (CPM). This mode allows to detect very low levels of radiation, however it is not suitable for the radiation dosimetry. A GM counter is very sensitive to radiation energy, especially for low energy photons (E_{ph}<80 keV). The GM counter has a very long dead time (time necessary to discharge the main capacitance before the next interaction) in a range of tens of millisecond [155]. The detector may be saturated or paralysed when the incident radiation is too high. No pulse will be generated in such a case and the readout will be equal to zero (dead time effect) [153].

A further raise of supply voltage results in unstable conditions and can result in damage of the counter due to electrical arcing [156].

Ion chambers and proportional counters operating in a current mode are predominantly used as sensitive dosimeters. The ionizing chamber filled with 1 cm^3 of air is commonly used for gamma dosimetry. The dosimeter is calibrated to give the air kerma or a tissue equivalent dose [157]. The dosimeter can be used for the measurement of a thermal neutron dose when it is filled with gas, which has a large thermal neutrons cross-section, like ^{10}B or ^{3}He according to Equation 4.1 [144, 150, 158, 159]. Moreover, an application of an additional moderator with a thermal neutrons filter allows to measure the doses of fast neutrons. The neutron energy independence of gaseous detectors depends to a large extent on the moderator design [160]. The sensitivity of gas-filled detectors can be enhanced by the gas pressure increase and the expansion of electrodes dimensions [161]. Ionizing chambers and proportional counters reveal dead time in the range of tens of microseconds, therefore the measured dose may be underestimated in high dose rate fields. Ionizing chamber-based neutron dosimeters have a limited ability to discriminate neutrons and photons, for example, the 1 MeV gamma radiation sensitivity may be only two orders of magnitude lower than the maximum neutron detection ability. A pulse build-up may occur in a high dose rate gamma-neutron field when the mean interval between gamma pulses will be shorter than the resolving time of the

detector and its readout circuit [158]. High sensitivity and precise gas-filled detectors require high pressure inside of its chamber and a large supply voltage, see Figure 4.2.

4.1.2 Semiconductor detectors

Semiconductor-based detectors reveal a few crucial benefits, like a fast response, high ruggedness and small dimensions in comparison with other dosimeters [162–164]. Moreover, energy required to produce an electron-hole pair in silicon is equal to 3.6 eV, compared to 35 eV in gas and 1000 eV necessary to generate a photoelectron by a cathode of a photomultiplier [142]. Silicon creates additional problems in classical dosimetry because of a different effect of radiation on silicon and biological organisms (Tissue Equivalent). Then, the measured does must be recalculated using a tissue-equivalent factor [142]. However, this fact is an unquestionable advantage, when the study or a counteraction against radiation damage of electronic devices made of silicon is the main goal [22, 143].

Silicon diode

A p-intrinsic-n junction (PIN) and photodiodes are widely used for dosimetry purposes [150, 153, 164–167]. A diode can be forward- or reverse-biased and can operate in a direct current or the pulse mode. The reverse-biased diode functions as a small solid-state ionizing chamber. Ionizing radiation can create free carriers in the large intrinsic area and a depletion region of the diode. An electric field present in a semiconductor causes carriers' separation and therefore the pulse of reversed current flow is observed. The pulse mode is usually used for the ionizing radiation measurement in the low dose rate environment. An application of an additional conversion layer allows to detect neutrons indirectly [162, 168, 169]. The amplitude of the induced pulse is proportional to the deposited energy, therefore ionizing and non-ionizing particles can be discriminated to some degree in mixed environments. The direct current mode is used in high dose rate fields [162]. The discrimination of particles is not possible in this case.

The forward-biased silicon diode is continuously degraded when exposed to the neutron radiation influence [143, 170, 171]. Therefore, as discussed in Chapter 2.2, the resistivity of bulk silicon and the lifetime of majority carriers will be decreased because of the formation of new recombination centres. The voltage drop on the diode increases with the absorbed dose of radiation [171]. The kerma is proportional to the voltage, assuming that a constant test current flows through diode.

Diode dosimeters are ideal for the on-line measurement, however their parameters depend strongly on the diode temperature. Thus, a suitable correction or tempera-

ture stabilisation is necessary to assure precise measurements. Diodes have a linear response only in limited range and the degradation process is dependent on the incident energy of the particles. Moreover, diodes undergo fading because of the annealing phenomenon [172]. The temporary current annealing or measured dose correction may be applied to improve the radiation measurement's accuracy [173].

Silicon transistor

Ionizing radiation has an appreciable influence on parameters of the MOS transistor, see Chapter 2.1.1. Radiation causes the threshold voltage V_T shift, which is slightly different for n-type and p-type transistors. These effects were presented in Figures 2.3 and 2.2. This phenomenon was utilized to design Radiation sensitive Field Effect Transistor RadFET with an enhanced thickness of the SiO_2 structure [173–175]. PMOS transistors are usually used as dosimeters because of a better linearity between V_T and absorbed dose [176, 177]. The ionizing radiation sensibility increases with the applied electric field, thus the RadFET's sensitivity can be tuned depending on requirements [163,178]. MOS transistors can be stacked to enhance response. Various types of RadFETs are able to measure doses from µGy to kGy with a different accuracy [162].

The MOS-based dosimeter is sensitive to the temperature and annealing, therefore the readout system used to evaluate ionizing radiation measurements should take these facts into consideration [179, 180]. The sensitivity of the RadFET dosimeter can be modified when exposed to a high neutron fluence [181, 182].

Bipolar transistors are slightly sensitive to radiation, therefore this technique is more suitable for doses near a few kGy [162].

Semiconductor memory

High capacity Random Access Memories (RAMs) consist of a large number of MOS transistors. Memories suffer because of SEUs when exposed to neutron or ionizing radiation (Chapter 2.2.3). A dynamic random access memory (DRAM) was proposed to be used as an alpha-particle counter, calculating a number of SEUs generated in the memory [183–186]. The top part of the memory package has to be removed to allow a deep penetration of the sensitive volume by alpha particles. The particle has a very short range in silicon and silicon dioxide, roughly a few µm, therefore the thin memory package filters the incident particles efficiently. The application of an additional ^{10}B or ^{6}Li-based converter foil allows to detect thermal neutrons [186, 187]. The foil was put on the silicon die of the DRAM. Despite the modification, the DRAM still had an insufficient sensitivity to neutrons. The susceptibility of the memory was significantly improved by the chemical etching of the DRAM die passivation layer and

the installation of the foil converter directly on the silicon die [188].

The sensitivity of the DRAM can be enhanced by lowering the supply voltage, increasing the refresh frequency, an application of a suitable pattern written into the chip or using higher capacity memories [188]. DRAM chips were used because of a higher sensibility to SEU than SRAM. The sensitivity of the memory strongly depends on the particle's energy.

SRAM devices were mainly used to detect charged particles, i.e. protons [169, 189]. A dedicated memory structure was designed and produced as an integrated circuit chip to detect protons fluence in the space environment that was used during the Clementine mission [174, 175]. The device was used as a proton spectrometer at the Clementine experiments. Static memory was also applied to design a miniature high-let radiation spectrometer for space and avionics applications [190].

A 4 kbit SRAM matrix was employed to design a tissue-equivalent (TE) personal dosimeter [191, 192]. The sensitive area of the detector was composed of reverse-biased p-n junctions that operated as a small ionizing chamber similarly to above-mentioned diode-detectors. There is no information about the detector's sensitivity and calibration factor. The presented detector was applied to detect neutrons, however the used technique caused that it was also gamma sensitive.

Diamond detectors

Diamond detectors are dedicated to high dose rate or harsh environments. Their detecting ability is rather poor, therefore they can also be used only for monitoring strong sources [150]. The detector functions as a small ionizing chamber composed of a thin diamond plate surrounded by aluminium electrodes. The detector can be used for ionizing particles and neutron detection [162].

4.1.3 Scintillators

A scintillator counter can be used to detect gamma radiation or X-ray. Moreover, an application of a suitable conversion layer allows to detect thermal and fast neutrons [161, 193–195]. Incident photons passing through a scintillator generate electron-hole pairs and cause an excitation of atoms. Blue or ultraviolet light is usually emitted as a result of their recombination. Scintillators can be made of liquid or solid organic or inorganic materials, like: thallium-activated sodium-iodine NaI(Tl) or caesium-iodine CsI(Tl), sodium-activated caesium-iodine CsI(Na), bismuth-fluoride BaF_2 and gadolinium orthosilicate (GSO) [22, 150]. The scintillator cooperates with a photomultiplier or a photodiode that converts emitted light pulses into electrical signals. The cross-section view of a scintillator counter is depicted in Figure 4.3. An application of the photomul-

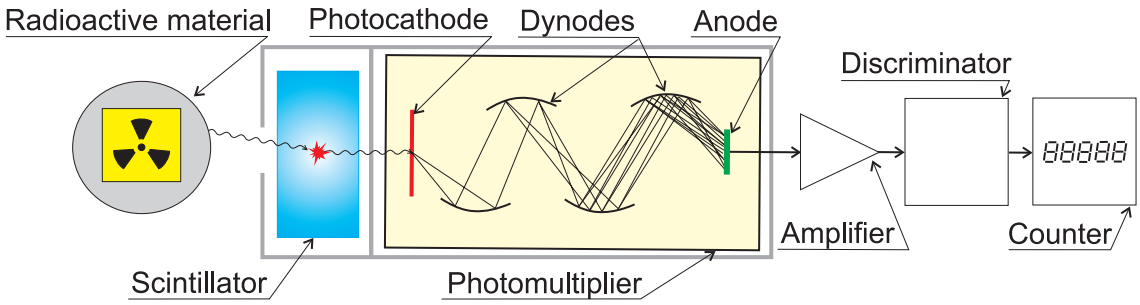

Figure 4.3: *A cross-section view of a scintillator counter [22].*

tiplier allows to obtain a very good sensitivity, high efficiency and fast response of the whole instrument [152]. Scintillators are primarily used as photons or particle counters, however the operation in the proportional mode allows to serve as a dosimeter. Some scintillators reveal dependence on the incident particles energy [146, 147].

4.1.4 Activation foils

Activation foils make usage of induced activity in one or more carefully chosen and purified materials [21]. Therefore this type of dosimeters is chiefly used for the measurement of neutrons. During the irradiation of a sample foil manufactured of high purity materials, the concentration of the radioactive nuclei accumulates. The population will decay when the foil is removed from the radioactive environment. Thus, the measurement of the induced radioactivity in the foil allows to quantify the absorbed dose. Radioactivity generated in the foil can be measured using a precise instrument for gamma or beta dosimetry, i.e. a scintillation detector [196]. Relatively intense neutron fluxes are required to induce enough radioactivity and permit the reasonably accurate measurement. Activation foils are used to measure large doses around accelerators, reactors or other strong sources of neutrons [197]. Slow neutrons can be measured using silver, indium and gold foils, while iron, magnesium and aluminium are suitable for the detection of fast neutrons [21].

Activation foils have advantages of low complexity, no sensitivity to gamma radiation, small size and easy calibration [150]. Moreover, foils are able to tolerate exposure to extreme temperatures, shocks and magnetic fields. The main disadvantage is the low sensitivity depending upon the neutron cross-section [198].

4.1.5 Bubble dosimeters

A bubble or superheated droplet detector is made of a suspension of tiny droplets (e.g. freon) in a clear polymer [199]. Surface tension forces prevent superheated droplets from evaporation. However, when a neutron collides with a droplet, the droplet sud-

denly vaporizes creating a visible gas bubble trapped in gel [150]. A bubble detector is primarily sensitive to neutrons because gamma photons are not able to deliver enough energy to overcome the surface tension forces. The amount of created bubbles is proportional to the number of neutrons colliding with the dosimeter, thus the calibrated bubble detector immediately gives incident neutron intensity [152].

The dosimeter can be reused when the increased pressure inside the detector causes a transformation of all bubbles into superheated droplets. Bubble dosimeters are selectively sensitive to low levels of neutron fluences, energy independent in limited range and relatively cheap. However, counting of bubbles can be difficult and arduous especially for larger neutron doses. The detector can be applied for an on-line fluence measurement, albeit the advanced counting system must be used [165,200]. The amount of bubbles may be delivered by analysing various photographs of the detector or counting acoustic spikes generated during the bubble formation. Dosimeter reveals strong temperature dependence [199,201]. However, temperature compensated bubble dosimeters are also accessible.

4.1.6 Chemical dosimeters

Chemical dosimeters make use of the inducing of chemical reactions in the absorbing medium. A large number of chemical dosimeters is known, that allows to measure gamma and neutron radiation. Radiation can cause a chemical change and result in the modification of chemical, physical or optical properties of the irradiated dosimeter. Chemical dosimetry usually requires using dedicated hardware (like spectrometers) and various chemicals to evaluate the absorbed dose. The methods are dedicated to the measurement of high doses and can be used in mixed radiation environments. Exemplary chemical dosimeters are: amino acid alanine, Fricke, thiocyanate, dichromate, ethanol-chlorobenzene and perspex detectors [21,22,142,146,147,202]. The attenuation of an optical fibre is enhanced when is exposed to ionizing radiation. This feature allows to design a distributed radiation monitoring system using a long optical fibre [203].

4.1.7 Calorimetric dosimeters

The calorimeter is based on the measurement of the energy deposited as heat in a thermally isolated mass [142]. Different absorbing materials are used as a target mass for the gamma and neutrons detection, i.e. silicon or carbon. The thermal characteristics of the material must be known. Small absorbers made of good thermal conductors may be used to assure a rapid achievement of the thermal equilibrium, e.g. beryllium, aluminium, copper, silicon [21]. The temperature is usually measured using thermocouples, thermistors or silicon detectors, which have similar atomic numbers to the

absorbing materials.

A calorimetric method is independent from particles' energy, total dose and dose rate, and therefore allows to obtain reliable measurements. Even if it is a simple device, the radiation measurement process and calibration are very complex. Dynamic energy absorption, heat transfer and heat losses should be taken into consideration. Because of a small temperature increase, advanced methods are used to calculate absorbed dose. A high dose of radiation is necessary to cause a noticeable temperature rise. The measurement is much more complicated in mixed radiation environments [146].

4.1.8 Thermoluminescent materials

Certain crystalline materials exhibit a thermoluminescence. TLD dosimeters can be sensitized for gamma radiation as well as neutrons. The advantage of this phenomenon was utilised to design a thermoluminescent (TLD) dosimeter. Materials used for TLD dosimeters are: lithium fluoride (^{7}LiF), calcium fluoride (CaF_2), calcium sulphate ($CaSo_4$), lithium borate ($Li_2B_4O_7$), beryllia (BeO) and alumina (Al_2O_3) [22]. Electron and hole traps present in TLD crystals are filled when the TLD sample is exposed to radiation. Most of them immediately return to the ground state, however a few remain permanently trapped in impurity levels. Trapped charges can be released during the TLD heating up. Light is emitted when free electrons and holes recombine. Generated light intensity depends on the amount of the trapped charge, which is proportional to the quantity of the energy absorbed from radiation, as well as on the temperature, used material and content of impurities. The absorbed radiation dose can be measured by the integration of the glow curve obtained during a monotonous heating up of the TLD. A TLD reader and the thermogram (glow curve) obtained for the LiF:Mg,Ti dosimeter are presented in Figure 4.4. The fading of the glow curve does not exceed a few per cent. Glow curves shown above were measured immediately, 4 and 20 days after the exposure, see Figure 4.4 [153].

TLD dosimeters can be reused after the readout. They must be annealed by heating at a high enough temperature (300-400 °C). However, their sensitivity is not constant and when high precision is required, dosimeters should be recalibrated.

TLDs are subject to fading, the dose of radiation is decreasing with time. Dosimeters should be read immediately after the exposure or a suitable correction should be applied [21].

TLD exhibits radiation energy dependence, therefore measurements in mixed radiation environments are more complicated. However, an application of various TLD dosimeters with different shielding materials (filters) allows to distinguish between the two radiation types and to measure the dose correctly [22]. Some of dosimeters have

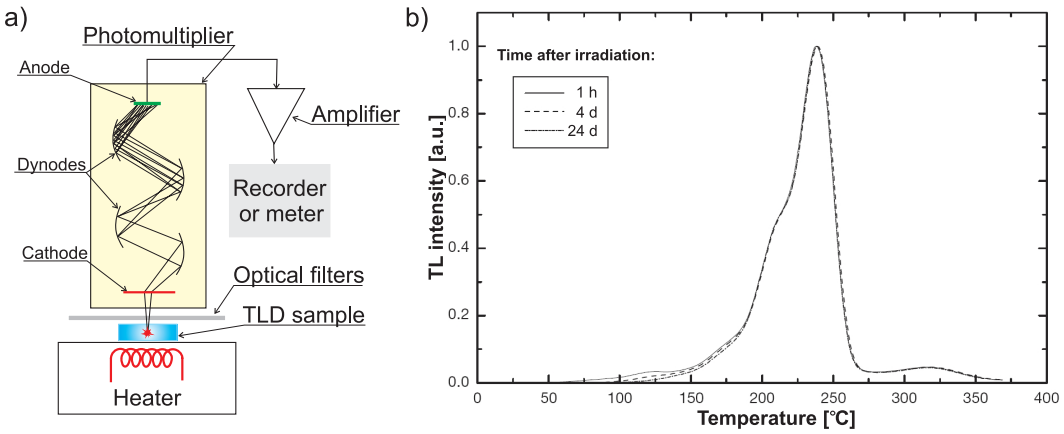

Figure 4.4: *TLD dosimetry: a) a TLD reader and b) a thermogram of LiF:Mg,Ti measured with a TLD reader [142, 153].*

a very high sensitivity to thermal neutrons (e.g. TLD-600), thus they cannot be used to measure radiation in an accelerator tunnel. Thermal neutrons present in the tunnel cause a fast saturation of TLDs or significantly falsify the results [1-A].

For the measurement of radiation in a linear accelerator tunnel a pair of dosimeters (TLD-500, TLD-700) can be used [1-A]. Dosimeters reveal an enormous sensitivity and linearity for small doses of radiation, therefore, they can be used during the calibration.

4.1.9 Photographic dosimetry

A photographic dosimetry is based on a transparency deterioration of photographic emulsions, plastic films or other materials. Emulsions consist mainly of a suspension of silver halide grains in an inert gelatine matrix. Incident ionizing radiation passing through the emulsion produces a similar effect as seen with the exposure to visible light due to interactions with silver halide molecules [146]. The transparency of radiographic films exposed to ionizing radiation is decreased as a general darkening of the film because of the cumulative effect of many radiation interactions in a given area of the emulsion [153]. The attenuation of light passing through the film can be measured using a photometer and therefore the absorbed dose of radiation can be estimated [147]. Photographic methods can be also used for fast neutrons dosimetry. The idea of this method is based on counting recoil protons during the irradiation of materials including hydrogen [146]. Photographic dosimetry is rarely used because of high complexity and inaccuracy.

4.2 Real-time radiation monitoring systems

The real-time radiation monitoring system of the National Synchrotron Radiation Research Center (SRRC) in Japan is installed in the third generation light source driven by a 50 MeV linac and 1.5 GeV synchrotron booster. The system consists of high-pressure ionization chambers used as a gamma-ray dosimetry and moderated BF_3 or ^{3}He rem counters for the neutron detection [15]. Signals from radiation detectors are collected by local computers and sent via the computer network to the main server. All data are accessible through web services.

The radiation monitoring system of 27 km long Large Hadron Collider (LHC) is dedicated to the real-time monitoring of the total ionizing dose TID, neutron fluence and hadron detector. Contrary to the SRRC, the system utilises semiconductor detectors. A RadFET sensor was used for the measurement of TID, a silicon photodiode acts as a neutron fluence sensor and Toshiba 512 kB memory chip functions as a hadron detector [204]. The sensors cooperate with the radiation tolerant readout system built using old TTL circuits. Measured data are sent to the main computer through the WorldFIP field bus. Current limiting circuits were applied to secure the most crucial integrated circuits against SEL [205]. The LHC collider and the monitoring system are currently under construction.

4.3 Conclusions

Principles of various radiation detectors and dosimeters was presented in Chapter 4.1. Detectors that are suitable for the on-line radiation monitoring system should assure a fast and accurate enough for radiation measurement. These requirements disqualify the usage of chemical, calorimetric, activation foils and photographic film dosimeters. Moreover, detectors should correctly discriminate the measured type of radiation, keeping in mind that the amount of produced gamma radiation in a linear accelerator is a few orders of magnitude higher than the neutron fluence. Therefore, gas-filled neutron dosimeters and scintillators can supply inaccurate results in such a situation. In addition, devices require a high voltage to operate. Some of the detectors display also problems in a pulsed environment of a linear accelerator because of limited recovery time. TLDs require a complicated procedure to unfold absorbed doses in gamma-neutron mixed fields. Bubble dosimeters can be utilised for an on-line monitoring, nonetheless they have a limited lifetime and relatively long resetting time.

Keeping in mind mentioned earlier requirements, the most suitable sensors for the real-time monitoring system seem to be semiconductor dosimeters. The measured dose of a silicon sensor can be directly compared with damage of the installed in tunnel

systems. Most of the silicon dosimeters produce analogue or digital signal proportional to the radiation dose, thus the devices can easily integrated with an electronic readout system. The detectors are made of silicon, hence measured radiation can be directly compared with damage of digital systems installed in the accelerator, while other dosimeters are produced with the usage of hydrogen rich materials in order to imitate biological damage and calibrated regards to the tissue equivalent procedure [22].

TLD and bubble dosimeters are useful tools for calibration of the on-line radiation sensors.

Chapter 5

The distributed on-line radiation monitoring system

The radiation monitoring system, called RadMon, will be installed in a linear accelerator tunnel to gauge IEL and NIEL radiation doses. Ionizing damage is mainly caused by gamma radiation, while neutron particles are responsible for displacement damage, see Chapter 2. The system will be subjected to TID, displacement damage and SEE because of gamma radiation and neutrons present in the tunnel during the operation of a linear accelerator. Therefore, the construction of the system should allow to operate properly in a mixed radiation field.

The application of RadMon may be helpful to estimate and analyse IEL and NIEL damage in electronic components used to design linear accelerator's control systems [3-A]. Due to the fact that most of electronic components are produced using silicon, it is preferable to measure a gamma radiation dose with the reference to the dose absorbed by silicon dioxide and neutron fluence should reflect damage in silicon.

5.1 Requirements for the radiation monitoring system RadMon

There is a strong need to measure both types of radiation, i.e. an absorbed gamma dose and neutron fluence in real-time. Therefore, applied neutron and gamma radiation sensors should allow to quantify accumulated doses and dose rates of radiation present in a linear tunnel. Sensors should have small sensitive volumes to ensure uniform response over the active area. Detectors must measure radiation correctly in the pulsed radiation environment of the VUV-FEL or X-FEL facilities. They should have good enough sensitivity and dynamic ranges. The readout device of the radiation monitoring system should be preferably equipped with a digital interface to enable easy connection

of the system to a computer network. Therefore, data measured in a few different places through a linear accelerator can be sent to a main computer and gathered in a database for future display and analysis. The construction of the system should give an opportunity for further extension. Above all, the construction of the system should be cost-effective.

Requirements concerning radiation measurement for RadMon are gathered in Table 5.1

Requirements for radiation monitoring system	
Detection ability	Neutron fluence and gamma radiation dose
Fluence range	10^6 – 10^{10} neutron·cm^{-2}
The lowest fluence	10^4 – 10^5neutron·cm^{-2}
Dose Range	10^2 – 10^3 Gy
The lowest dose	10^{-3} – 10^{-2} Gy
Energy range	up to 20 MeV

Table 5.1: *Requirements for RadMon's on-line radiation monitoring dosimeters.*

Silicon sensors were taken into consideration as candidates for the gamma radiation dose and neutron fluence dosimeters. RadFET transistors can be utilised as a gamma dosimeter. Sensors are accessible with different sensitivities relating to the thickness of the silicon dioxide structure. The output analogue signal from the sensor can be easily converted into digital data and connected to the readout system. A PIN diode may act as a neutron sensor. Nevertheless, neutron fluence in the VUV-FEL accelerator is relatively low and the sensitivity of the detector is not satisfactory ($0.4\ \mathrm{V}/10^{11} n \cdot cm^{-2}$) [172, 173]. Silicon SRAMs disclosed a high neutron vulnerability during radiation sensitivity tests of electronic components carried out at DESY accelerator centre [5-A, 14-A, 15-A, 16-A, 17-A]. My research shows that SRAM chips, similarly to DRAMs, suffer because of SEUs provoked by incident neutrons. An application of DRAM memories for the neutron dosimetry was described in Chapter 4.1.2. Detectors characterised in the literature require to remove the memory package and install an additional converter foil directly on the silicon structure [186–188]. An application of the boron or lithium foil was indispensable to enhance the sensitivity of the detector. Despite a large number of virtues, the described process is very complicated and requires specialised hardware. Indeed, an application of ^{10}B or ^{6}Li-based converter foils results in a very high sensitivity to thermal neutrons of the dosimeter.

A SRAM-based sensor has a big advantage because gamma radiation is not able to trigger a SEU [14-A, 16-A][1]. Moreover, memories are always equipped with a digital interface, thus can be easily connected to a digital readout system [54]. Experiments

[1]SEUs can be triggered only by very energetic gamma photons with energies higher than 500 MeV.

performed in DESY allow to use a selected SRAM chip as a fast neutron fluence dosimeter without complicated modifications of the chip. Moreover, SRAMs sensitivity, similarly to DRAMs, should be enhanced in a natural way when the number of memory cells is increased [184].

Indeed, RadFET and SRAM memories are cost-effective solutions and therefore the on-line monitoring system can be distributed inside the long accelerator tunnel. Moreover, the number of SEUs generated in SRAM can be directly compared with soft errors induced in the accelerator's digital system. Dosimeters can be used for a dose rate and an absorbed dose real-time monitoring.

The monitoring system may be utilized as a interlock detector, therefore the desired fluence measuring time should be better than 150 ms [206]. In such a case an application of a large RAM memory can causes a problem because of the long scanning time, for example the scanning time for a 2 MB SRAM memory with 70 ns access time is roughly 140 ms (not counting the comparison and preprocessing data procedures).

RadFET as well as SRAM memory have a limited lifetime. The maximum measured dose for RadFET dosimeter depends on the gate oxide thickness and the maximum allowed input voltage of the readout circuit. However, there is always a compromise between the sensitivity and the maximum measured dose. The maximum dose of the SRAM sensor is primarily restricted because of TID damage effect. The detectors used to design the monitoring system and their limitations will be discussed in Chapter 5.2 in details.

5.2 The architecture of the radiation monitoring system RadMon

The radiation monitoring system is composed of two modules: radiation sensitive sensors and the radiation tolerant readout circuit able to operate correctly in the radioactive environment of the linear accelerator. The block diagram of the radiation monitoring system is presented in Figure 5.1. Measured gamma radiation and neutron fluence in the accelerator's vault are transferred to a PC computer placed outside the tunnel in a safe, non-radioactive area and then gathered in a database. Data should be accessible via the www interface and distributed object oriented control system DOOCS system.

The RadMon system is going to be built with an application of commercial-off-the-shelf components (COTS) because of the extremely high costs of the dedicated radiation-hardened hardware. Digital devices exposed to radiation suffer mainly because of TID, displacement damage effect and SEE, see Chapter 2. The system can

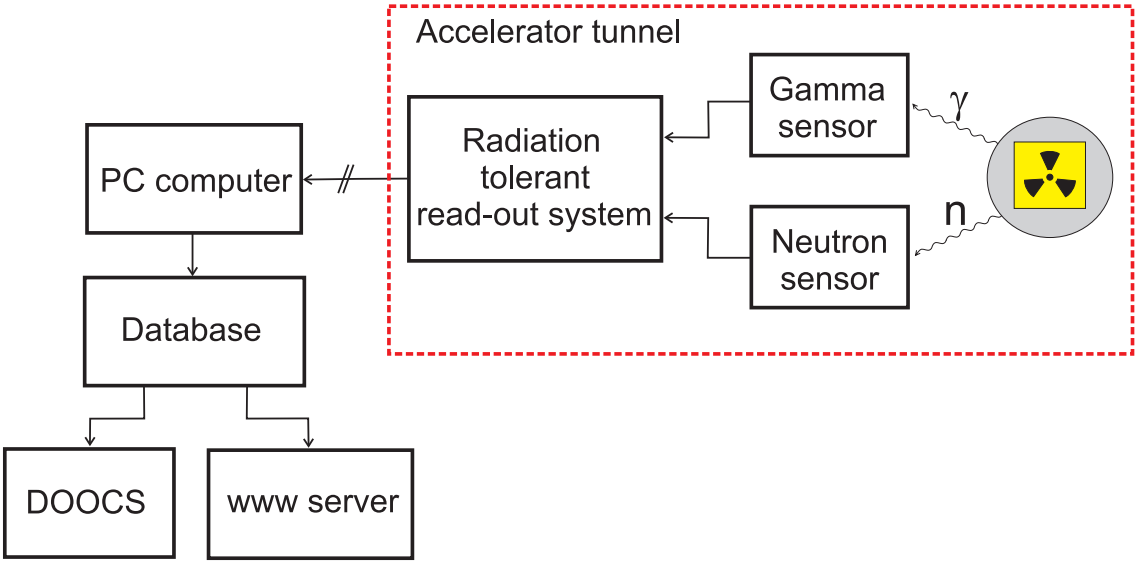

Figure 5.1: *The block diagram of the radiation monitoring system RadMon.*

be designed to tolerate errors provoked by radiation, however the lifetime of the whole system is limited because of the maximum allowed dose of ionizing radiation for used electronic components and displacement damage. The lifetime of the system can be extended when the proper shielding against radiation will be employed. Moreover, the device can be constructed with an application of selected devices that are able to tolerate relatively high doses of radiation. Information about radiation resistivity of some electronic component can be found in specialised research centres, e.g. CERN, NASA [207–209]. The system may be designed in such a way that it can tolerate SEEs, in particular SEUs and SELs when COTS elements are used. Therefore, the deployed mechanisms and algorithms allow to operate in the linear accelerator environment.

Different versions of the readout were designed, built and given a thorough examination. The systems and the methodology of design such a devices are presented in Chapter 7.

Chapter 6

Neutron fluence and gamma radiation sensors

The primary sensor, neutron dosimeter, was constructed with an application of a commercially available SRAM chip [18-A]. Standard memories manufactured by diverse manufacturers reveal different SEU sensitivities to neutron radiation. Some of them are very susceptible to high energy neutrons, another to thermal neutrons. Memories with ECC circuits are much more SEUs resistant and therefore cannot be used as a neutron fluence detector. A large number of miscellaneous memories were examined with an application of an ^{241}AmBe(α,n) americium-beryllium neutron source to select the most suitable SRAM as a neutron dosimeter. Auxiliary irradiations were performed initially in Linac II and later in VUV-FEL accelerator tunnels. The research allows to better understand the mechanism of SEU and draw up suitable methods to increase the sensibility to SEUs and therefore enhance the sensitivity of the dosimeter. The list of tested SRAM and NVRAM devices is presented in Table 9.1.

A RadFET dosimeter was chosen as a secondary gamma radiation sensor. The detector and dedicated readout system are described in Chapter 6.2.

6.1 SRAM-based neutron detector

Two types of random access memories were examined, i.e. non-volatile (NVRAMs) and conventional SRAMs. Both types of memories cooperated with dedicated readers. Non-volatile devices have been used during off-line experiments, while SRAMs have been employed for radiation measurement in real time. NVRAMs manifested to be very helpful in the initial stage of the research and when an additional moderator was designed. The readout systems used to control and evaluate memories are presented in Chapter 7.

A suitable pattern was written into the memory chip before the irradiation. Then

the memory was subjected to neutron radiation influence. The data were read and then compared with the pattern after the exposure. A number of SEUs generated in the memory was calculated for a given period of time or neutron fluence.

6.1.1 Radiation sensitivity tests

Radiation sensitivity tests of NVRAM and SRAM devices were carried out at DESY institute in Hamburg. Part of the experiments was performed in the tunnel of the pulsed mode linear accelerator Linac II. The accelerator supplies electrons and positrons for Petra and Hera experiments. Electrons produced by the electron gun are accelerated up to 450 MeV and then collected in the PIA ring (Positron Intensity Accumulator) when the accelerator is operated in the electron mode. Positrons are produced using the electron-to-positron (e^-/e^+) converter during collisions of electrons with the tungsten target of 9 cm in diameter. Positrons are also accumulated in the PIA ring for further experiments. Two types of radiation are mainly produced during the operation of 450 MeV linac: photoneutrons and bremsstrahlung gamma. Memories were irradiated when the electron-to-positron converter was utilized. The dedicated radiation dosimetry is not supported in Linac II, therefore accurate measurements of neutrons and gamma radiation dose produced during accelerator's operation are impossible. TLD and bubble dosimeters were used during the memories irradiation. A pair of TLD-500 (aluminium oxide) and TLD-700 (lithium fluoride) dosimeters were used to measure absorbed doses during exposures: neutron silicon kerma and gamma dose [1-A, 14-A]. The TLD-500 is sensitive to gamma rays, while TLD-500 reveals the response to neutron and gamma radiation. An interpretation of glow-curves of both TLDs after the exposure allows to calculate the doses of both radiations. However, a large gamma background prevents to measure the neutron fluence accurately. The TLD-500-gamma sensitive dosimeter registered a large gamma dose, while the TLD-700 response to neutrons was weak during the irradiation in Linac II.

The significant amount of photoneutrons and bremsstrahlung gamma are produced during the bombarding a tungsten converter with 450 MeV electrons. The neutron spectrum of Linac II is not well known, however an approximate shape has been proposed [1-A]. The spectrum is illustrated in Figure 6.2.

A calibrated water-moderated americium-beryllium ^{241}AmBe (α,n) neutron source was applied during further exposures [17-A]. The setup employed during irradiation tests is presented in Figure 6.1 [17-A]. The cylindrical neutron source was placed on a 16 cm high aluminium tripod in the centre of two 32 cm high nylon jars with the external diameters equal to 14 cm and 32 cm respectively. The device under test (DUT) was installed outside the external jar at the height of the neutron source using

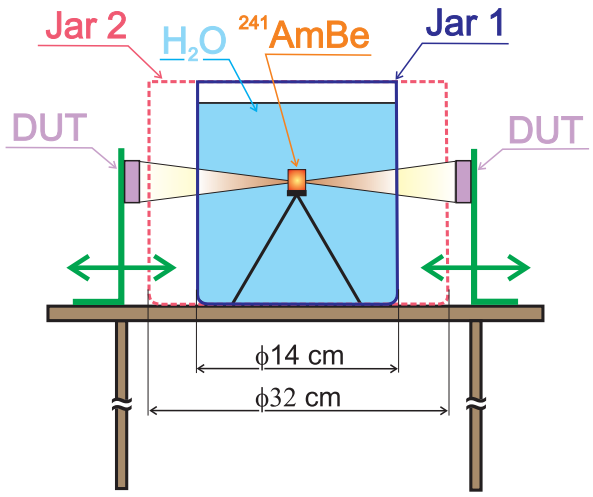

Figure 6.1: *The irradiation facility for testing electronic components and systems.*

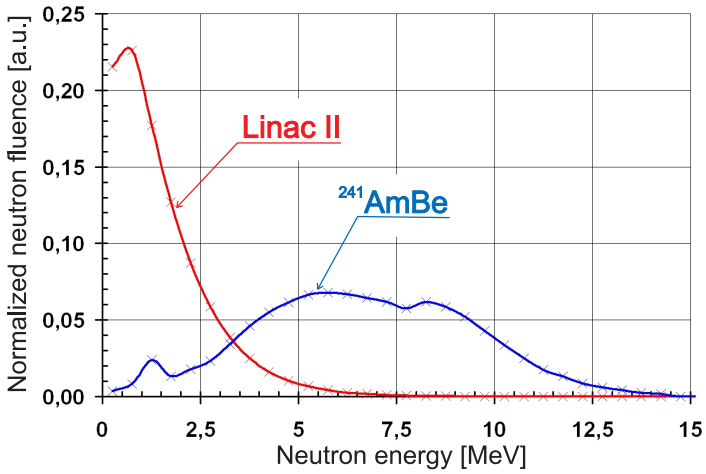

Figure 6.2: *Energy spectra of* ^{241}*AmBe neutron source and Linac II.*

a removable angle. The space in the jar surrounding ^{241}AmBe was filled with deionised water. An application of two jars with different dimensions allows to use different water moderators and exploit different neutron spectra [210]. The water moderator was applied to slow down the neutrons generated by ^{241}AmBe and modify their energy spectrum to imitate the spectrum of Linac II. The original energy spectrum of ^{241}AmBe is depicted in Figure 6.2, whereas water-moderated spectra of americium-beryllium can be found in Appendix 9.2 [1-A].

6.1.2 NVRAM-based neutron detector

A non-volatile random access memory (NVRAM) consists of a standard low power CMOS SRAM device, lithium battery and a power supply supervisory circuit. Components are housed in an epoxy resin moulded package. The supervisory circuit assures write protection and power backup when the external power supply is disconnected.

a)

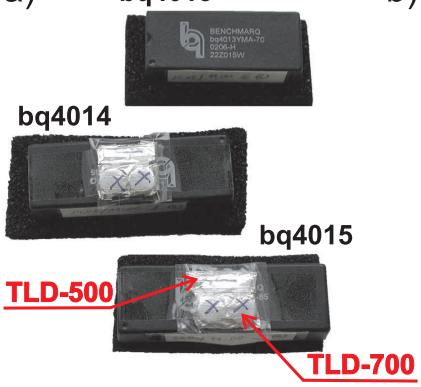

b)

	Configuration memory	Conf. data size
0x000	Memory density	[1B]
0x032	Memory signature	[4B]
0x0FA	Calibration factor	[4B]
0x1C2	Date of first usage	[4B]
0x28A	Accumulated SEU	[4B]
0x352	Written pattern type	[1B]
0x384	CRC 16	[2B]
0x3E8	Spare space	[24B]
0x400	Main memory area	[1B]
.		[1B]
.		[1B]
.		[1B]
.		[1B]

Figure 6.3: *Neutron sensitive NVRAM chips, a) prepared for the irradiation with the accompanying TLD dosimeters, b) a map of the configuration memory.*

Therefore, a SRAM-based chip behaves as a non-volatile memory allowing to carry out off-line experiments. NVRAMs with 128, 256 and 512 kB capacities equipped with TLD dosimeters are presented in Figure 6.3. The lithium battery is able to supply data retention for 10 years.

A selected, known digital pattern must be written into the NVRAM before the irradiation. A dedicated memory reader, able to operate memories supplied from 2 to 5 V, was constructed to assure fast programming and evaluation of memories subjected to radiation [16-A]. Their operation is performed in the non-radioactive environment before and after the exposure, thus the reader is not required to be radiation tolerant. Two types of information are stored in a non-volatile memory: the above-mentioned pattern written into the main sensing memory and 1 kB of configuration data, see Figure 6.3 [16-A]. The configuration data, contrary to the main memory, must be radiation immune. The configuration data describes the memory capacity, its signature, a type of pattern used during the programming, a total number of generated SEUs, the calibration factor, the date of the first usage and the 16-bit CRC control sum. These data were utilised for the automatic configuration of the reader. Data translated into the binary words are stored in the first kilobyte of the memory using redundancy to ensure its correctness. Data, depending on its function, occupy multiple of single, double or quad bytes depending on the used redundancy. The data are written into memory chip during formatting and always read during the evaluation. The amount of used redundancy for the following memory parameters can be easily changed in the reader's properties during memory formatting. The configuration was secured using fifty-times redundant data during experiments in Linac II and with ^{241}AmBe, as presented in Figure 6.3. Some of the configuration data are necessary to read and evaluate the memory contents after the exposure, e.g. memory capacity, used pattern.

NVRAM reference	Memory capacity	Applied SRAM memory	Supply voltage	SEU Cross-section ($cm^2 \cdot bit^{-1}$)
NVRAMs manufactured by Texas Instruments				
bq4013MC-70	128 kB	HY628100B-55	5 V	2.32×10^{-13}
bq4014MC-70	256 kB	-	5 V	2.80×10^{-13}
bq4015MC-70	512 kB	K6T4008C1B-VB55 R1LP0408CSB-5SI	5 V	2.94×10^{-13} 2.90×10^{-15}
bq4016MC-70	1 MB	2xK6T4008C1B-VB55 2xR1LP0408CSB-5SI	5 V	2.61×10^{-13} 2.8×10^{-15}
bq4017MC-70	2 MB	4xK6T4008C1B-VB55 4xR1LP0408CSB-5SI	5 V	2.35×10^{-13} 2.5×10^{-15}
NVRAMs manufactured by Maxim (Dallas)				
DS1249AB-85	256 kB	M5M51008DVP-55H1	4.75-5.25 V	4.06×10^{-15}
DS1270W-100	2 MB	-	3.0-3.6 V	3.48×10^{-15}

Table 6.1: *The characteristics of tested NVRAMs with measured SEU cross-sections.*

The configuration data are recovered using a voting technique in the case of detected error or CRC discrepancy before reading of the sensing area of NVRAM. Recovered data are immediately rewritten to avoid accumulating errors. A SEU detected in configuration part of NVRAM can be also considered during reading. A calibrated NVRAM can act as a neutron fluence dosimeter. The calibration factor is then used to translate the number of generated SEUs into the neutron fluence. Both the date of first memory usage and the total accumulated number of SEUs can be helpful to estimate the memory's lifetime.

An application of NVRAM configuration facilitates the evaluation process of irradiated memories and significantly reduces the number of mistakes during reading [16-A].

Irradiation sensitivity tests of NVRAM

Some experiments with NVRAM memories were carried out in the Linac II tunnel. Then, the relationship between generated in memory SEUs and neutron fluence was observed for the first time. However, the measurement of neutron fluence during the exposure was difficult because of limited access to the accelerator. Therefore, calibrated ^{241}AmBe was used for further experiments. The neutron emission of the source is equal to 2.2×10^6 n$\cdot$s^{-1} per Ci. The energy spectrum of the source is depicted in Figure 6.2 and detailed data are presented in Appendix 9.2. Various NVRAMs, manufactured by Texas Instruments and Maxim, supplied from 3.3 and 5 V were used during experiments. Table 6.1 summarizes the most important parameters of NVRAMs. Memories were subjected to neutrons obtained from water moderated americium-beryllium, the

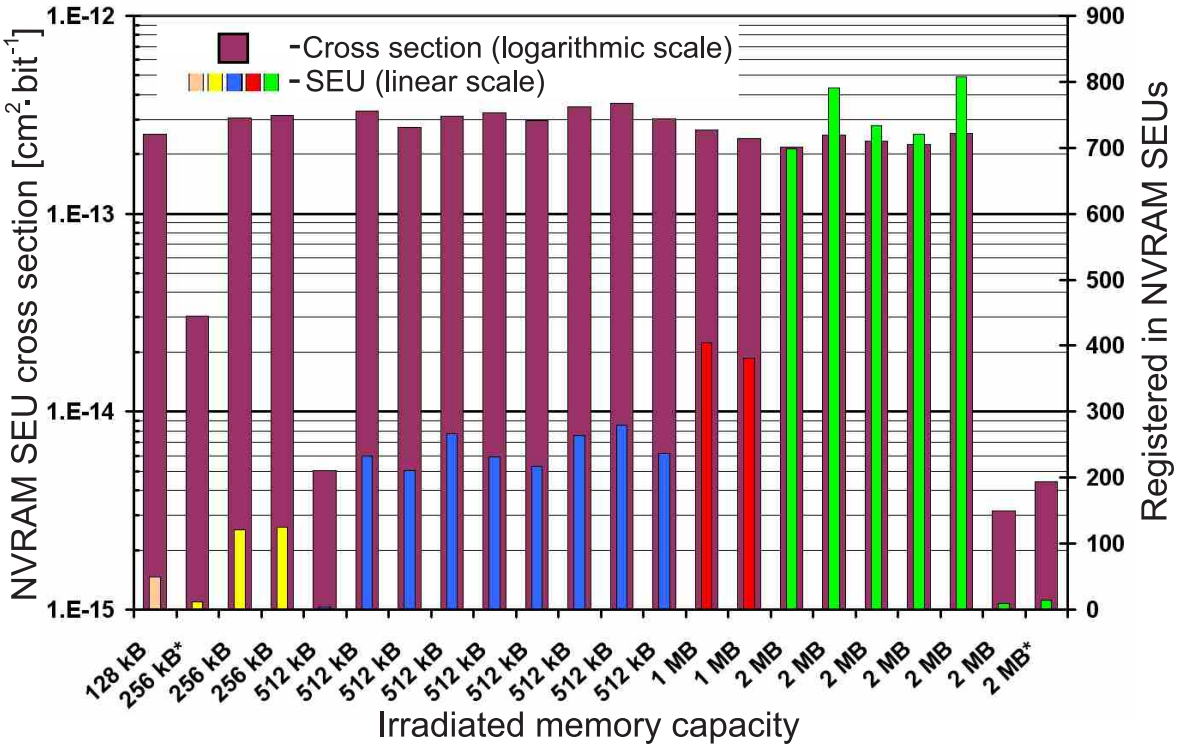

Figure 6.4: *The comparison of SEU cross-sections of NVRAMs and generated SEU during irradiation with AmBe.*

thickness of the moderator was equal to 6.9 cm. The exposures were carried out in a restricted access area during 24 hours. The memories were supplied from the internal 3 V lithium battery. After irradiation, the devices were read and the number of SEUs was calculated. The results are exemplified in Figure 6.4. The probability of single bit flip for the memory with capacity D is determined by the SEU cross-section σ_{SEU} that can be calculated using Equation 6.1 and expressed in cm^2·bit^{-1}.

$$\sigma_{SEU} = \frac{N_{SEU}}{D \cdot \Phi \cdot}, \tag{6.1}$$

where N_{SEU} corresponds to the total number of generated SEUs, fluence Φ defines the number of neutrons passing through a unit area during irradiation. One can calculate fluence Φ for period of time Δt, when fluence rate ϕ for a given neutron source is known:

$$\Phi = \int_0^{\Delta t} \phi \cdot dt, \tag{6.2}$$

Fluence rate for the used neutron source in the completed experiment was equal to $2.38{\times}10^3$ n·cm^{-2}·s^{-1}, see Appendix 9.2. The calculated SEU cross-sections for the tested NVRAMs are presented in Figure 6.4 (logarithmic scale). The memories fabricated by Maxim (Dallas) are marked with asterisks. Most of the examined memories manufactured by Texas Instruments (TI) have similar SEU cross-sections, in range of

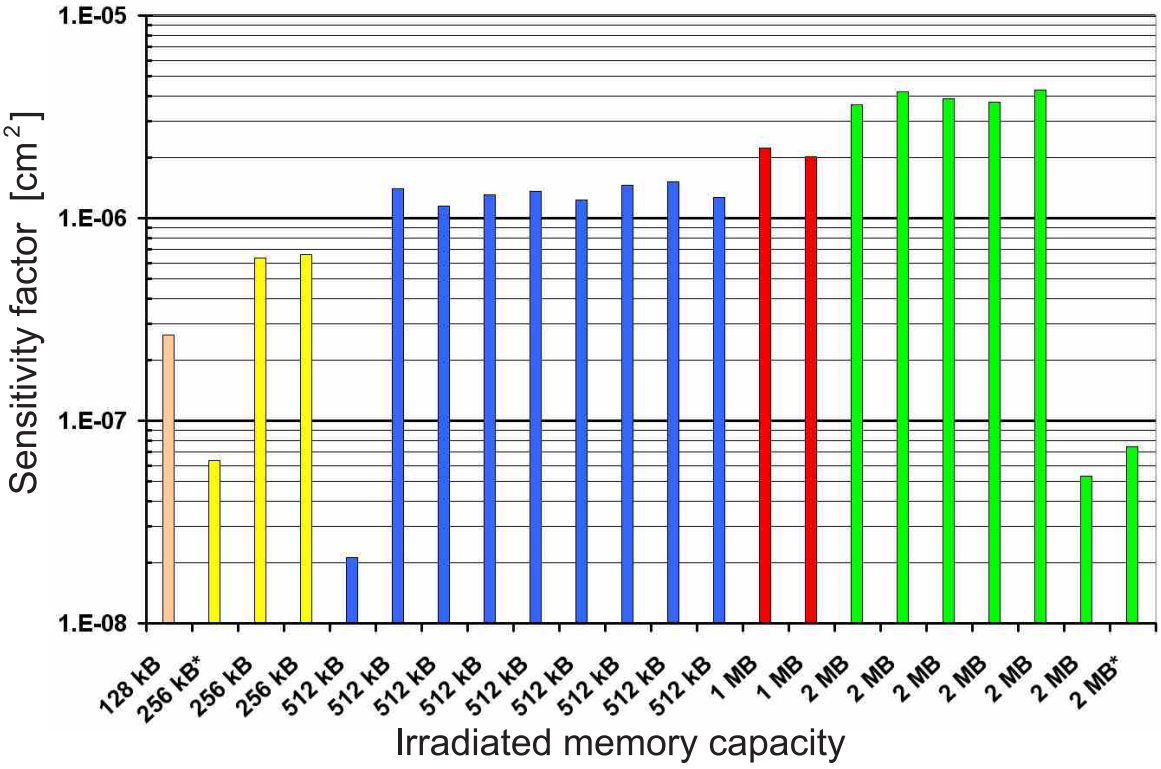

Figure 6.5: *Sensitivity factors for the examined NVRAM chips.*

10^{-13} cm$^2\cdot$ bit^{-1}, however other chips reveals sensitivity that is two orders of magnitude lower. For example 512 kB bq4015 TI memories have SEU cross-sections equal to 5×10^{-15} and 3.5×10^{-13} cm$^2\cdot$ bit^{-1}. The SEU cross-sections of low capacity memories, i.e. 256, 512 kB were slightly better that the ones calculated for 2 MB chips, see Figure 6.4. The sensitivities of memories produced by Maxim were rather poor (approximately 10^{-15} cm$^2\cdot$ bit^{-1}). The sensibility of memories to SEUs is crucial from the point of view of SRAM-based neutron sensor. Thus the sensitivity factor (SF) S was introduced by multiplying memory capacity D by calculated SEU cross-section σ_{SEU}, which is the figure of merit of SRAM-based neutron detector performance:

$$S = \sigma_{SEU} \cdot D \tag{6.3}$$

The SFs calculated for the NVRAM chips are shown in Figure 6.5. As expected, the highest capacity 2 MB memories reveal highest sensitivity to neutrons. However, two of the tested 2 MB memories have very low vulnerabilities. One of them was manufactured by Maxim and the others by TI. Consequently, other devices with low cross-sections were characterised by low sensitivity factors. Further research showed that new memories with various densities manufactured by TI also have SEU cross-sections in range of 10^{-15} cm$^2\cdot$ bit^{-1}.

The average number of SEUs generated in memories with different capacities was

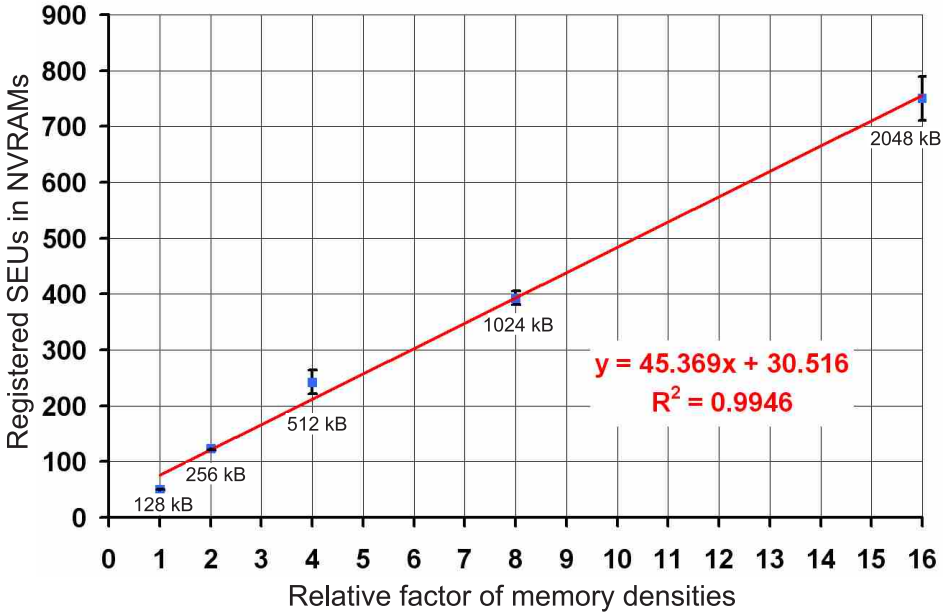

Figure 6.6: *Comparison of the SEUs generates in NVRAMs with memory densities.*

compared to determine the gradient of increasing errors with respect to memory capacity. The memories with the lowest sensitivities were omitted. The results are exhibited in Figure 6.6. The relative factors of memory densities were calculated comparing to the 128 kB SRAM. One can notice a linear relationship between the number of detected SEUs and memory density. Generally, the NVRAM sensibility increases along memory capacity, notwithstanding the new memories, which are much more immune than the old ones. Some of the tested memories were disassembled to find out the reason of contrasting sensitivities. The experiment shows that different generations of chips were used to produce memories with high and low cross-sections. The SRAMs applied for examined NVRAMs are included in Table 6.1. High-sensitivity 512 kB NVRAM bq4015 uses Samsung memories K6T4008C1B, while Renesas chips R1LP0408CSB were exploited to manufacture more immune ones. Moreover, the high-capacity NVRAMs, i.e. bq4016, bq4017 are built with an application of two or four chips (K6T4008C1B or R1LP0408CSB). Therefore, the cross-section per memory bit should be the same for all devices bq4015–bq4017. This fact explains the linear relationship presented in Figure 6.6. The small differences in SEUs registered for the high capacity NVRAMs can be explained because of inaccurate alignment of the chip with reference to neutron source (the position of SRAMs in the NVRAM package is slightly different for bq4015 and bq4016/17).

The effect of the technology trends on the memory sensitivity

The main difference in the SEUs sensitivities of the tested NVRAMs is caused by the application of various SRAMs manufactured in distinct technologies. The vulnerability of high-capacity digital devices to soft errors increases when the transistors' dimensions are shrinking and the supply voltage is decreased [211] as described in Chapter 2.2.3. Moreover, the number of transistors and memory capacities are continuously increasing because of technology development. Therefore, the higher probability of SEUs occurrence is observed. What is more, soft errors generated by atmospheric neutrons were registered at the ground level. Consequently, an integrated circuit fabrication and the design process had to be modified to enhance the immunity to SEUs. High energy neutrons are capable of inducing soft errors indirectly because of producing elastic and inelastic recoils and provoking nuclear reaction that cause high ionization in the sensitive volumes of memory cells. On the other hand, large number of soft errors is provoked because of thermal neutron interaction $^{10}B(n,\alpha)^{7}Li$ with boron present in silicone structures, see Table 4.1. Interaction of thermal neutron with silicon does not release recoiling particles of sufficient energies to cause SEU. The thermal neutron cross-section of boron-10 isotope is very high (3838 barns). The lithium nuclei are emitted with two energies 1.014 MeV or 0.84 MeV and the kinetic energy of alpha particle is equal to 1.47 MeV. Moreover, the ionizing losses of the alpha particle in the substance are four times larger than protons' with the same speed [146]. The recoil particles have a very short range in silicon below 3 µm, however their effective ionizing region is lower than 0.5 µm. Boron is usually used as a p-type dopant and it is also added to a dielectric layer-phosphosilicate glass (PSG) in weight proportion of 2-8% to reduce its reflow temperature during circuit fabrication. The boron is composed of two isotopes: ^{10}B and ^{11}B in the 19.1% and 80.1% abundances respectively. The borophosphosilicate glass (BPSG) is placed to planarize a silicon surface in the nearest proximity of the MOS transistors therefore the generated particles can catch the sensitive regions of the circuit structure, ionize it and provoke SEU. The cross-section of Boron-11 fission is much lower than for ^{10}B therefore the substitution of boron-10 isotope with ^{11}B or another material allows to design much more immune devices. The modification of BPSG layer explains the difference in SEU sensitivities between the examined memories. The fabrication process was revised beginning with 0.25 µm technologies. The Renesas memories manufactured in 0.13 µm are much more immune than the Samsung chips produced using 0.4 µm technology.

Further experiments with memories were carried out to confirm the hypothesis. The series of irradiations with an application of an americium-beryllium source were performed. Firstly, the memories were irradiated using a bare neutron source. Then, a

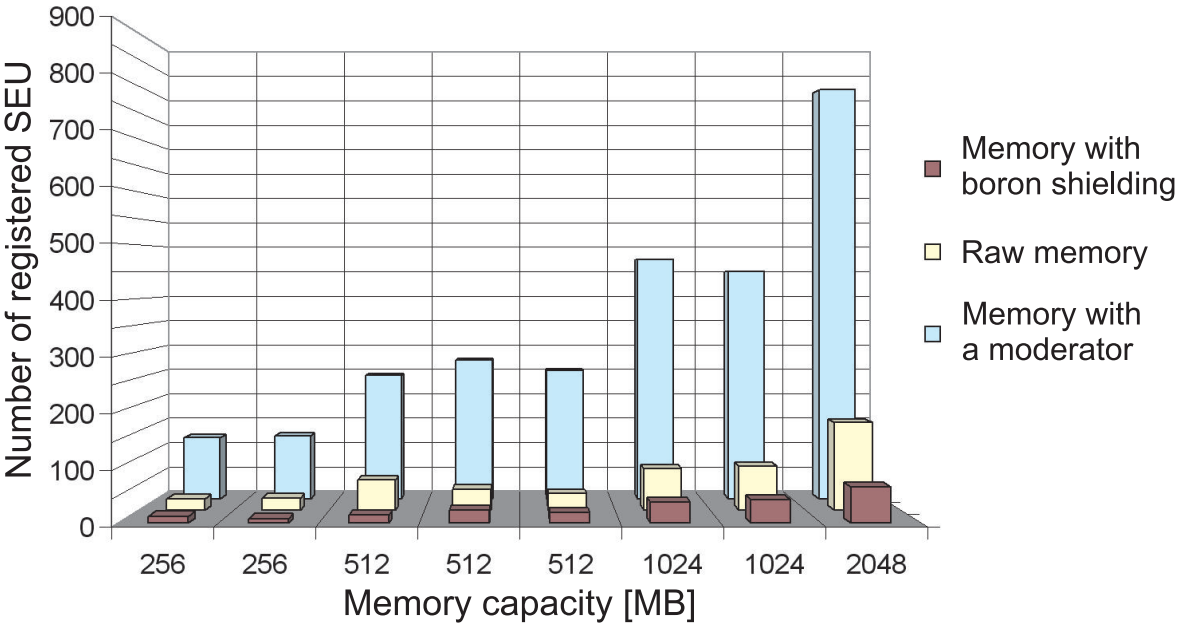

Figure 6.7: *A comparison of SEUs generated in NVRAMs irradiated from a bare, moderated and shielded by a borated polyethylene sheets, americium beryllium.*

6.5 cm water moderator was utilized to modify neutron spectrum. Finally, the devices were irradiated using a water-moderated source and an additional thermal neutron shielding material placed between the source and memory chips. A 3.2 mm thick borated polyethylene (thermal neutron attenuator) was applied as a shielding material. The most important parameters of the attenuator are presented in Appendix 9.3. The distance between the neutron source and the NVRAM chips was equal to 6.9 cm during all exposures. The selected most radiation sensitive memories with capacities between 256 and 2048 kB were used. The memories were formatted before experiment and then kept in the retention mode. The results of the investigation are presented in Figure 6.7. The number of SEUs generated in the memories is increased 5.85±1.21 times on average when the devices are irradiated from a water moderated comparing to a bare source. The application of a boron-based attenuator resulted in a significant decrease of generated errors contrary to the case of moderated neutrons. The average attenuation factor is equal to 13.06±2.44, as presented in Figure 6.7. The experiments prove that the soft errors generated in memories are caused mainly by thermal neutrons. When the mean energy of the source is lowered and the amount of thermal neutron is increased the number of bit flips increase. However, attenuation of the thermal neutron flux results in a significant reduction of SEUs created in exposed memories.

Similar experiments were carried out in Linac II accelerator. Four 512 kB NVRAMs were installed 2 m away from the electron-to-positron converter and irradiated for 12.5 hours. The first memory was installed inside a 6.5 cm polyethylene moderator.

Memory ID	NVRAMs irradiation conditions	Number of registered SEUs
#1	Bare memory	14506
#2	Memory placed inside a polyethylene moderator	74187
#3	Memory wrapped up in a cadmium foil	1539
#4	Memory wrapped up in a cadmium foil and housed in a moderator	922

Table 6.2: *NVRAMs irradiated in Linac II.*

The second and third chips were wrapped up in a 0.5 mm cadmium foil, additionally the third memory was housed in the moderator. The last memory was irradiated directly. The number of evaluated SEUs are summarised in Table 6.2. Similarly to the experiment with ^{241}AmBe, the number of SEUs generated in the memory housed in a polyethylene moderator increased 5.11 times. The application of cadmium foil caused that the number of SEUs decreased 48 times (memory #3). A reduction of 80-times in comparison to the bare chip #1 was observed when the memory #4 wrapped up in cadmium foil was placed inside the moderator. The cadmium, similarly to boron, has a huge thermal neutron cross-section and therefore effectively cuts off the particles and reduces the number of generated SEUs.

The application of an additional moderator allows to increase the number of generated SEUs in the SRAM memory and thus enhance the neutron dosimeter sensitivity. The cadmium or borated silicon can serve as a thermal neutron attenuator and can be exploited as a shielding of the readout system. The borated sponge is not toxic, contrary to the cadmium foil.

Examination of the influence of the source pattern on the memory cross-section

Previous studies described in the literature showed that the sensitivity of the DRAM chips depends on the pattern written into the memory [212]. The highest sensibility was obtained when motif complementary to the obtained immediately after power on of the DRAM device was used. Various patterns were written into NVRAM chips during irradiation tests, i.e. 0xFF, 0x00, 0x55, 0xAA, random and the power-on complementary schemes to find out the most sensitive scheme. However, contrary to DRAM memories as reported in [212], no significant difference in the SEU cross-sections were observed. A symmetrical construction of a SRAM cell and sense amplifier may explain the independence of SRAM memory sensitivity from utilized bit-pattern. The DRAM consists of an unsymmetrical matrix of capacitor-based storage cells. Supple-

mentary dummy cells, cooperating with symmetrical sense amplifiers are used during reading and writing [54]. Therefore, the small differences between storage and dummy cells, imperceptible under normal operation, can explain the highest sensitivity to the complementary power-on pattern of the DRAM.

The influence of gamma radiation on NVRAM

Two 512 kB formatted NVRAM batches were subjected to gamma radiation. A strong ^{60}Co gamma source with average energy equal to 1.3 MeV was applied. The memory chips were irradiated up to 1.1 kGy in 20 days. After the exposure the memories were evaluated. This high gamma radiation seems to have produced practically no SEU [15-A]. Therefore, gamma radiation has a negligible chance of triggering SEU in the SRAM chip. However, the radiation can be detrimental to the functioning of the memory when it exceeds the safe level because of the TID effect. Therefore, the lifetime of SRAM must be estimated.

6.1.3 SRAM devices

The application of NVRAMs was very helpful in the initial phase of research [19-A]. However, the desired neutron detector is going to measure fluence in real time. Moreover, the utilization of the NVRAMs has imposed a few restrictions, e.g. used SRAM devices, a fixed power supply voltage. On-line radiation measurement can prove that the amount of generated SEUs can be correlated with neutron fluence and supply information about the linearity of the neutron sensor.

Real time exposure of SRAM chips

A few experiments using ^{241}AmBe and different memories were carried out. The relationship between accumulated SEUs induced in 128 kB Samsung memory K6T1008C2E within 24 hours exposure is presented in Figure 6.8. The parameters of the Samsung memory are collected in Table 6.1.3. The americium-beryllium source was directly installed on the memory chip package. The memory was irradiated with the standard ^{241}AmBe spectrum. A 5 V power supply was connected to the SRAM. The distance between the memory and the source was equal to 5 mm, thus the neutron fluence was very high in the range of $6{\times}10^{10}$ n·cm^{-2}. The measured SEUs during time passing were represented with a linear regression, see Figure 6.8. The neutron source emits a constant flux of neutrons with time therefore the accumulated number of SEU should increase linearly. The R-square value for the calculated regression is very close to 1 as pointed out in Figure 6.8. The second exposure was also performed with americium-beryllium within 47 hours. The 512 kB SRAM memory K6T4008C1B manufactured by

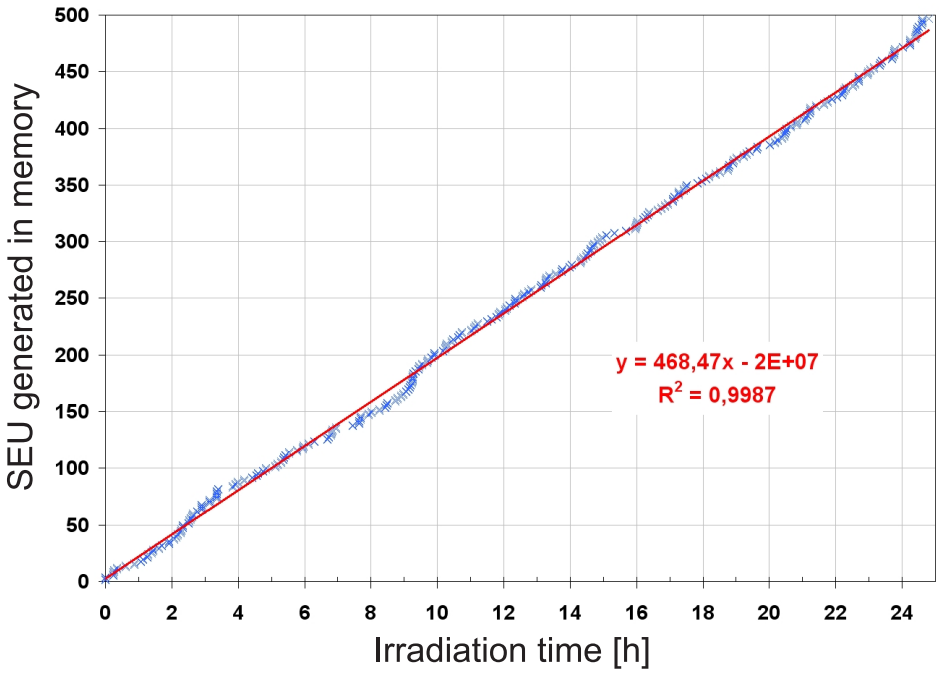

Figure 6.8: *SEUs generated in 128 kB Samsung memory irradiated with $^{241}AmBe$. The total neutron fluence was equal to 6×10^{10} $n\cdot cm^{-2}$.*

Samsung was subjected to a light water moderated neutron source with E_{AV}=4.1 MeV. The distance between device under test (DUT) and the source was equal to 6.9 cm. The memory was supplied from 5 V. The accumulated soft errors generated during exposure and calculated accumulated neutron fluence are depicted in Figure 6.9. The number of SEUs registered during 24 hours was almost the same as for the previous irradiation, however the total neutron fluence was two orders of magnitude lower, see Figure 6.8 and 6.9. The applied 512 kB memory has a higher sensitivity than 128 kB SRAM. The examined memories are more susceptible to a water moderated source with lower energy neutrons. Similarly to the previous experiment, the linear regression was fitted to the registered characteristics. The R-square factor is slightly better than the previous one because a larger number of errors were registered.

The examination with ^{241}AmBe(α,n) source reveals a good linear relationship between the number of generated SEUs and the neutron fluence in real time. The radiation monitoring system RadMon composed of radiation-tolerant readout and 128 kB SRAM-based detector was installed in the Linac II tunnel [15-A, 20-A]. The device was mounted 20 cm from the wall and approximately 18 m from the main source of gamma and neutron radiation – the e^-/e^+ converter (see Chapter 6.1.1). The temperature of the memory chip was constant during the experiment and equal to 37±1 °C. The measured accumulated number of SEUs is illustrated in Figure 6.10 [15-A]. The shape of the characteristics is not any more linear, as opposed to the curve obtained with ^{241}AmBe. The radiation produced in Linac II tunnel is highly variable in time.

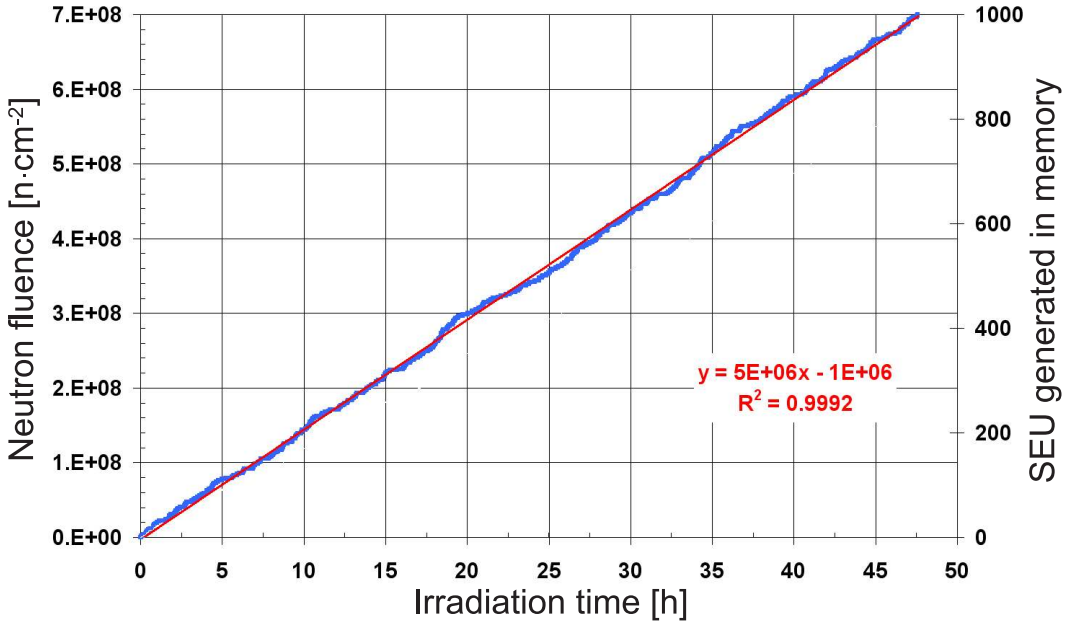

Figure 6.9: *Accumulated neutron fluence and number of SEUs generated in the 512 kB memory irradiated from $^{241}AmBe$.*

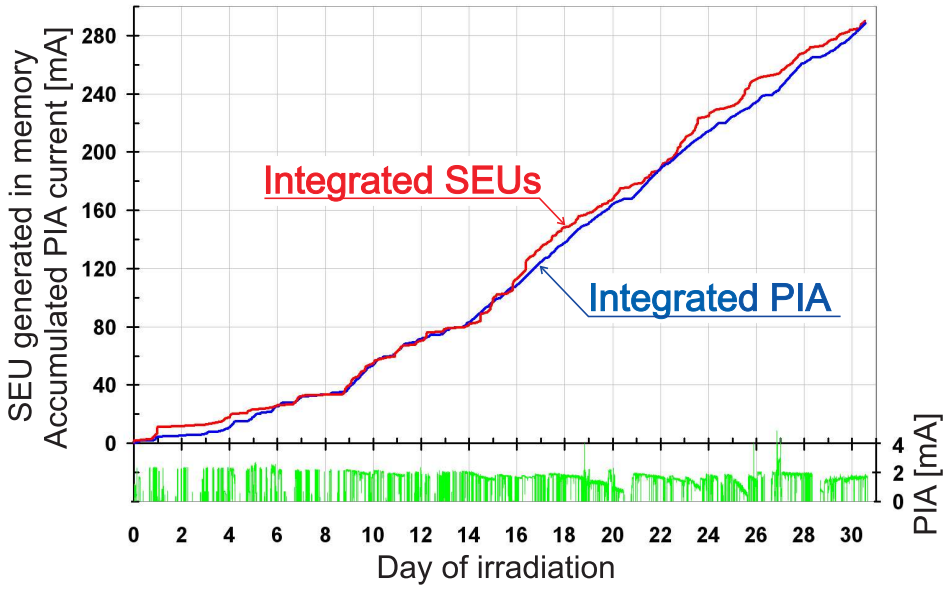

Figure 6.10: *The accumulated PIA current and SEUs generated in a 128 kB memory subjected to neutron and gamma radiation in Linac II tunnel.*

No radiation dosimetry system allowing to measure neutron fluence or gamma radiation produced during operation of Linac II is installed, therefore the results obtained from the RadMon cannot be compared. However, the PIA current can be measured in the PIA-storage ring while electrons are accelerated and positrons are formed in Linac II [213]. The value of the current allows to distinguish between electrons and positrons. The highest radiation is observed when positrons are produced and the e^-/e^+ converter is operating. Therefore, to verify the SRAM-based detector response in the real environment of the linear accelerator the rescaled accumulated PIA current, accompanying the registered SEUs, is added (Figure 6.10). The original value of PIA current is presented in the form of green spikes below the x-axis . The shape of the integrated PIA curve is very close to the integrated SEUs, the standard deviation calculated for the measurement is equal to 6.76. The PIA characteristics is sometimes lower than the registered error curve. The difference may be caused by a temporary increase of generated neutrons that are not originated in the converter, e.g. beam loss in cavities. In such a case the measured PIA will not reflect the real neutron fluence in the tunnel.

Neutron sensitivity tests of commercial SRAM chips

The experiments carried out with ^{241}AmBe(α,n) source and in Linac II tunnel reveal a linear relationship between soft errors generated in a SRAM and neutron fluence. The SRAM-based neutron sensor should be characterised by good sensitivity to allow measuring low neutron fluence in the accelerator tunnel with satisfactory accuracy. Therefore, a number of experiments was completed to measure the commercial-off-the-shelf (COTS) asynchronous SRAMs neutron vulnerability and to quantify the sensitivity factor defined similarly to NVRAM devices. Further exposures with ^{241}AmBe(α,n) neutron source were performed. A 6.5 cm water moderator was applied to enhance the number of errors generated in memories and therefore improve the accuracy of SRAM assessment. A large number of different memories, manufactured in various technologies, were examined. A universal socket was added to the reader to allow for a fast and convenient exchange of the tested memory module. Exemplary SRAM modules, tested during the irradiation, are gathered in Figure 6.11. All the memories were supplied from 3.3 V during irradiation. The most important SRAM parameters, calculated SEU cross-sections and sensitivity factors are presented in Table 6.1.3. The determined SEU cross-sections and SFs are depicted in Figure 6.12 to facilitate the analysis of the results. Generally, the devices manufactured in older technologies disclose the highest SEU cross-sections. The modern, high-capacity memories are at least two orders of magnitude more resistant. Moreover, no SEU was registered in the 2 MB

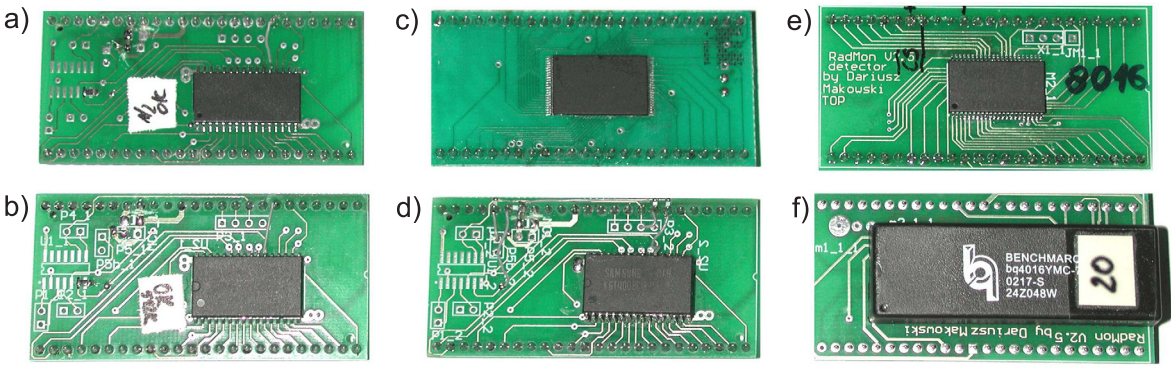

Figure 6.11: *Exemplary SRAM modules - potential candidates for a memory-based detector.*

Memory reference	Memory capacity	Manufacturer	Supply voltage	Feature size	Cross-section [$cm^2 \cdot bit^{-1}$]	Sensitivity factor
K6T1008C2E-DB55	128 kB	Samsung	5 V	—	2.32×10^{-13}	2.42×10^{-7}
TC554001AF-70L	512 kB	Toshiba	2.7-5.5 V	0.4 µm	3.19×10^{-14}	1.33×10^{-7}
IS61LV25616AL-10T	512 kB	ISSI	3.3 V	0.18 µm	2.81×10^{-14}	1.33×10^{-7}
CY62148BLL-70SI	512 kB	Cypress	4.5-5.5 V	0.25 µm	8.85×10^{-14}	3.71×10^{-7}
M5M5408BFP-70H	512 kB	Renesas	5 V	0.25 µm	1.42×10^{-13}	5.94×10^{-7}
K6T4008C1B-VB55	512 kB	Samsung	4.5-5.5 V	0.4 µm	3.18×10^{-13}	1.34×10^{-6}
K6T4008C1B-GB70	512 kB	Samsung	5 V	0.4 µm	2.94×10^{-13}	1.23×10^{-6}
M68AF511-AM70MC6	512 kB	ST	4.5-5.5 V	0.18 µm	9.03×10^{-15}	3.79×10^{-8}
IDT72V2111-L15PF	576 kB	IDT	3.3 V	0.5 µm	no SEU registered	0
K6X8008T2B-TF70	1 MB	Samsung	2.7-3.6 V	0.13 µm	4.60×10^{-15}	3.86×10^{-8}
K6X8016C3B-TF55	1 MB	Samsung	4.5-5.5 V	0.13 µm	1.16×10^{-15}	9.71×10^{-9}
R1LV1616HSA-4LI	2 MB	Renesas	2.7-3.0 V	0.13 µm	no SEU registered	0

Table 6.3: *Characteristics of the tested SRAMs with calculated cross-sections and sensitivity factors.*

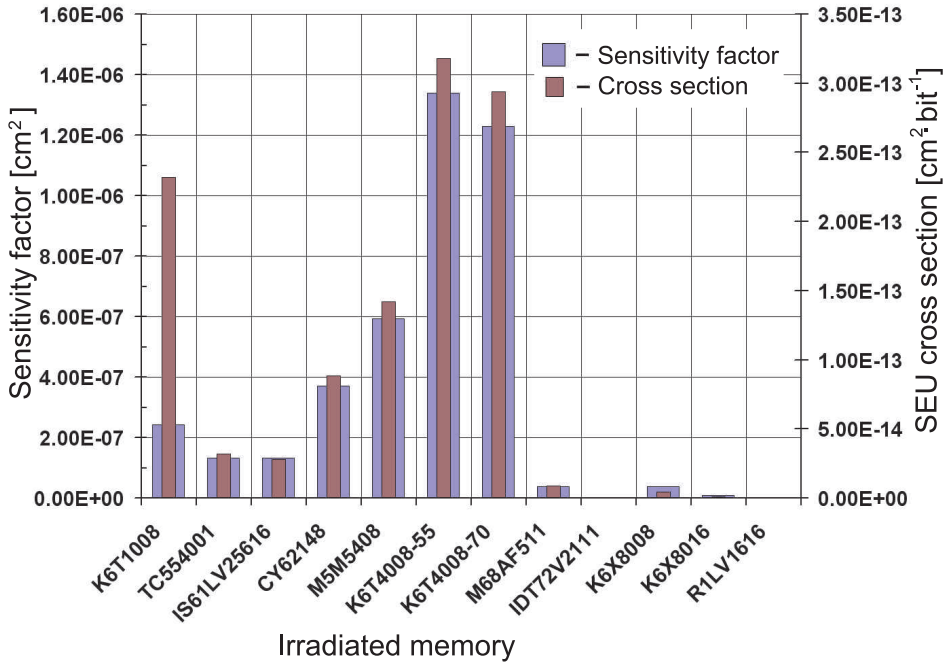

Figure 6.12: *SEU cross-sections and sensitivity factors for SRAM chips irradiated with $^{241}AmBe$.*

Renesas memory within 48 hours exposure. Further study of datasheets and technical reports showed that ECC circuit are being implemented in Renesas chips. The memory was continuously read during the exposure therefore ECC system was able to correct every single error and did not allow for their accumulation. Despite the high cross-section of the K6T1008C2E Samsung memory, the device is not suitable for the radiation detector because of the small capacity and thus poor SF. The best results were obtained for 512 kB Samsung SRAMs manufactured in 0.4 µm technology, see Figure 6.12. The memory has a low retention voltage (2 V), hence its sensitivity can be further enhanced, see Chapter 6.1.4.

A dedicated reader was designed and built to examine the first input first output (FIFO) memory (512 k x9 bits) fabricated by IDT, see Chapter 7.1.2. The memory demonstrated no sensitivity to the influence of neutrons. Writing and reading data from the FIFO is very fast and convenient, thus a radiation sensitive FIFO memory could be an ideal solution for a SRAM-based neutron sensor.

High-capacity, low supply voltage memories have weak sensitivity factor. Therefore, a 512 kB K6T4008C1B-GB70 memory produced by Samsung was finally chosen as a neutron fluence detector. Four 512 kB memories were stacked to create 2 MB structure. The memories were connected to the reader using 8-bit data bus. The bus was extended to 32 bits in the next generation of the readout system to accelerate the evaluation time, see Chapter 7.1.

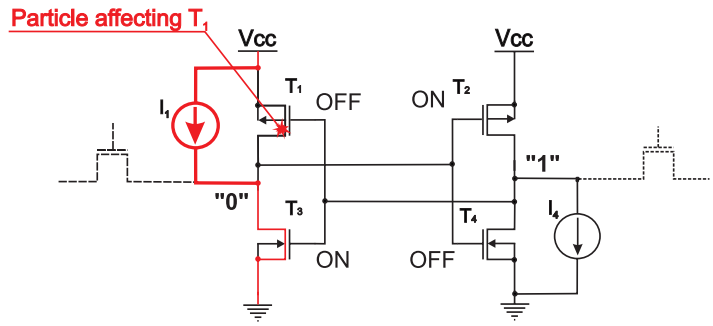

Figure 6.13: The schematic diagram of a 6T SRAM cell used to simulate vulnerability to SEU when the supply voltage is decreased.

6.1.4 The methods to increase the sensitivity of the neutron sensor

The sensitivity factor of the Samsung memory was enhanced four times when the stacked structure was built. However, the sensibility was still not good enough to measure the neutron fluence in the VUV-FEL tunnel. An application of higher-capacity SRAMs was not possible therefore other methods allowing to increase the sensitivity were taken into consideration. Firstly, a decrease of the memory supply voltage can help to sensitize the sensor. Secondly, the experiments carried out with an application of water or polyethylene moderators exhibited that the sensitivity can also be improved.

A modification of the memory supply voltage

The vulnerability of integrated circuits to SEUs is increased with the fabrication technology development. The dimensions of the transistors in the CMOS technologies are shrinking and therefore the critical charge necessary to provoke SEU is also reduced. Therefore, a lower current is required to be delivered by an incident particle to change the state of the storage cell in case of memory. The bit flip of a standard 6T SRAM cell was simulated with an application of SPICE. The current induced by ionizing particle was imitated using a 5 ns long transient pulse of current. The simulation was carried out for transistors manufactured in 0.35 µm technology. During a stable operation of the SRAM cell only two deactivated transistors are susceptible to soft errors and can be turned on. The schematic diagram of the memory cell with two current sources is shown in Figure 6.13. The simulation showed that the critical charge is decreased when the supply voltage is lowered. Therefore, the threshold of the transient current also changes and the probability of the memory state change is increased (assuming that the neutron fluence is constant). The results are presented in Figure 6.14. A series of irradiations with a water moderated americium-beryllium was carried out to investigate the possibility of sensitivity enhancement. The results for Samsung K6T4008C1B

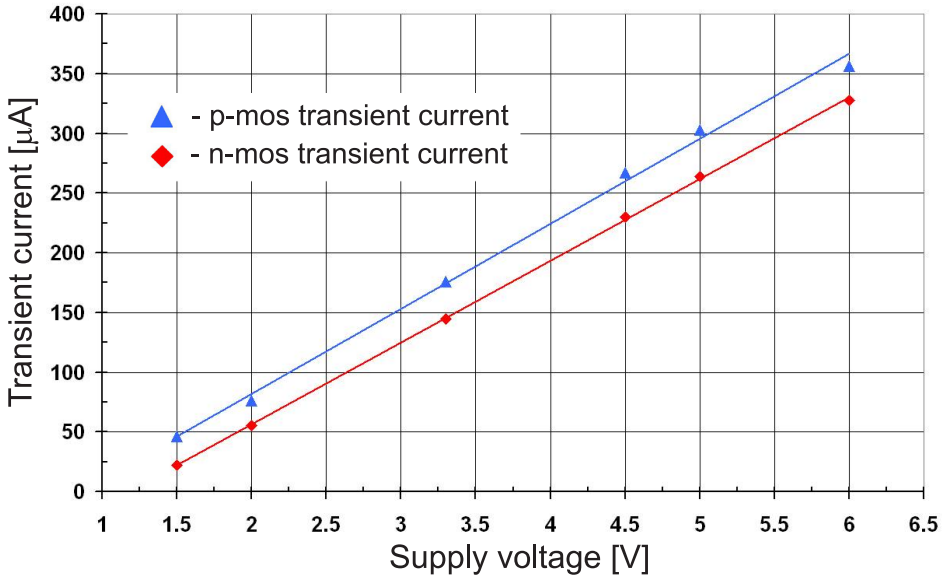

Figure 6.14: *The trend of the threshold of transient current depending on the SRAM supply voltage.*

and Toshiba TC55001AF SRAMs are presented in Figure 6.15. Both memories are dedicated to be supplied from 5 V. The memories operated stable when the voltage was higher than 2.7 V for the Samsung and 2.2 V for Toshiba. The experiment proved that the SEUs sensitivity of the Samsung SRAM chip can be enhanced 8 times and 20 times for the Toshiba chip when the voltage is reduced to 3.0 V. On the other hand, the memory supply voltage must be high enough to guarantee long-term reliable operation. Despite the fact, that the Toshiba memory was able to operate when supplied from 2.2 V, the number of SEUs generated in the Samsung memory supplied from 2.7 V was higher than in Toshiba chip.

An application of an external moderator

Cylindrical moderators made of polyethylene with different diameters (ϕ 7, 10, 13, 18 cm) were used to investigate the ability to enhance the sensitivity of a SRAM-based neutron detector. Two tests were initially carried out with a water moderated ^{241}AmBe and then the NVRAMs placed in the moderators were irradiated in Linac II. The exemplary moderators used during the examination are presented in Figure 6.16. The best results were obtained for the moderator with 9 cm radius. The ideal shape of the device should be spherical to assure a uniform slowing down of neutron around a point neutron dosimeter. Semi-spherical moderator presented in Figure 6.16 was applied instead of the ideal spherical structure. The SRAM-based sensor is not a point detector therefore the deformation of the moderator shape has a negligible influence on the response of the whole dosimeter. The main advantage of the presented solution is easier fabrication and therefore lower production costs. However, it is should be

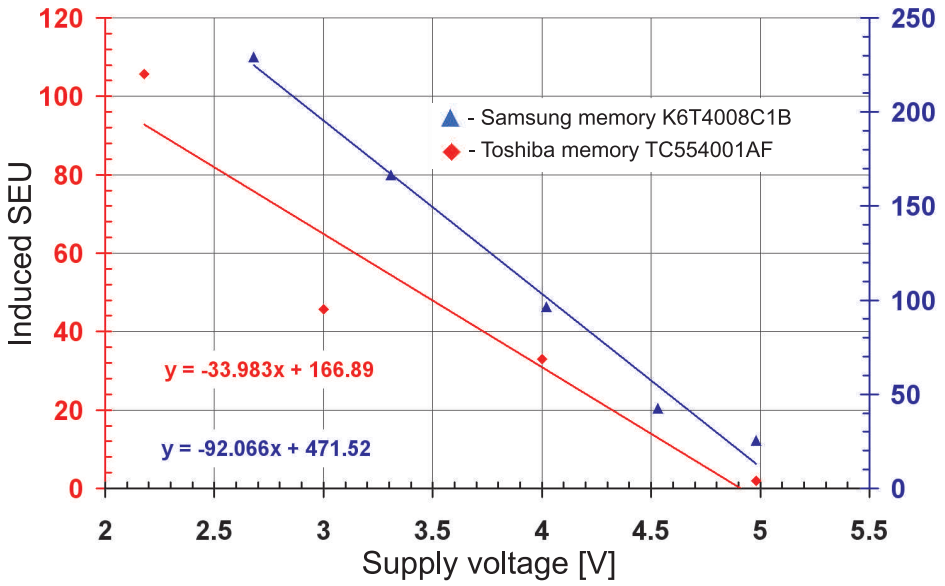

Figure 6.15: *The relative sensitivity enhancement of the SRAM device for different supply voltages.*

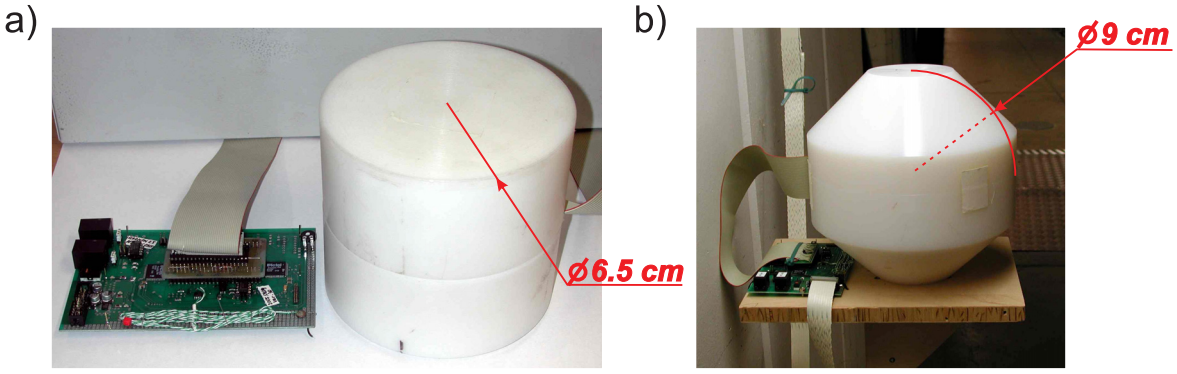

Figure 6.16: *Polyethylene moderators: a) 6.5 cm cylindrical and b) 9 cm semi-spherical moderators.*

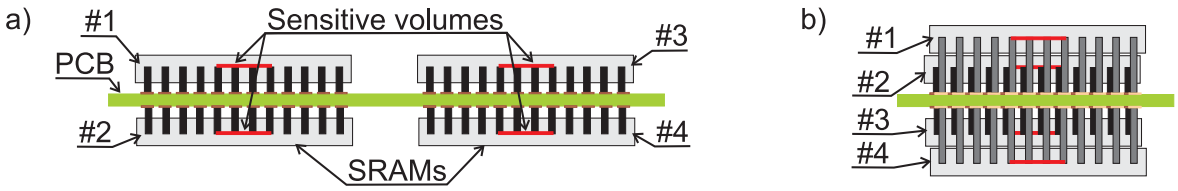

Figure 6.17: *The SRAM-based sensors: a) the flat version and b) the sandwich structure.*

emphasized that the sensitive volume (SV) of the SRAM chip must be small. The proposed detector consists of four SRAM devices (total capacity 2 MB) thus the SV is four times larger compared to a single chip. During the experiments two types of the 2 MB memory modules were used, flat and sandwich versions, see Figure 6.17. The sandwich structure imitates a point detector better because of more concentrated SVs and therefore it is more suitable for the detector.

The sensitivity tests in VUV-FEL tunnel

Both methods were applied to enhance the sensitivity of the SRAM-based neutron detector. A RadMon equipped with a 2 MB stacked flat-sensor based on Samsung memories supplied from 3.3 V has been installed in the VUV-FEL tunnel for three months. The K6T4008C1B memories are able to operate with voltages below 3 V (the retention voltage is equal to 2 V), however the voltage was increased to 3.3 V to assure a long-term reliable functionality. The sensor was housed in the 9 cm semi-spherical polyethylene moderator. Two additional RadMon systems were installed in the VUV-FEL tunnel to allow comparing the sensitivities of the memories. The first was equipped with the same 2 MB memory supplied from 3.3 V and the second cooperated with a bare 1 MB stacked SRAM with 5 V supply voltage. The registered number of SEUs generated during 28 days irradiation in VUV-FEL tunnel is depicted in Figure 6.18. The number of SEUs registered in the 2 MB memory (3.3 V) is 5.6 times higher than the amount generated in the bare chip supplied from 5 V (the memories have different capacities therefore the number of SEUs in bare chip was doubled to calculate the ratio). The application of 9 cm moderator enabled to enhance the sensitivity by 3.9 times. However, the total sensitivity to soft errors was increased 22 times when both methods were utilized [18-A]. The memories with reduced supply voltages operated correctly more than 6 months. The accelerator is deactivated for a few hours every week. The flat regions on the characteristics depicted in Figure 6.18 correspond to the days when the accelerator was stopped and no neutrons were produced.

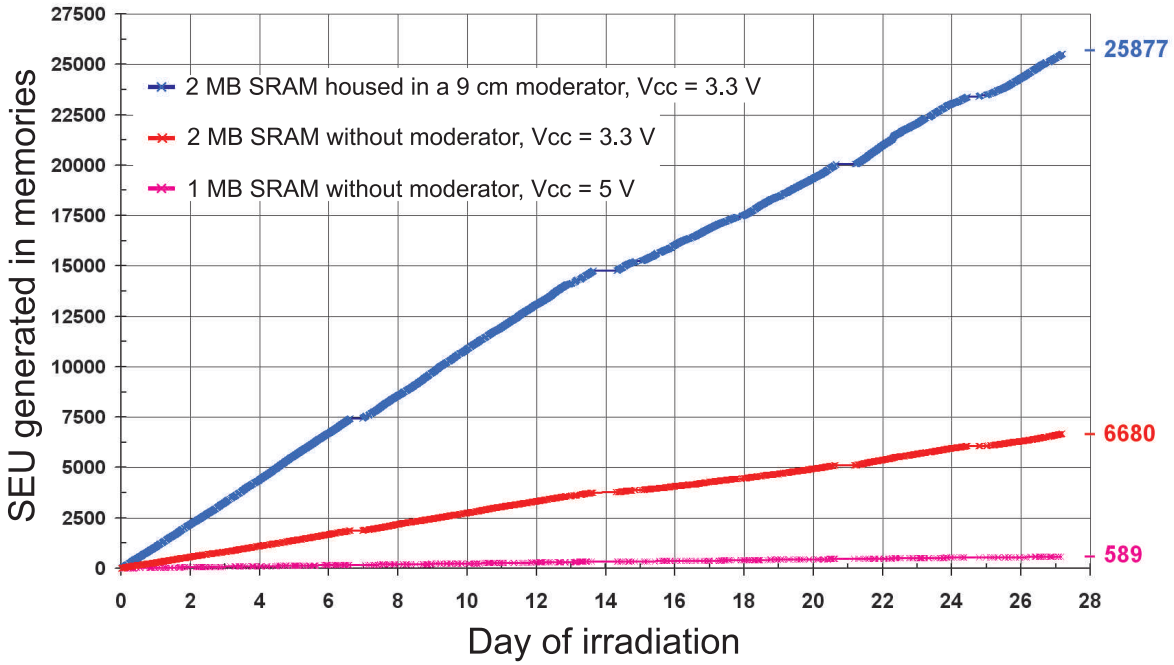

Figure 6.18: *A comparison of 1 and 2 MB memory modules irradiated with and without moderators in VUV-FEL (a total number of detected soft errors is pointed out on the right side).*

6.2 The gamma radiation detector

The application of SRAM device as a gamma detector cannot supply good enough sensitivity, therefore a better sensor must be applied. A RadFET dosimeter can be easily combined with a digital readout system and is able to supply dose and dose rate measurement in real time. RadFETs are produced with a different silicon oxide thicknesses, thus the required sensitivity can be adjusted. The parameters of exemplary RadFET dosimeters manufactured by NMRC company are presented in Table 6.4 whereas the sensors are illustrated in Figure 6.19. The sensitivity was measured at 15 Gy(H_2O) using a constant 10 µA current. The RadFETs were irradiated in two modes, when the electric field across the oxide was equal to 0 and 0.125 MV·m^{-1}. A 5 V bias voltage V_{bias} between a RadFET gate and drain-source may be applied to obtain the required electric field (0.125 MV·m^{-1}).

Each RadFET includes two types of PMOS dosimeters with different W/L values, i.e. 300/50 and 868/11. The dosimeters have the same sensitivity, however the initial threshold voltages are different. The device has small dimensions, it is lightweight and has a low power consumption [179,180,214]. The RadMon system was equipped with a dedicated analogue channel to connect a single RadFET dosimeter. The readout system is described in Chapter 7.1.3. RadFETs have significant initial threshold voltages before exposure to radiation. Therefore, a boron implanted version was designed to reduce the initial threshold voltage and increase its sensitivity, i.e. 4 kÅ implanted.

RadFET type	Oxide thickness	Sensitivity V_{bias}=5 V	Sensitivity V_{bias}=0 V	Extrapolated V_{th}	Temp. coefficient
1 kÅ	100 nm	9 mV/Gy	0.14 mV/Gy	-2.15±0.1 V	2.5 mV/°C
4 kÅ	400 nm	25 mV/Gy	18 mV/Gy	-6.9±0.3 V	6.4 mV/°C
4 kÅ implanted	400 nm	133 mV/Gy	46.3 mV/Gy	-1.0±0.4 V	2.5 mV/°C
10 kÅ	1 µm	240 mV/Gy	80 mV/Gy	-17.2±0.4 V	15 mV/°C

Table 6.4: *The parameters of NMRC RadFET dosimeters (the parameters refers to a 300/50 type).*

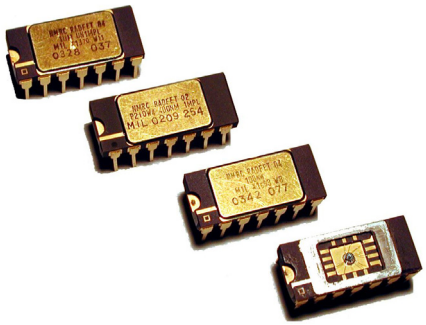

Figure 6.19: *The RadFETs family manufactured by NMRC, from left side: 10 kÅ, 4 kÅ, 1 kÅ, 1 kÅ.*

The RadFET is subjected to radiation in the sense mode (SM) when the drain and source electrodes are grounded, see Figure 7.10. However, the device must be switched into reader circuit (RC) before readout as presented in Figure 7.10. The source electrode is reconnected from ground to the current source. A 20 s delay after the reconnection is recommended to assure stabilisation of switching traps created inside Si-SiO_2 interface and silicon oxide [179, 214]. A high sensitivity of the RadFET is not always perceived as an advantage, particularly in high dose fields, because the maximum detectable dose is reduced when high sensitivity dosimeter is used. The maximum measured dose is limited because of readout system's and RadFET's linearity. The irradiation is a destructive process, therefore RadFET must be replaced after a long-term irradiation when the radiation-increased threshold voltage is out of the readout range or a linear region. Concluding, the lifetime and the maximum detectable dose of the most sensitive 10 kÅ RadFET is lower than the 1 kÅ one.

The research carried out allows to choose the 4 kÅ implanted RadFET as a gamma dosimeter because of a good sensitivity, low initial threshold voltage and relatively low fading effect. A 4 kÅ implanted RadFET connected to RadMon system was irradiated from ^{137}Cs gamma source. The bias voltage V_{bias} during the exposure was set to 5 V. The data describing the source are presented in Appendix 9.3. The distance between gamma source and RadFET dosimeter was equal to 20 cm. The accumulated gamma

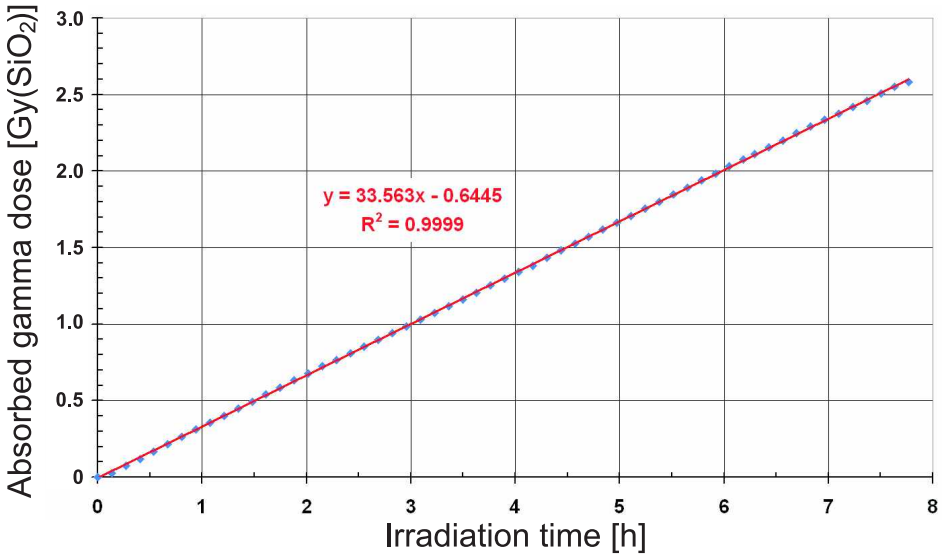

Figure 6.20: *An integrated gamma dose measured using 4 kÅ implanted RadFET dosimeter.*

dose registered in real time within a 7.5 hours irradiation is presented in Figure 6.20. The experiment was carried out at room temperature. The ^{137}Cs source supplies a constant flux of gamma photons. The calculated R-square coefficient for first order linear regression for the presented results is very close to 1. The substantial fading effect of the RadFET that is presented in Figure 6.21, was observed after the exposure. The fading is caused because of partial annealing of the MOS transistor [176, 177, 179, 180]. The fading could have a significant influence on the measured dose and can disrupt the correct interpretation of measured dose. However, further irradiation with no electric field in the RadFET oxide shows that the fading was significantly reduced and was estimated to be in range of 1-2 % within five days. However, the effect must be corrected on-line before the data are gathered in the database.

The RadFET sensor is also sensitive to neutron radiation, therefore cannot be used in the high intensity neutron dominated irradiation fields [163, 181]. However, the amount of gamma radiation produced in VUV-FEL tunnel is a few orders of magnitude higher than neutron fluence. Therefore, the error caused by neutron influence is rather low. Moreover, production of both types of radiations is partly correlated, thus the appropriate correction coefficient can be calculated. The output threshold voltage of the RadFET is sensitive to temperature drift [180]. A suitable correction circuit has been applied to minimise the influence of temperature to measure the gamma dose, see Chapter 7.1.3.

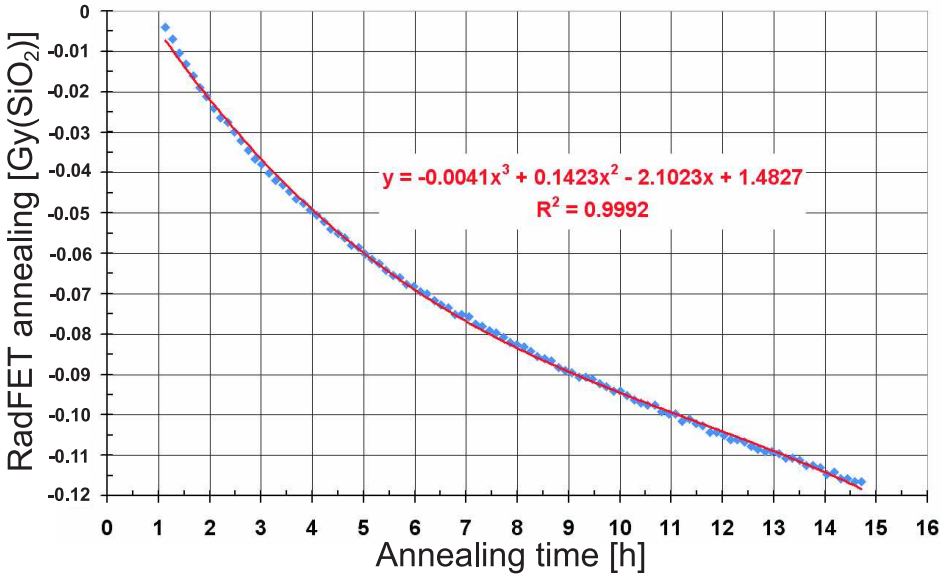

Figure 6.21: *An annealing effect of 4 kÅ implanted RadFET sensor irradiated from ^{137}Cs gamma source.*

6.3 Conclusions

The experiments carried out with NVRAM and SRAM devices that were irradiated with americium-beryllium and in linear accelerator's tunnels allow to adapt the SRAM chip as a neutron fluence detector. The sensitivity of the commercial memories to neutron-provoked SEUs was not sufficient to measure radiation in the VUV-FEL. The sensitivity of the high-capacity memories manufactured in modern technologies should be dramatically enhanced, whereas the feature size and supply voltage are decreased. The number of generated soft errors decreased significantly contrary to expectations. The cross-section calculated for the memories manufactured in 0.13 µm technology was two orders of magnitude lower than the one computed for older chips. Boron 10–based BPSG layer present in SRAM devices plays a crucial role in the formation of SEUs. The removal of the conversion layer resulted in the reduction of neutron detector sensitivity. Thus, high-capacity modern memories with low supply voltages are not good candidates for a neutron fluence sensor. Moreover, the implemented ECC circuit in one of the tested memories tellingly prevent to induce SEU.

The 512 kB Samsung memory manufactured in 0.4 µm technology was chosen as a neutron dosimeter. The efficient methods were elaborated to improve its sensitivity to SEU. The reduction of the memory supply voltage from 5 V to 3.3 V resulted in 5.6 time multiplication of its sensibility. A safe voltage margin has been kept to guarantee safe operation. Further design of a suitable moderator allows also to increase memory sensitivity by 3.9 times. Finally, the sensitive volume of the memory-based sensor was enlarged four times by application of four chips. Therefore, the total sensitivity of the

neutron dosimeter was enhanced almost two orders of magnitude. Cadmium foil or a borated sponge can be applied as a shielding material because of the high thermal neutron cross-section.

The NVRAM chips were very useful in the different stages of the project. The memories allow to apply and examine quickly new ideas and technologies. Even if the memories were not calibrated, the memories were used for comparative measurement, e.g. the gain of sensitivity for different moderator diameters were checked employing bq4015 chips. However, the relative response of the chips were determined with ^{241}AmBe.

The reduction of the supply current of the modern low-power asynchronous memories prevented to apply the devices as a gamma sensor. The measurement of a small current in accelerator's tunnel is difficult and thus the detector cannot supply reliable results. Alternatively, a dedicated ionizing dosimeter–RadFET has been applied. During the application of the detector a few problems were encountered. Firstly, the initial threshold voltage of the detector must be taken into consideration before readout is constructed. Some of the detectors have high initial voltages around 20 V. Moreover, RadFET is temperature sensitive, thus a suitable correcting circuit must be applied. The temperature coefficients of various RadFET types are different. The RadFETs vulnerability to neutrons cannot pose a problem in case of VUV-FEL, whereas the amount of gamma radiation produced in the tunnel is a few orders of magnitude higher than the neutrons fluence.

Chapter 7

RadMon–the radiation-tolerant radiation monitoring system

RadFET and the SRAM-based neutron fluence sensors cooperate with a dedicated radiation tolerant readout. The system, called RadMon, is installed in the VUV-FEL tunnel. Measured data are sent from RadMon using the EIA 232 interface. The EIA 232 is reliable enough to transfer data from the readout at a distance longer than 60 m with a 9600 baudrate. The designed system allows to gauge radiation at various spots inside an accelerator tunnel. A modular construction and the application of Ethernet medium for data transmission allow to extend the system easily. Signals from RadMons are connected to a EIA232–to–Ethernet AXEL AX4020 bridge and sent to the main computer. A distributed four-channel system is presented in Figure 7.1. The PC is responsible for generation of control signals for all devices, collecting data, requesting diagnostic information and handling the watch-dog operation.

The SRAM-based sensor should be scanned continuously after an initialisation process. However, the short interruptions of memory checking are permitted because the error of measured neutron fluence caused by a system restart is relatively insignificant. The average period between two SEUs induced in a 2 MB memory housed in a 9 cm

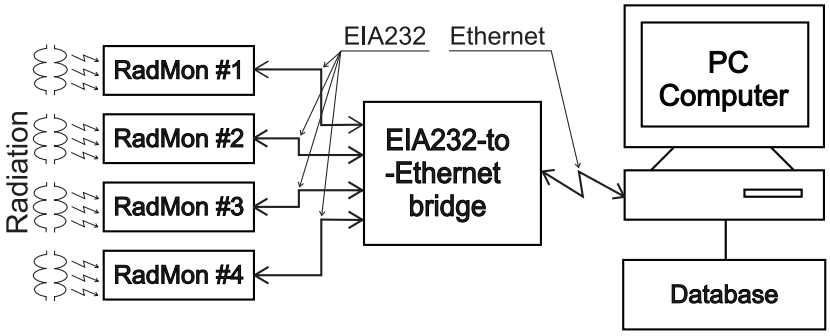

Figure 7.1: *The block diagram of a four-channel distributed radiation monitoring system.*

moderator in the VUV-FEL accelerator was equal to 90 s, see Figure 6.18. Scanning cycle time is also not critical in such a case. On the one hand, when the device is used to trigger an interlock system, the scanning cycle and restart time must be shorter than 150 ms and restarts of the system should be minimized [206].

A few different versions of RadMon readout were designed and examined, while SRAM and NVRAM devices were being tested [2-A], [20-A – 27-A]. RadMon systems were constructed using relatively cost-effective commercial-off-the-shelf (COTS) components. The characteristics of designed systems and the advisability of using them in the harsh radiation fields are presented in Section 7.1. Conclusions are drawn to summarise performed research.

7.1 A review of radiation-tolerant readout systems

A radiation-tolerant device had to be constructed to allow operating a SRAM device and therefore gauging the number of triggered SEUs in real time. Initially, the memory installed in Linac II was connected to the reader placed in a non–radioactive field using a long cable. However, a cross-talk between cables prevented from obtaining reliable results. Therefore, the readout system was moved into the Linac II tunnel. Radiation present in a linear accelerator poses another problem. SEUs in the reader electronics may be generated and the entire system could be jeopardized. Various systems were designed to counteract radiation-generated soft-errors using different methods. All devices were constructed employing COTS elements. The negative influence of gamma radiation and neutron displacement damage can be reduced by the application of suitable shielding [6-A], see Chapter 3.2.

7.1.1 The application of redundancy to design radiation-tolerant systems

A modular redundancy was used to enable a faultless operation of the RadMon in the accelerator tunnel. Although radiation is measured on-line and the memory is continuously read, short interruptions of the read-out system are acceptable [20-A]. Hence, a DMR was able to protect the system against SEUs. The advantage of DMR is the low excess of hardware in comparison with other hardening methods, e.g. TMR. The schematic diagram of the designed system is presented in Figure 7.2. Two identical microcontrollers generates control signals, however only one of them handles the SRAM device. Signals generated by microcontrollers are connected to a data comparator. An interrupt is generated when the comparator detects an inconsistency. Then, microcontrollers send information to a PC and the system is restarted. An additional watch-dog

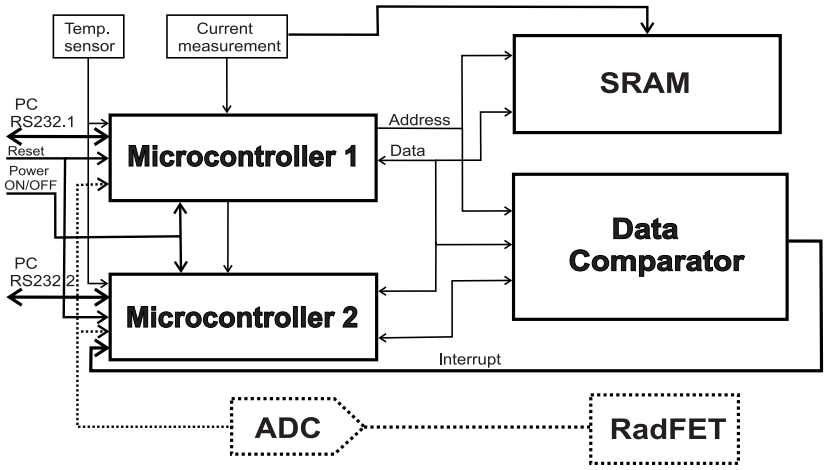

Figure 7.2: *A block diagram of the RadMon device.*

was applied to assure a reliable operation of the system. The PC generates a hard-reset signal and writes a new pattern into the SRAM device in case of a general RadMon's failure that is not corrected by DMR. The RadMon device cooperates with a master PC computer, therefore the device must be able to perform commands delivered from the PC. During the normal operation, the system periodically sends heartbeat frames to the PC. A hard reset is generated when the heartbeat frame is not delivered to the PC at the appointed time. The first prototype of RadMon (version 1.0) was built with an application of two ATMEL's 8051–family microcontrollers and a TTL–based control logic [20-A], see Figure 7.3. The system was able to supervise a maximum of 128 kB memory supplied from 5 V. The old TTL technology was chosen intentionally, because it is much more resistant to radiation than modern circuits. Highly advanced, low–voltage devices with reduced feature sizes are more susceptible to SEE. The doses of radiation generated in Linac II were not known, therefore the old technology was chosen to investigate the influence of radiation on both: the readout system and the sensing memory [20-A] . Microcontrollers manufactured by Microchip were used to design the second prototype of RadMon [2-A]. The version 2.0 is illustrated in Figure 7.3. The system, supplied from 3.3 V, is able to handle up to 128 MB SRAM chip employed as a neutron fluence detector. The microcontrollers operate synchronously executing the same program and therefore supply identical control signals to peripheral devices. However, the scanned memory and auxiliary devices are controlled only from the master device (microcontroller 1), see Figure 7.2. A digital comparator based on FPGAs produced by Actel was utilised as a voter. The digital voter is radiation sensitive, thus the system will be restarted when neutrons generate SEU or SET in the main logic. However, the configuration of the employed FPGA is stored in a FLASH memory that is much more immune to SEU than SRAM. During the RadMon operation, additional parameters are measured: supply current and temperature of the memory. The mea-

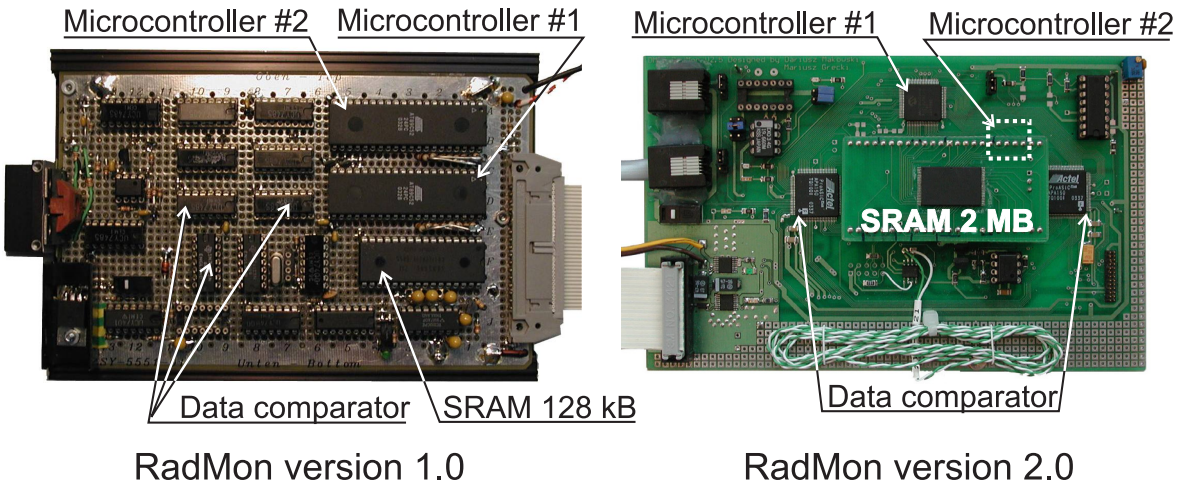

Figure 7.3: *The photographs of radiation monitoring systems.*

sured memory supply current increases because of the TID effect as it is presented in Chapter 6.1.4. Knowledge of memory temperature is necessary to make a temperature correction of the measured SRAM current. The analysis of memory and board supply currents provide information about TID damage effect and dangerous Single Event LatchUps (SELs) [21-A]. The device is protected against SEL using a current-limited power supply and polymer-based resettable fuses. No SEL has been observed in the tested devices in Linac II and TTF 2 tunnels [21-A].

The first version of the RadMon has a serious disadvantage, the maximum operable memory was limited to 128 kB. The whole system was designed in 5 V technology, therefore it was possible to connect only 5 V memories. The one cycle scanning time was below 1 second for 128 KB chip. The second device was designed using low voltage circuits therefore the memory supplied from 2.5 up to 5 V can be employed with capacities up to 128 MB. The system is able to scan a 2 MB memory within 30 s.

7.1.2 An application of programmable circuits to design readout system

Field Programmable Gate Array (FPGA) devices are often used to design digital circuits because of high speed of data processing and flexibility. The configuration of a FPGA circuit is usually stored in a SRAM, hence the device can be easily and quickly programmed many times [215]. An application of the FPGAs significantly simplifies the design process of electronic circuits.

Programmable devices can be used to design an efficient readout for the RadMon system [23-A]. In addition, the adaptation of FPGA allows to reduce the scanning time of the sensing memory and system restarts in case of Single Event Functional Interrupt (SEFI). However, the configuration SRAM of a programmable circuit can be

distrusted when exposed to neutrons because of the occurrence of SEUs as described in Chapter 2.2.3 and literature [216] . A readout circuit designed with an application of FPGA should tolerate radiation-provoked errors and therefore operate reliably in a linear accelerator tunnel. The readout system should be therefore constructed using FLASH-based devices. The ACTEL ProASIC FPGA family devices, produced in 0.22 µm technology, are good candidates to be used to design a radiation tolerant readout system. The data describing their vulnerability to neutrons and gamma radiation were studied before their selection [207–209]. Only SEUs were observed in user flip-flops during irradiation at Los Alamos [217, 218]. The cross-sections calculated for APA750 are equal to 3.1×10^{-13} cm^2·bit^{-1} for neutrons with energies below 1.5 MeV and 2.4×10^{-13} cm^2·bit^{-1} for neutrons with energies higher than 10 MeV. SEGR are only expected during FPGA programming when the device is supplied from 16 V. The ProASIC FPGA does not have a charge pump and the programming voltages are supplied externally. Moreover, contrary to SRAM-based devices, the FLASH FPGA storage element is not expected to be sensitive to SEU [219]. The maximum allowed TID for the ACTEL ProASIC fabrication technology should amount to at least 500 Gy(Si) [219, 220].

No SEL was detected in APA 750 and APA 1000 FPGAs during radiation tests [217, 218]. We can assume that APA 600 device should be also latch-up immune. Nevertheless, the resettable polymeric fuses were applied to secure other devices against SEL. Thus, the APA ProASIC plus devices are ideally suited as control devices of the readout system. An utilisation of FLASH-based FPGAs may eliminate a part of SEU-generated errors. Nevertheless, SETs can be still triggered in the control logic in both FPGA-type circuits [46].

The RadMon was implemented in a commercial FPGA to examine its suitability for the usage in a radiation-tolerant readout. FLASH–based devices made by ACTEL were taken into consideration.

A radiation tolerant readout implemented in FPGA

ACTEL APA 600 ProASIC family programmable circuit has been chosen to construct the fourth version of the RadMon readout [18-A, 22-A, 23-A]. The device cooperates with a compact version of sensing memory that is composed of four 512 kB stacked memory modules, see Chapter 6.1.4. Configuration data are stored in the internal FLASH memory of ACTEL circuit that is much more immune to SEUs comparing to SRAM. The principle of its operation is similar to the previous version of RadMon 2.0. A simplified block diagram of the FPGA-based reader is presented in Figure 7.4. The device consists of the main finite state machine (FSM), responsible for supervision of

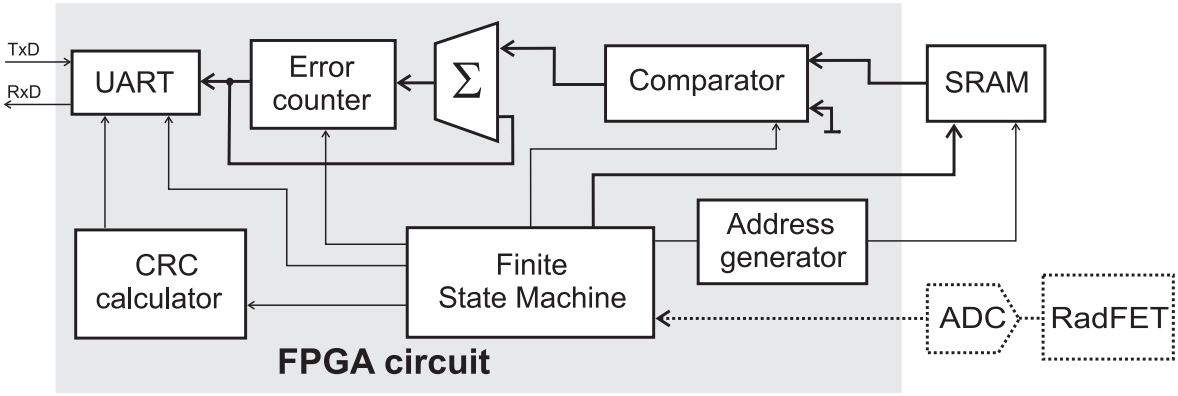

Figure 7.4: *The block diagram of the FPGA-based RadMon (version 4.0)*

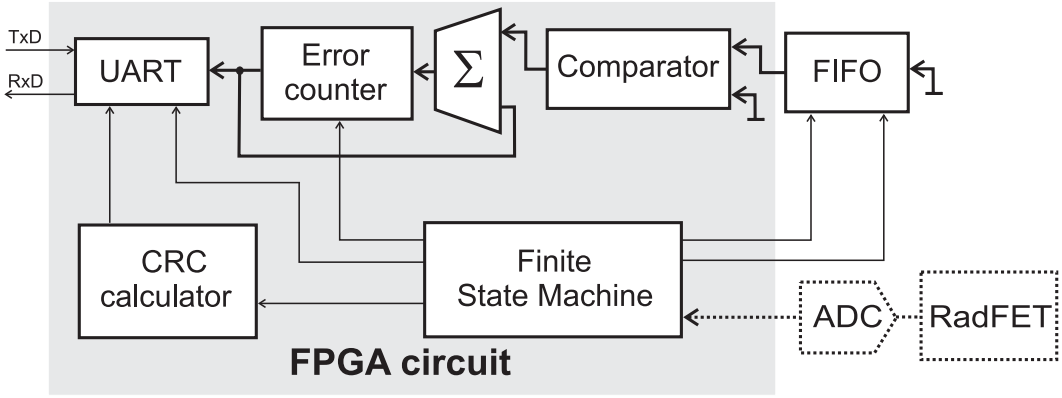

Figure 7.5: *The block diagram of the FPGA-based readout system of FIFO memory RadMon (version 5.0).*

all submodules. The SRAM memory is programmed after restart. Suitable information is sent to the main PC computer when the programming is finished and verified. Then, the continuous scanning process of the memory begins. When an error or errors are detected, the error counter (EC) in increased and corrected data is written into the memory. The number of detected SEUs is sent to the PC after a whole scanning cycle. A heartbeat frame must be transmitted in the period of time shorter than 10 seconds to avoid triggering off an external watch-dog. The data sent are secured with a 32-bit CRC checksum to avoid transmission errors and to verify the correctness of the reader operation. The digitalised RadFET's threshold voltage is delivered every 10 minutes.

The fifth version of the readout system dedicated to supervision of FIFO memory was also implemented in the ACTEL FPGA. A lower density programmable circuit APA150 was utilised because of the simplified construction of the FIFO reader. The block diagram of the reader is illustrated in Figure 7.5. The reader uses almost the same submodules as the version fourth. However, the memory interface is slightly different. The address counter has been eliminated. The output 9-bits data bus of the FIFO is connected to a comparator, while logical zeros are delivered to its inputs. The

Submodule	FSM type	Number of states	Total number of states
Control FSM	safe, gray	31	32
CRC calculator	safe, onehot	8	248
UART	safe, gray	20	32
SPI	safe, onehot	9	503
Address generator	safe, onehot	6	58

Table 7.1: *The summary of the designed FSMs of the readout system.*

main FSM generates only write and read signals.

A selective TMR was applied to immunize designed readers against neutron provoked SEUs [23-A]. The FSMs, which control reader's operation, i.e. a CRC calculator, an universal asynchronous receiver transmitter (UART), a serial peripheral interface (SPI), an address generator and the main control circuit, are the most crucial elements of the system when radiation immunity is taken into consideration. Circuits were implemented in Libero IDE with Synplify synthesiser. The Synplify can generate three types of state machines: one-hot, gray and sequential. Even though the synthesiser produces a highly optimal final implementation of FSMs that were immunised using TMR, their application in circuits operating in a harsh radioactive environment cannot be accepted. Synplify optimizes away all transition states and logic that cannot be reached to enhance both speed and circuit area [221]. However, FSM can get stuck in an invalid state when a SEU is generated in the FPGA structure. Therefore, the FSM has to be designed in a way to enable transitions from all invalid states into defined safe state. Parameters of the employed FSMs are summarized in Table 7.1 [22-A].

One can notice that the total number of states for the onehot FSM is much higher than the number of usable states. A onehot machine is very efficient with regards to both occupied resources and speed. Nevertheless, this type of FSM is suitable to applications with a low number of states. All FSMs in the presented readers were equipped with a reset logic for illegal states [23-A].

A Synplify synthesiser has been applied to implement selective and conventional TMRs [23-A, 24-A]. Firstly, a standard description of the readout was prepared using a very high scale integrated circuit hardware description language (VHDL). The synthesis was then executed, however input-output cells were not implemented. Computer program has been written to substitute automatically a collection of flip-flop primitives with their tripled versions equipped with voting circuits. Moreover, the software allows applying the redundancy to desired selectively chosen submodules. The exemplary modified D-type flip-flop is depicted in Figure 7.6. The circuit is ready for a final synthesis when the substitution process is finished. The amount of required resources

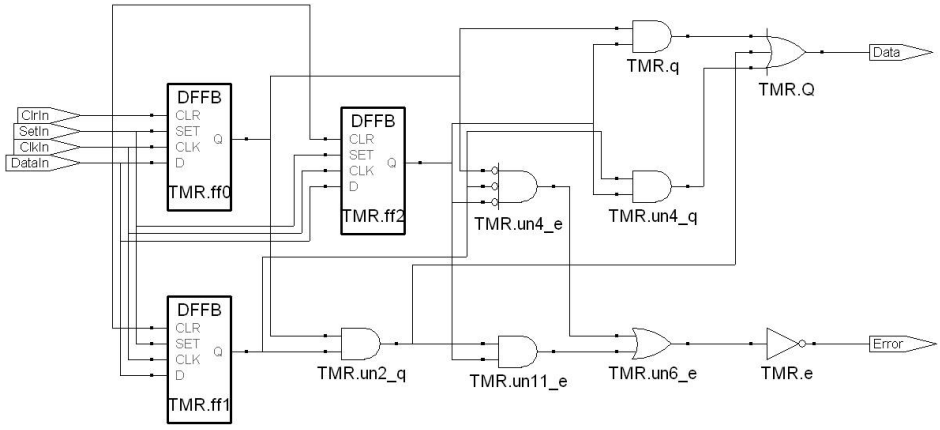

Figure 7.6: *A standard flip-flop with an asynchronous reset and preset that was modified using TMR.*

was increased significantly after the synthesis depending on the applied redundancy method. The comparison of FPGA resources consumed is presented in Table 7.2[1]. The amount of storage elements used increased 2.9 times when the TMR was utilized. The usage of STMR allows to save some FPGA resources, the factor is equal to 2.7. Additional combinational primitives were also required for voters. Moreover, the readout of the FIFO memory was simplified compared to the RadMon 4. In particular, the number of required input-output pins was smaller and therefore a lower density FPGA APA 150 has been used [23-A]. Almost three times more flip-flops were required when TMR was employed. The RadMon 5 may be further simplified when a dedicated memory is used, the FIFO memory produced by IDT needs a lot of connections to enable its initialisation. The custom memory may only have three control signals read, write and reset (not counting data buses), see Figure 7.5.

Irradiation tests of different RadMon reader versions Designed readers were subjected to radiation during experiments with an application of different memories [2-A, 23-A, 25-A, 26-A]. The devices were irradiated with americium-beryllium neutron source and inside Linac II and VUV-FEL tunnels as described in Chapter 5.2. During sensitivity tests with ^{241}AmBe no significant malfunctions were observed. The devices, similarly to sensing SRAMs, were placed in the nearest proximity of the neutron source. All above mentioned systems were able to read the memories and therefore supply numbers of generated SEUs. However, short interruptions in the RadMons' operations were observed when the devices were irradiated in accelerator tunnels. It should be

[1] An APA150 programmable circuit was used to design the readout dedicated to a FIFO memory, while the standard SRAM version employed APA600 device. Hence, the RadMon supervising the FIFO memory was synthesised intentionally for larger APA600 FPGA to facilitate their comparison. The microcontroller-based reader RadMon 3 required RAM and FIFO resources whereas RadMon 4 and 5 do not used them.

Device version	FPGA resources		Tiles		Gates	
	Core cells	I/O pads	Logic	Storage	Logic	Storage
Readout system of a 32-bit SRAM device based on APA600 FPGA						
RadMon 4	12.6 %	37.2 %	2158	559	4387	4328
RadMon 4-TMR	22.3 %	37.2 %	3188	1599	6375	12369
RadMon 4-STMR	21.7 %	37.2 %	3126	1537	6251	11873
Readout system of a FIFO memory based on APA150 FPGA						
RadMon 5	11.1 %	26.9 %	1938	495	3853	3813
RadMon 5-TMR	20.1 %	26.9 %	2926	1452	5836	11178
Radiation tolerant microcontroller-based readout						
Microcontroller RadMon 3	55.3 %	75.0 %	9118	2767	16310	21747
	RAM or FIFO cells		**RAM or FIFO**		**RAM or FIFO**	
	64.3 %		329472		288	

Table 7.2: *The comparison of occupied FPGA-resources of various RadMon reader versions.*

emphasised that DMR does not allow to maintain the correct operation of a system when an error is triggered in critical module. Therefore, restarts of the systems were necessary to enable a correct measurement of SEUs in the RadMons' sensing memory.

Three systems, based on RadMon 2 readouts, were equipped with different memories and placed in the VUV-FEL tunnel for two months, see Chapter 5.2. The malfunctions registered in the systems are gathered in Table 7.3. The systems were installed opposite the accelerating module AAC1 approximately 20 cm from the concrete wall. Most of the failures of readouts were detected by comparators and eliminated by restarts of systems. However, data measured by RadMon 2.2 were not sent to PC computer after 1219 hours of operation. The PC computer had to generate a reset

Device	Malfunction type	Time of operation [h]
RadMon 2.1 2 MB bare chip	Desynchronisation	845
	Desynchronisation	1210
RadMon 2.2 1 MB in moderator	Desynchronisation	305
	Desynchronisation	840
	Denial of service	1219
RadMon 2.3 2 MB in moderator	Desynchronisation	45
	Desynchronisation	409
	Desynchronisation	1350

Table 7.3: *Restarts of different RadMon 2 devices during two months irradiation in VUV-FEL tunnel.*

Device	Malfunction type	Time of operation [h]
RadMon 2 2 MB with moderator 3 month test	Desynchronisation	393
	Desynchronisation	427
	Desynchronisation	429
	Desynchronisation	487
	Desynchronisation	501
	Desynchronisation	661
	Desynchronisation	902
	Desynchronisation	942
	Desynchronisation	1152
	Desynchronisation	1207
	Desynchronisation	1557
	Desynchronisation	1605

Table 7.4: *Restarts of the RadMon 2 device within 3 month exposure.*

signal after 150 s to revive the system. However, exact details of the failure are not known. The history of the further three-month operation of RadMon 2.0, that supervised a 2 MB memory sensor and gauged neutron fluence and gamma radiation in the VUV-FEL tunnel is depicted in Table 7.4. The RadMon 2.0 operates reliably even if a few desynchronisations occurred.

RadMon 4 and 5 devices were installed in the VUV–FEL tunnel at the same time. No system restarts were recorded. The neutron fluence quantified by RadMon 4 was comparable with the fluence gauged by RadMon 2.0. The system cooperating with a FIFO memory has not measured any SEUs. The memory was insensitive to neutrons during sensitivity tests described in Chapter 6.1.3. However, the readout system has not demonstrated any faultiness.

A radiation-tolerant microcontroller implemented in FPGA

A programmable processor able to operate in a radioactive area can be also employed for the supervision of the sensing memory. Therefore, another version of a readout system, called RadMon 3, has been constructed using a radiation-tolerant microcontroller and its suitability for radiation monitoring in a accelerator tunnel has been tested [24-A].

A Harvard architecture of a reduced instruction set computer (RISC) based on a Microchip PIC16C57 core was adapted to design the device. The microcontroller, similarly to previous versions, has been implemented in APA 600 FPGA, see Chapter 7.1.2. The device operates in a similar way as the RadMon in version 1 or 2. However, only one microcontroller is required for a reliable reading in this case. The original Microchip microcontroller supports 33 instructions. Most of them can be executed within a single machine cycle. A data memory is implemented in the internal SRAM of the

FPGA. The microcontroller cooperates with an external SRAM chip that is used as a program memory. The irradiation tests of SRAMs described in Chapter 6.1.3 allow to select the most suitable memory. Hence, the Renesas memory has been utilised as the most radiation immune chip. The program executed by a microcontroller must be copied from an additional non-volatile FLASH after each restart. The application of SRAM allows to execute the program much faster. The number of digital ports is increased in order to facilitate the control of the sensing memory. Moreover, some additional commands and registers are added to enable FLASH memory programming and the analysis of SEUs generated in various submodules. A simplified block diagram of the radiation-tolerant microcontroller, showing the most important submodules, is shown in Figure 7.7. The software for the microcontroller can be developed using

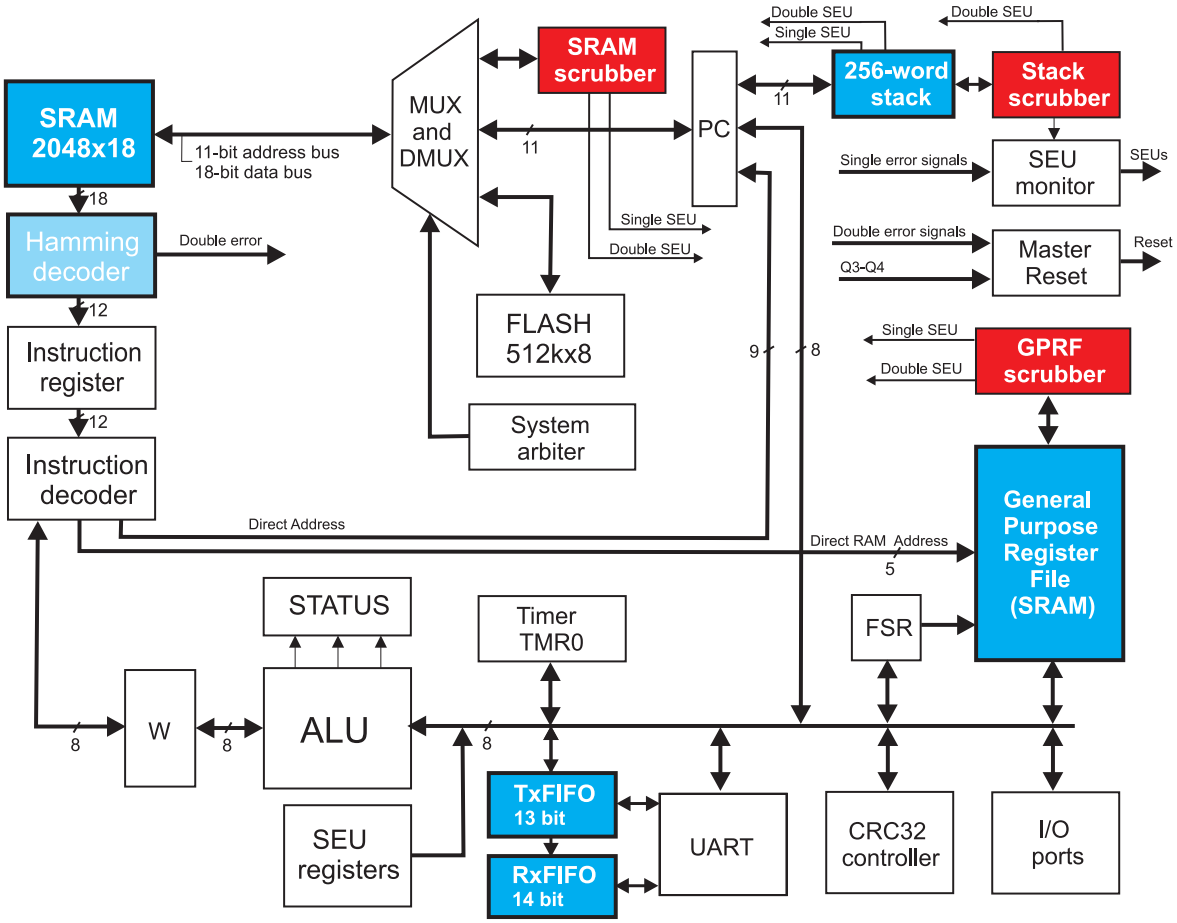

Figure 7.7: *A block diagram of the radiation-tolerant microcontroller. The modules mitigated with an application of Hamming codes are marked with the blue colour, while scrubbers are marked with red. However, only one Hamming decoder that decodes data from program memory is presented.*

available tools dedicated to the microchip PIC16C57 microcontroller, like: integrated design environment (IDE), C or Basic compilators.

Hamming codes, TMR and memory scrubbing were employed to immunize the

Submodule	Hamming code protection	Memory scrubber
Program Memory	(18,12)	Yes
SRAM register file	(13,8)	Yes
Stack	(16,11)	Yes
UART transmitter FIFO	(13,8)	No
UART receiver FIFO	(14,9)	No

Table 7.5: *Mitigation techniques used for the protection of FPGA-based microcontroller submodules.*

microcontroller against SEUs [24-A]. The external SRAM is utilized as a main program memory, while stack, general purpose register file (GPRF) and data receiver and transmitter FIFO are implemented in FPGA resources. Therefore, Hamming encoders and decoders were applied to secure used memory segments. Protected memory segments have different widths of their data buses and therefore the amount of redundant data is various. A Hamming decoder is necessary for the checking the correctness of program memory. Data are recovered from an external FLASH memory if any error is found. Other segments require a full EDAC circuit, see Chapter 3.3.2. Hamming codes allow to correct every single error and detect double. The microcontroller is restarted when the double error is detected and Hamming decoder is not able to cope with it. Moreover, a memory scrubbing has been applied to avoid the accumulation of errors in the program memory, stack and GPRF, see Figure 7.7. The scrubbing period is equal to 1 second. The period can be easily decreased when a significant number of system restarts will be observed. The program memory scrubbing time is equal to 0.12 ms, assuming that 10 percent of the memory is in an erroneous state. A dedicated system arbiter is required to allow the access to program memory by a memory scrubber. When the scrubber obtains an access to the program memory, the microcontroller is halted. The program memory is tested on the falling edge of phase Q4, whereas GPRF is inspected in the middle of phase Q4 or when the result of ALU operation is stored. The stack is monitored, if the address is popped from it. FIFO memories of the UART transmitter and receiver are not equipped with memory scrubbers because their data have a short life-time and SEUs generated in these memory segments are not a threat for the microcontroller operation. Moreover, the data are secured with CRC 32 checksum, thus errors can be easily detected and recovered by the retransmission [24-A]. Parameters describing utilized Hamming codes and memory scrubbers are summarised in Table 7.5. FSMs responsible for supervising the microcontroller submodules and other sequential components are protected using TMR. The algorithm describing the application of TMR in a Libero environment is described in

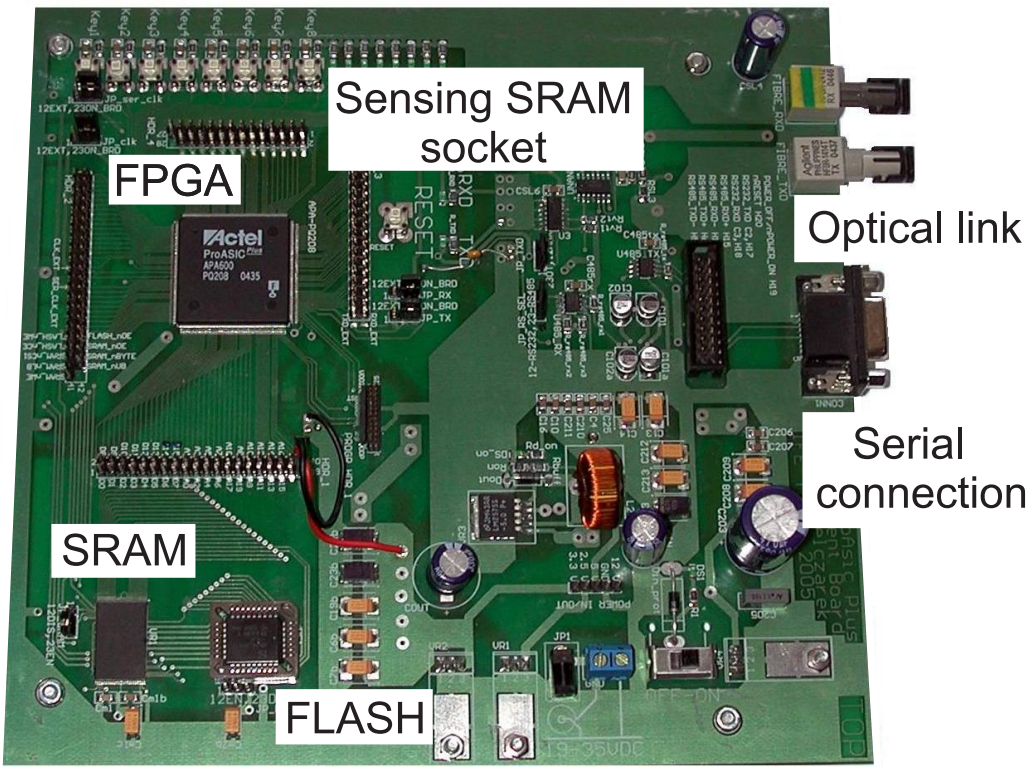

Figure 7.8: *The photograph of the radiation-tolerant microcontroller.*

Chapter 7.1.2. The amount of FPGA resources consumed is presented in Table 7.2. One can notice that a microcontroller-based version needs much more resources than RadMon in version 4 or 5. Moreover, RAM and FIFO blocks were utilised. The device requires two times more general purpose input-output (GPIO) ports than RadMon 4. Moreover, additional SRAM and FLASH memories were required to be connected to the microcontroller. Therefore, the device is much more complicated than the previous versions of RadMon reader.

The photographic view of the microcontroller-based RadMon is presented in Figure 7.8. The system is able to communicate with an external PC computer using various interfaces, i.e. EIA 232 or differential EIA 485 [119]. Moreover, data were transmitted using a full-duplex 62.5/125 micron multimode optical link. The system has been installed in the Linac II accelerator. Data were transmitted over a 60 m cable and an optical fibre. However, no error was observed during a 24 hour transmission. Experiments were repeated using different media for the transmission.

The exposure executed with an application of americium-beryllium does not show any errors in microcontroller modules. Therefore, the complete system that was equipped with a 1 MB stacked memory has been irradiated in the Linac II tunnel for 72 hours [119]. The system has been installed in the nearest proximity of the neutron source, five meters from the electron-to-positron converter. Only five errors were detected in receiver UART registers during the exposure. All of them were corrected

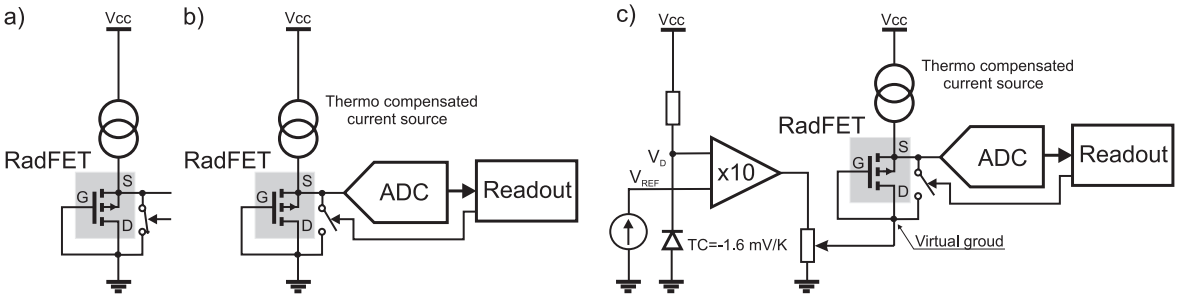

Figure 7.9: *The RadFET reader during the exposure a) and while the reading process b) and c). The simple version of the reader is presented in b), whereas a reader with applied temperature compensation is depicted in c).*

using TMR. The Hamming-based EDAC and scrubbing circuits had no occasion to correct any errors. The device was able to supervise the sensing memory for the 72 hour exposure. No errors in the transmission were registered. A strong correlation between SEUs provoked in UART registers and PIA current were observed. The sensing memory supplied from 5 V registered 500 upsets. The memory scanning period was equal to 120 seconds.

7.1.3 The RadFET readout subsystem

The RadFET dosimeter can operate in two different modes: SM when exposed to radiation and in RC whereas reading. Simplified schematic diagrams illustrating RadFET operation in both modes are presented in Figure 7.9 [27-A]. The constant current is flowing through the RadFET during reading. A temperature compensated current source has been applied to avoid errors in a measured threshold voltage of RadFET sensor, caused by temperature changes in the accelerator tunnel [28-A]. The amplified threshold voltage is digitalised using a 16-bit analog-digital converter (ADC) and then sent to the PC computer.

A 4 kÅ implanted version of RadFET dosimeter was finally chosen as a ionizing radiation sensor, see Chapter 6.2. The detector is composed of two pairs of PMOS transistors, which have channel width and length parameters equal to 300/50 and 690/15 µm respectively. The 300/50 version is dedicated to the operation with a lower current about 10 µA whereas the 690/15 requires higher current up to 100 µA [27-A]. The readout of the RadFET threshold voltage depends on its temperature. Moreover, the temperature coefficient (TC) of the RadFET sensor is various for different sensing currents. The temperature coefficients of the 4 kÅ implanted non-irradiated RadFET are depicted in Figure 7.10. One can notice that the temperature coefficient is equal to zero for the particular reading current, called zero temperature coefficient current (ZTC). ZTC currents are equal to 13 µA and 125 µA for 300/50 and 690/15 RadFETs,

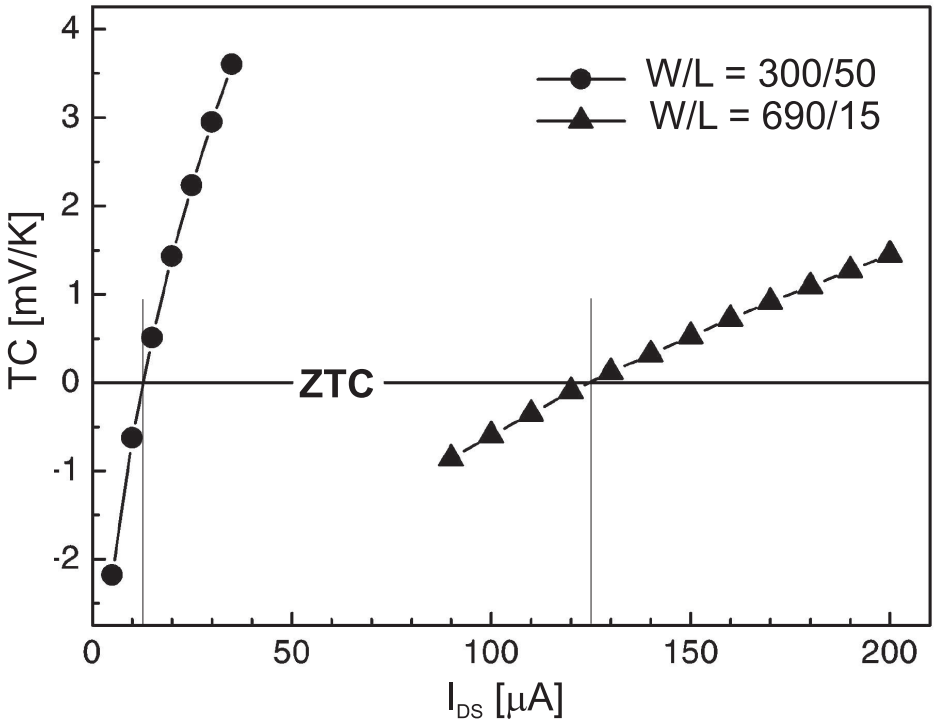

Figure 7.10: *Temperature coefficients versus drain-source current I_{DS} of 300/50 and 690/15 400 nm implanted RadFETs [180].*

respectively. Various solutions can be applied to compensate the negative influence of the temperature on the measured gamma dose. The simple version of the reader has been used when the device operated with ZTC.

An additional compensation circuit has been designed to eliminate the influence of TC on the readout, see Figure 7.9. A standard silicon diode has been applied as a thermometer [27-A]. The difference between the reference voltage V_{REF} and the drop voltage V_D on the diode is amplified and utilised as a virtual ground. When the temperature increases, the diode voltage V_D will be decreased, therefore the virtual ground will be also lowered. The increased threshold voltage will be compensated (assuming that the RadFET has a positive TC).

An additional temperature sensor is added to monitor the RadFETs temperature [27-A]. The thermometer is also used to measure the temperature in the tunnel to estimate the maximum temperature changes within a year. The temperature measured in the VUV-FEL tunnel within two months is depicted in Figure 7.11 [27-A]. The temperature does not change more than 10 °C within this time, however during the year the changes can be higher. Both methods allow to decrease the influence of TC and therefore enhance the accuracy of measured gamma radiation. According to the literature a small increase of ZTC has been observed when the device was exposed to radiation [180].

The standard readout system supervising the 300/50 RadFET has been finally

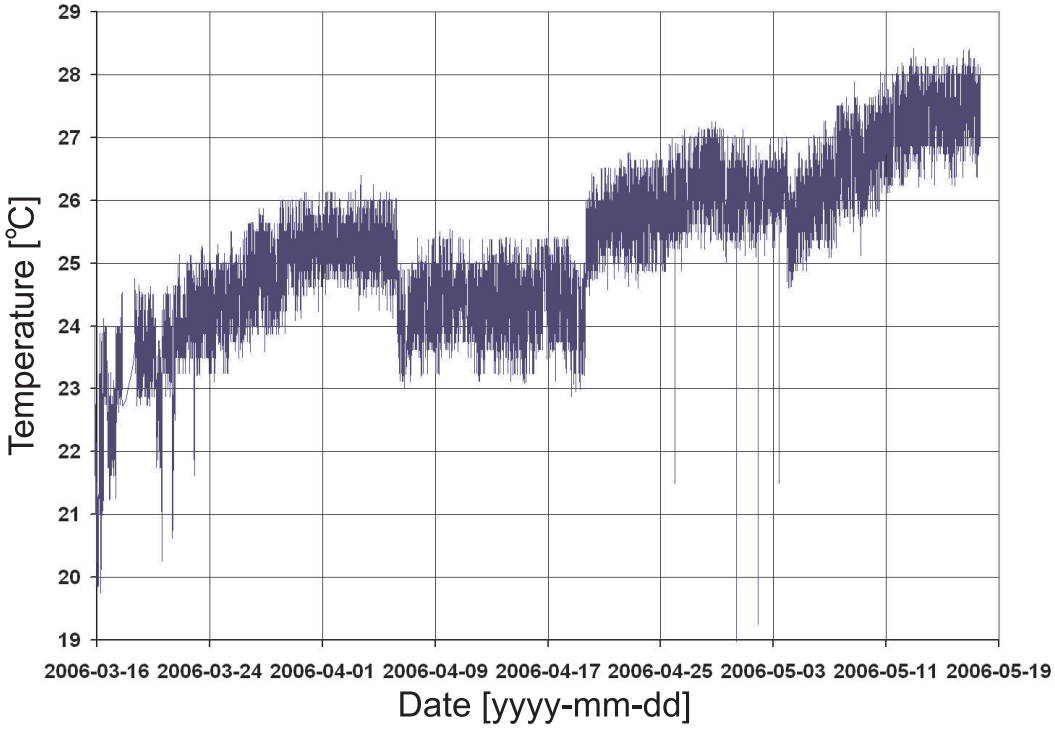

Figure 7.11: *The temperature measured in the VUV-FEL tunnel.*

chosen [27-A]. The results of the irradiation are presented in Chapter 6.2 and in Chapter 7.1.4.

7.1.4 The prototype of the RadMon device installed in VUV-FEL

Finally, the device equipped with a 2 MB stacked memory neutron-fluence detector and the 4 kÅ implanted RadFET has been installed in the VUV-FEL tunnel. The system was built using RadMon 2 readout based on redundant microcontrollers. The device was installed at the right side of the accelerating module AAC1 approximately 20 cm from the concrete wall, see Figure 1.2. The accumulated gamma radiation and neutron fluence characteristics registered during 2 months of operation are presented in Figure 7.12 [27-A].

The system was turned off for 10 hours during the exposure. One can notice a significant increase of neutron fluence in Figure 7.12. The SRAM memory has not been able to register any errors, however radiation was continuously generating defects in the silicon dioxide structure of RadFET dosimeter (the neutron fluence characteristics is flat, whereas the gamma dose is continuously increasing). Therefore, 5000 SEUs were added to avoid the desynchronisation of both curves and allow further analysis. During the exposure the SRAM memory registered 48910 SEUs, while the threshold voltage of RadFET sensor has been increased by 0.26 V. The RadMon system has been

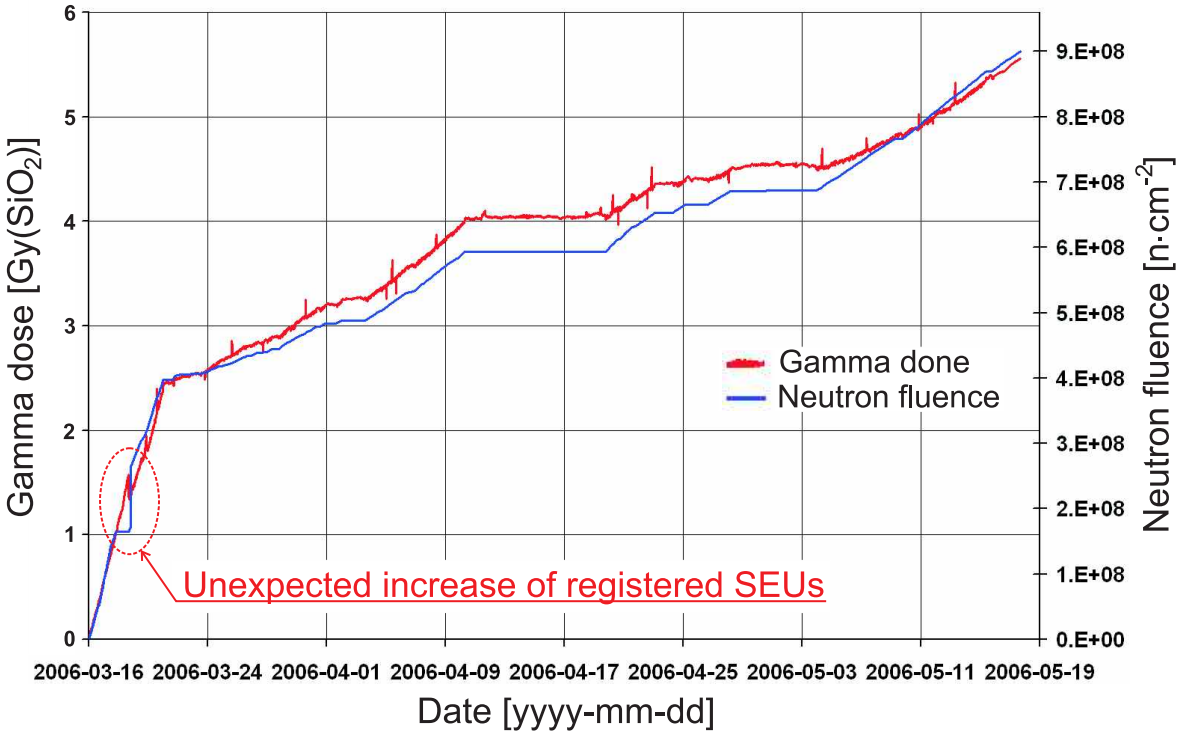

Figure 7.12: *The accumulated dose of gamma radiation and neutron fluence registered in VUV-FEL tunnel.*

Calibration factor	Dosimeter	
	SRAM device	RadFET
Neutron fluence	1.85×10^{4} n·cm^{-2}/SEU	–
Silicon kerma	1.17×10^{-3}Gy(Si)/SEU	–
Gamma dose	–	46.3 mV/Gy(SiO_2)

Table 7.6: *Calibration factors for SRAM-based and RadFET dosimeters.*

restarted five times.

The calibration of SRAM memory was executed in-situ in the VUV-FEL tunnel. A bubble dosimeter was used as a reference. The gamma detector was calibrated using a ^{137}Cs source. Obtained calibration factors for dosimeters are depicted in Table 7.6.

A calibration factor allowing to calculate displacement kerma was estimated [222]. Displacement kerma can be helpful during the analysis of displacement damage caused by energy deposited in the form of displacement damage by neutron interactions.

7.2 Conclusions

Research allows to find out the most suitable architecture and design of the readout for the on-line radiation monitoring system dedicated to a linear accelerator. The application of various radiation mitigation techniques allows to design digital readout systems

that are able to operate in the radiation environment of a linear accelerator. Systems have been intentionally built using COTS elements to obtain a cost-effective solution. However, an application of commercially available components enables only to mitigate SEE. The resistance to ionising radiation, in particular to TID, is strictly imposed by a fabrication technology and design of electronic circuits. Therefore, irradiation sensitivity tests should precede the design process of electronic devices and systems to select the device that is the most radiation immune. Some institutions, which carry out research in radiation fields, like NASA, CERN and ACTEL have made databases with results of sensitivity tests of various electronic components available. Therefore, the analysis of available data allows to select the most suitable device. However, the sensitivity to radiation of various devices is strongly dependent on fabrication technology, therefore circuits' sensibility should always be verified.

Performed tests show that both microcontroller- and FPGA-based systems are able to operate correctly when subjected to the neutron influence from americium-beryllium. However, a long-term irradiation in the target environment of the linac driving the VUV-FEL laser reveals the advantage of FPGA-based system over the microcontroller version. The FPGA-based readout allows to scan the sensing memory incomparably faster. The parallel nature of the FPGA circuit allows to supervise a few SRAM chips at the same time. Moreover, the scanning time can be further shortened when more parallel SRAM-based dosimeters will be used. However, an application of distributed sensor that is composed of many SRAMs negatively affects its sensitive volume (SV). On the other hand, the usage of a parallel memory allows to enhance the overall sensitivity of the sensor.

The first constructed system based on two microcontrollers had a few serious limitations. The maximum operable memory was limited to 128 kB and it is necessary to supply the chip from 5 V. However, the system allowed to carry out first reliable tests of SRAM chip in the real accelerator environment and delivered information describing the threat to electronics installed in the Linac II chamber. The second version enabled to scan various SRAM and DRAM memories supplied from voltages from 2.5 up to 5 V. The main drawback of the system was long scanning time (30 seconds). Restarts of the RadMon 2.0 were unavoidable to guarantee a reliable operation when the desynchronisation was detected. Such a behaviour of the readout can be tolerated during a normal operation assuming that restarts occur adequately sparsely. The external watch-dog is activated only once when the microcontroller-based system does not send any frame.

One can observe a compromise between the total scanning time and the detectors sensitivity to neutrons. The sensitivity is increased when the larger memory is used, but the scanning time is also extended. However, the employment of FPGA devices allows

to use higher-density memories and does not lengthen the reading cycle. Therefore the full cycle scanning time below 100 ms can be obtained. The scanning time is crucial in case of the usage of the monitoring system to trigger an alarm signal when radiation level increases considerably. The response time is much more important than the sensitivity of the monitor for such an application.

The tested FIFO memory was insensitive to the neutron influence during sensitivity tests, hence it cannot be used for radiation detection. However, the application of FIFO memory can simplify the construction of the readout system and the detector. Concluding, a radiation-sensitive FIFO may be an ideal candidate for the neutron fluence detector.

The relatively short exposure of the radiation tolerant microcontroller proved that the device is able to operate in the harsh radioactive environment of the Linac II tunnel. However, much longer irradiation is desired to observe soft errors in the memory regions protected by Hamming codes and scrubbing mechanisms. The construction of the reader is very complex. The same effect can be obtained using much simpler device secured by TMR, i.e. RadMon 4 or 5. The construction of the RadMon 4 or 5 does not require any additional SRAM or FLASH memory, not counting the radiation sensor. RadMon 3 device is characterised with a very long scanning time (2 minutes). On the other hand, the application of the programmable radiation-tolerant microcontroller can be very useful when the system must be easily modified and adjusted to new design requirements. In such a case, the program can be easily written using an assembler or C language, debugged and implemented.

The data link between RadMon and AX4020 operates at a speed of 19200 baud. The reliable communication has been proved for distances over 60 m. For longer distances an EIA-232 interface can be easily substituted with EIA-485 standards, that allows sending data up to a few km. The is no need to used optical connections. Data transmitted from all RadMon systems were not stored in the database once for 10 hours because of damaged computer network. RadMon systems are connected to a computer network thorough EIA232–to–Ethernet bridges. Therefore, a dedicated bus is required to enhance the reliability of the distributed system and assure reliable continuous measurement of radiation doses.

The vulnerability of designed systems to neutron-generated SEU was tested. However, resistivity tests on total ionizing dose were not performed. Therefore, designed systems should be subjected to a strong gamma source, while the supply current of the most crucial components should be monitored. ACTEL devices can tolerate the ionizing radiation up to 500 Gy, therefore RadMon 4 or 5 are expected to be the most resistant systems to gamma radiation.

The obvious conclusion to be drawn from research is that the FPGA-based design,

RadMon 4 is the best solution for the distributed radiation monitoring system. The device has a simple construction and is able to scan a 2 MB memory sensor in less than 100 ms.

Chapter 8

SUMMARY AND CONCLUSIONS

A radiation monitoring system dedicated to gauging neutron fluence and gamma radiation in a linear accelerator tunnel are presented in this dissertation. The system is composed of two modules: radiation sensitive sensors and a radiation-tolerant readout system. Therefore, the presented work can be divided into two parts. In the first part, the author proposed to utilize a commercial static random access memory chip as a calibrated neutron fluence detector. The second part of the thesis is devoted to development of a radiation-tolerant readout system able to operate reliably in a linear accelerator tunnel. Neutron sensors developed by the author and five radiation-tolerant readouts systems built with an application of various electronic components have been exposed to neutron and gamma radiation obtained from different sources, i.e. ^{241}AmBe(α,n) americium-beryllium neutron source, in Linac II and VUV-FEL tunnels.

8.1 Neutron dosimetry

The application of a 128 kB SRAM and a memory reader installed in a safe non-radiation area have allowed to carry out preliminary experiments. During radiation sensitivity tests of various electronic components the author noticed that the amount of SEUs generated in a SRAM depended on the neutron flux in the accelerator tunnel. However, the sensitivity of the preliminary sensor was insufficient to be used for on-line measurements in VUV-FEL and X-FEL accelerators. In the first approach, the author utilized modern low-voltage high-capacity SRAMs. However, contrary to the author's predictions, the cross-sections of devices were reduced roughly two orders of magnitude instead of increasing when compared to the 128 kB memory. Thorough analysis has proved that the sensitivity reduction was caused by the absence of the BPSG layer in modern memories. This layer acts as a neutron to alpha particles converter. Therefore, the lack of BPSG excluded the usage of modern memories fabricated in 0.18 µm –

0.25 µm as neutron sensors. Further research reveals that 512 kB memories fabricated in 0.4 µm technology had the highest cross-sections and thus were the best candidates for the sensing component. However, the sensitivities of memories have not fulfilled the requirements for the neutron sensor. The author conducted further experiments aiming to enhance the detector's sensitivity. Series of exposures were carried out with 512 kB memories supplied with various voltages. The reduction of the supply voltage from 5 V to 3.3 V allowed to enhance the sensitivity 5.6 times because of the decreased critical charge of the sensitive part of the memory. The application of an additional 9 cm polyethylene moderator enhanced the sensitivity four times. Moreover, the total capacity of the sensing memory was increased four times. Applied methods allow to enhance the sensibility ninety times. The calibration of the sensor was executed "in situ" in the target operation environment of the VUV-FEL. The proposed calibrated neutron fluence sensor has a resolution of $1.84{\times}10^4$ n·cm^{-2}.

The proposed method allows to build a cost-effective sensor suitable for gauging neutron fluence in real-time. However, an ionizing chamber has still a better sensitivity in comparison with the presented SRAM-based sensor. The main drawback of the ionizing chamber is its response time. When the detector is used in pulsed radiation fields, like X-FEL or VUV-FEL, the dosimeter registers only the first particle or bunch of particles. The following particles are not counted during the dead time of the dosimeter. Therefore, the measured neutron fluence is underestimated. Moreover, ionizing chambers used for neutrons gauging are also prone to gamma radiation. The amount of gamma radiation is a few orders of magnitude higher than neutron fluence in VUV-FEL, thus fluence measurement results could be significantly affected. A SRAM-based sensor measures pulsed radiation correctly because of the fast response. Neutron particles generate SEUs in various memory cells of the SRAM matrix. Gamma radiation present in VUV-FEL accelerator is not able to trigger soft errors, therefore the detector can selectively measure neutron fluence.

Since there is no available SRAM-based neutron sensor or dosimeter that utilizes the SEU phenomenon to measure radiation, the approach suggested in the thesis is innovative and thus the first thesis can be considered to be proven.

The off-line neutron dosimeter

A non-volatility of a NVRAM device allows to use the electronic component for off-line radiation measurements. Such memories were used in various experiments during the development of the SRAM-based neutron sensor and concrete shielding. A NVRAM is composed of a standard SRAM and circuit supervising the memory supply voltage. During the exposure the memory can be supplied from the lowest voltage that is

required to maintain its contents. The retention voltage of the 512 kB Samsung memory can be as low as 2 V and therefore the sensitivity can be enhanced almost 20 times. As mentioned earlier, similarly to the sensing SRAM of the RadMon system, the NVRAM can be equipped with an additional moderator to improve further its sensitivity.

Hence, the most important conclusion is that a NVRAM device can be used as an off-line sensor or dosimeter. A non-calibrated memory can be employed during comparative measurements, whereas the device can be competitive to TLD or bubble dosimeters when the calibration is performed. The main advantage of the detector is its much higher neutron fluence saturation in comparison to bubble dosimeters and TLD. A NVRAM-based sensor can be used to measure maximum neutron fluence up to 10^{13} n·cm^{-2} for the 512 kB Samsung memory. The maximum detectable dose for a bubble dosimeter BD-PND fabricated by BTI is equal to $8{\cdot}10^{6}$ n·cm^{-2}, assuming that a hundred bubbles can be counted [223, 224]. The highest detectable fluence for a pair of dosimeters TLD-500 and TLD-700 is much higher up to $4{\cdot}10^{10}$ n·cm^{-2} [1-A]. However, both TLD dosimeters are sensitive to gamma radiation and the practical maximum measurable dose in a mixed radiation field of linear accelerator is lower. The amount of gamma radiation produced in an accelerator is much higher than neutrons. The measured in VUV-FEL ratio of gamma dose and neutron kerma is in range of a few hundreds [225]. Therefore, gamma radiation may result in a saturation of TLD dosimeters and the evaluation of measured doses may be impossible. Bubble and NVRAM-based dosimeters are gamma radiation insensitive.

The readout of the NVRAM is performed in a non-radiation area therefore the memory can be evaluated using a cost-effective not radiation-tolerant reader. All configuration parameters and calibration factors can be stored in the same memory as proposed in Chapter 6.1.2. The evaluation process of TLD dosimeters is much more complicated. Counting of bubbles generated in a bubble dosimeter requires an application of an expensive apparatus utilizing image recognition or sound detection. All above considerations fully confirm the second thesis of the dissertation.

8.2 An application of COTS elements to design rad-tolerant devices

The readout system supervising a neutron fluence sensor and RadFET detector had to be able to operate reliably in a radiation area of a linear accelerator. An application of dedicated radiation-hardened devices was considered during the design of the device. However, enormous prices of such components prevented from their use in the distributed radiation monitoring system. The employment of rad-hard components can

solve most of the problems caused by radiation influence. However, radiation-hardened devices are usually produced in small quantities, therefore there is no guarantee that devices or similar parts will be accessible in near future. Alternatively, much cheaper, commercially available electronic components were tested and finally used to design a radiation-tolerant readout system of RadMon. However, a dedicated design approach of electronic circuits or systems must be applied to create a device able to tolerate bit flips caused by neutrons present in an accelerator tunnel.

The application of COTS elements allows to design a reliable and cost-effective readout system for RadMon monitoring system. A few different versions of the system have been built and tested. Performed tests show that both microcontroller- and FPGA-based systems are able to operate correctly when subjected to neutron influence from americium-beryllium. However, a long-term irradiation in the target environment of the linac driving the VUV-FEL laser and Linac II reveals the advantage of FPGA-based system over the microcontroller version. The microcontroller-based readout device must be restarted when a SEU is detected, whereas the FPGA-based device can maintain its operation thanks to the application of TMR and Hamming codes. The FPGA-based device allows to scan the sensing memory incomparably faster. The parallel nature of the FPGA circuit allows to supervise a few SRAM chips at the same time. An employment of FPGA devices shortens the full scanning cycle suration below 100 ms. The scanning time is particularly crucial in case of the usage of the monitoring system to trigger an alarm signal when the radiation level in a tunnel increases considerably. The response time is much more important than the sensitivity of the monitor for such an application.

FLASH-based FPGAs were intentionally used to design readout systems because of their much higher immunity to soft errors in comparison to SRAM-based circuits. When the SRAM-based device is used, an external configuration memory scrubber is required. Some of the FPGAs with SRAM memories are equipped with internal scrubbers. Still, the interruption in the operation of devices is necessary when a soft error is detected in the configuration SRAM. In such a case their contents must be reloaded. Moreover, ACTEL FPGA are able to tolerate relatively high ionizing damage up to 500 Gy.

The microcontroller implemented in FPGA allows to test various mechanisms dedicated to enhance immunity of digital devices to SEEs. Employed scrubbers of memories and registers caused an imperceptible decrease in the computation power. Hamming codes and TMR were used for an efficacious protection of FSM, counters, dividers and other sequential components. The application of these devices resulted in the consumption of additional resources of the programmable device. The external watch-dog is always desired to revive the system when other mechanisms fail. The designed readout

system based on the microcontroller implemented in FPGA has a relatively long scanning cycle of the sensing memory equal to 120 s. The device requires three times more resources than the FPGA-based reader. Therefore, the FPGA-based reader secured with TMR and Hamming codes has been finally chosen. Designed readers dedicated to the RadMon system and results of radiation resistivity tests prove the third thesis.

The design process of radiation-tolerant systems

Experiences obtained during the design of readout systems of the RadMon system can help to design other radiation-tolerant systems. The design process can be summarized in five steps:

1. TID and the probability of SEE for given types of radiation that are present in the target area should be estimated. Moreover, a map of a radiation field distribution in a tunnel could be also helpful. The exact analysis of the map allows to find suitable places in the machine chamber or accelerator tunnel to install electronics, where the generated radiation reaches the lowest levels.
2. The system should be designed using well-known devices whose radiation sensitivities were already verified. The sensitivity of other electronic components that are going to be used in the system should be also tested. Information about radiation resistivity of some electronic components can be found in specialised research centres, e.g. CERN, NASA [207–209]. However, the radiation sensitivity of electronic components should be always verified experimentally.
3. When components are selected, the preliminary version of hardware can be designed. An additional shielding against ionizing radiation can be also applied. The device can be protected using methods described in Chapter 3. When a SEL is possible, fast current limiting circuits or other selected devices that not suffer because of SEL should be used.
4. The sensibility of the system should be tested in the accelerator or machine's vault. Moreover, the sensing memory and/or RadFET detector can be installed on the board together with other electronic circuits. Therefore, neutron fluence and TID can be easily measured during the exposure.
5. When the device fails radiation resistivity tests, the weak point must be found and the system must be redesigned.

Immunity to SEEs of electronic components can be improved when the hardware or firmware design of electronic circuits is modified. Methods used to design radiation-tolerant devices are described in Chapter 3. Contrary to SEE, the influence of TID effect on most electronic components cannot be improved using hardware or software

methods. Therefore, the electronics dedicated to an operation in a given radiation environments should be qualified correctly to stand the defined radiation levels including safety factors. The electronics can be protected against ionizing radiation by an application of additional shielding. It should be emphasised that SEE are always generated in COTS circuits, hence the applied hardware of software methods can allow to tolerate the errors and help to decrease the probability of the system inoperability.

The radiation sensitivity assessment of electronic components is a complex process. Therefore, it is desired to verify available data describing radiation susceptibility of a given electronic part in the target radiation environment, i.e. in an accelerator tunnel. The radiation environment of the VUV-FEL and X-FEL are not well defined, therefore the sensitivity of components used for the control system should be verified experimentally in their tunnels.

Carried out research has proved that electronic devices produced by various manufacturers in the standard CMOS technology reveal different susceptibility to SEE. Moreover, cross-sections of different samples of memories produced by the same company that are marked with the same labels are also different. Manufacturers of electronics components may change slightly the production process of electronic components without the notification of the end customer, e.g. can remove the BPSG layer. Therefore, the sensitivity of devices with the same labels, speeds, supply currents and voltages can be reduced or even enhanced.

Devices fabricated in submicron technologies tend to be more immune to ionizing radiation, whereas their susceptibility to SEE is increasing because of decreasing supply voltage and transistor's dimensions. Accordingly, new techniques that allow to enhance sensitivity to soft errors of a modern integrated circuits are still in progress. On one hand, BPSG layer was removed. On the other hand, dedicated correcting codes, like CRC, Hamming or RS, are implemented to reduce their sensitivity. Concluding, the devices are good candidates for the readout system, however cannot be applied as a sensing memory.

8.3 The optimal architecture of the neutron fluence sensor

A SRAM-based detector can be easily integrated with a digital readout circuit. Moreover, the sensitivity of the sensor can be enhanced when a dedicated ASIC is designed. The device can be equipped with a simple readout system with a serial interface, like Serial Peripheral Interface (SPI) or I^2C. Data received from the sensor by a standard FPGA or microcontroller can be protected using CRC code to avoid errors caused by

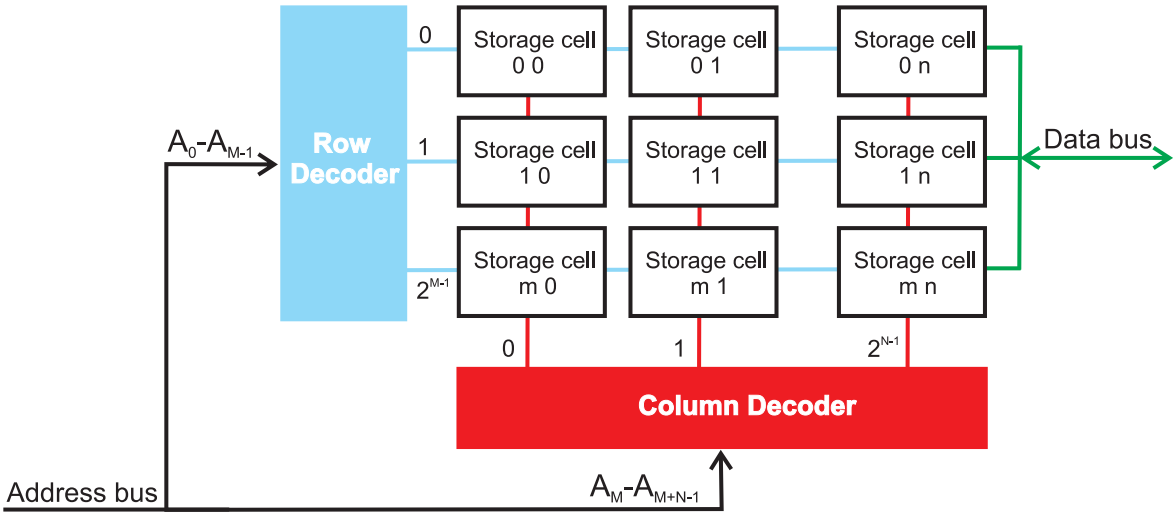

Figure 8.1: *An architecture of SRAM chip organised as an array of 2^M rows and 2^N columns [54].*

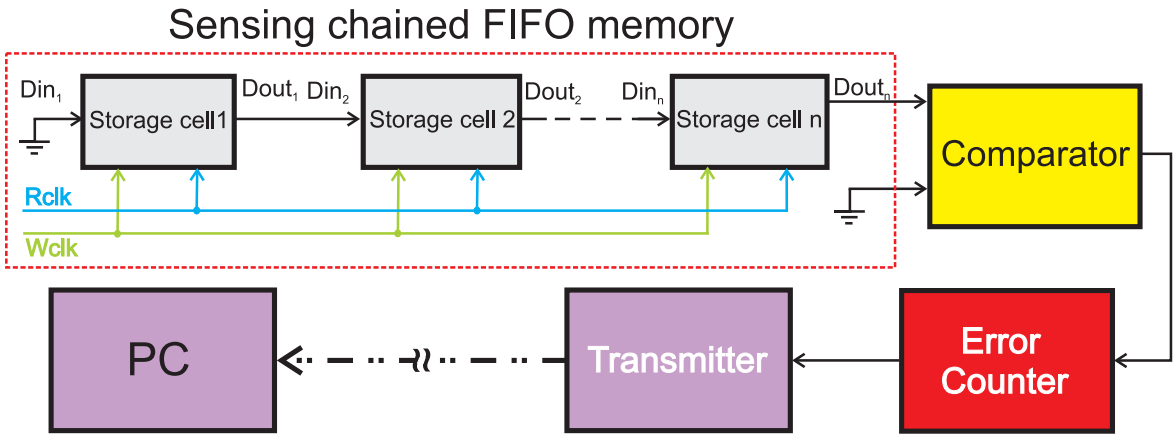

Figure 8.2: *An exemplary architecture of a chained FIFO memory-based neutron fluence detector.*

SEU in the receiver FIFO, its registers or FSM. However, the further analysis of a standard SRAM chip design shows that matrix architecture is not the optimal one taking into consideration the area of the sensing memory, access time, and production costs. The classic static random access memory chip is composed of a high capacity memory matrix cooperating with row and column address decoders, see Figure 8.1. Therefore, the readout system has to generate an address before the memory is read or written. The address generated by the reader must be decoded by row and column decoders to select the desired storage cell. However, the application of a simple chain first input first output (FIFO) memory allows to simplify significantly the construction of the readout system and reduce memory access time. When the FIFO memory is applied, row and column decoders are not desired as presented in Figure 8.2. The memory is fed with a pattern signal that is also used to control the correctness of output data of the memory chain. The FIFO sensor requires only a clock signal for a proper oper-

ation; data are written on the falling and read on rising edge. The induced SEUs in the sensing chain are counted by an error counter and sent to a PC computer or other circuit when the error is detected.

The reader cooperating with a FIFO memory has also been built and tested. However, the employed commercial FIFO memory was insensitive to the neutron influence during sensitivity tests, hence it cannot be used for radiation detection. The application of FIFO memory simplified slightly the construction of the readout system. The architecture of the readout circuit can be further simplified when the dedicated custom-designed FIFO memory (presented in Figure 8.2) is applied. The VHDL-based description of the FIFO readout system can be used to design the integrated circuit. Concluding, a radiation-sensitive FIFO may be an ideal candidate for the neutron fluence detector. The application of FIFO memory allows to design an optimal integrated neutron fluence dosimeter taking into consideration required silicon area, its sensitivity and costs. The sensor can be integrated with a radiation-tolerant readout system and fabricated as a cost-effective ASIC, similarly to the RadFET dosimeter. The circuit should be fabricated using a technology, which allows to apply a pure boron-10 isotope or other materials including ^{10}B, for example 0.25 µm technological process can be used to fabricate a SRAM-based dosimeter. Modern technologies with the feature size better than 0.25 µm are not suitable because a BPSG-layer containing ^{10}B has been substituted with PSG. Alpha particles produced during the nuclear reaction with ^{10}B have a short range up to a few micrometers in silicon. Thus, the layer including ^{10}B should be placed as close as possible to SV of the sensing memory structure to enhance the probability of SEUs and therefore the sensitivity of the dosimeter.

The radiation sensitive ASIC can be installed on each electronic board that is going to operate in the radiation environment, i.e. SimCom 3.1L. The radiation monitoring system can help to control radiation levels in crucial places of the linear accelerator tunnel in the nearest proximity of devices and systems employed to control the machine. Moreover, the distributed system can generate an alarm signal in emergency or critical situations when the level of radiation will be increased and pose a threat to electronics. In such a case the main control system of the accelerator can try to limit generated radiation, e.g. decrease an electric field gradient that supplies cavities. The presented architecture of the optimal neutron fluence dosimeter confirms the fourth thesis.

Chapter 9

APPENDICES

9.1 SRAM and NVRAM devices used during the experiments

The list of the memories used during various experiments and exposures is presented in Table 9.1.

9.2 Americium-Beryllium neuron source

An isotropic americium-beryllium ^{241}AmBe (n,α) neutron source is able to produce continuous fluxes of neutrons. Americium-beryllium source generates neutrons via the ^{9}Be(α,n)^{12}C reaction. The source has a long useful life with a relatively constant flux of neutrons. The half-life of the source is equal to 432 years. The source in kept in a package made of stainless steel that has a shape of a cylinder with 22.4 mm diameter and 31 mm height, see Figure 9.1. The neutron source generates neutrons incessantly, therefore it can not be turned off and must be stored in a housing made of a boronated-polyethylene. The activity of the ^{241}AmBe is equal to 1.0 Ci (37 GBq), therefore the source emits 2.2×10^{6} n·s^{-1}. The most important parameters of the source are depicted in Table 9.2. The number of neutrons generated per square centimetre decreases with increasing distance from the source. The neutron fluence rate depending on the distance from the source is depicted in Figure 9.2. The original energy spectrum of ^{241}AmBe neutron source is presented in Figure 6.2.

9.2.1 A water moderated Americium-Beryllium neuron source

For some experiments, the energy spectrum of a 1.0 Ci ^{241}AmBe (n,α) neutron source has been modified using water moderators. The neutron source has been placed in the

Memory reference	Memory capacity	Memory lot number	Supply voltage	Number of tested memories
Non-volatile SRAM				
bq4013MC-70	128 kB	35W007A	5 V	5
bq4014MC-70	256 kB	11ZM30Z	5 V	3
bq4015MC-70	512 kB	7BZ050W	5 V	4
bq4015MA-70	512 kB	5AZ014W	5 V	20
bq4015YMC-85	512 kB	7BZ039W	5 V	20
bq4015YMA-85	512 kB	6AZ020W	5 V	6
bq4016MC-70	1024 kB	11ZB01W	5 V	3
bq4016YMC-70	1024 kB	52ZZ03W	5 V	1
bq4016YMC-85	1024 kB	45A03W	5 V	1
bq4017MC-70	2048 kB	23Z004W	5 V	20
bq4017YMC-70	2048 kB	52Z001W	5 V	20
bq4017MC-85	2048 kB	12Z401W	5 V	2
bq4017YMC-85	2048 kB	52Z002W	5 V	2
DS1249AB-85	256 kB	52Z001W	5 V	2
DS1270W-100	2048 kB	52Z002W	3.3 V	2
SRAM				
KM68V1000BLTI-7L	128 kB	K65837	3.3 V	1
K6T1008C2E-DB55	128 kB	27BM70B6	5 V	2
CY7C1049CV-15VC	512 kB	R04615724	3.3 V	1
TC55VEM208ASTN-55	512 kB	KS3488	3.3 V	1
R1LP0408CSP-7LC	512 kB	441N2004	5 V	2
TC554001AF-70L	512 kB	K925160442	5 V	2
K6T4008C1B-VF70	512 kB	R1L287AA	5 V	5
K6T4008C1B-VB55	512 kB	TLKG65FBS	5 V	31
K6T4008C1B-GB70	512 kB	R1D007AA	5 V	20
K6T4008T1F-GF70	512 kB	TLKD3303	5 V	5
HY628400ALLT2-55	512 kB	0027A	5 V	2
IS61LV25616AL-10T	512 kB	X2183900E 0423	5 V	2
CY62148BLL-70SI	512 kB	0510 609083	5 V	2
M5M5408BFP-70H	512 kB	1171A0	5 V	1
K6X8008T2B-TF70	512 kB	TLTC09P2	5 V	1
M68AF511-AM70MC6	512 kB	FASAT0428	5 V	2
K6F8016V3A-TF55	1024 kB	TSB047CC	3.3 V	1
M5M5W816TP-55HI	1024 kB	517200	3.3 V	1
TC55VBM316AFTN-55	1024 kB	LO3125	3.3 V	1
K6X8016C3B-TF55	1024 kB	TLTH12PS	5 V	1
R1LV1616HSA-4LI	2048 kB	416G2001	3.3 V	1
TC55VBM416AFTN-55	2048 kB	L50228	3.3 V	1
TC55V8200FT-12	2048 kB	0432KAD	3.3 V	1
FIFO				
IDT72V2111-L15PF	576 kB	ZAF0013P	3.3 V	1

Table 9.1: *The list of memories used during experiments and exposures.*

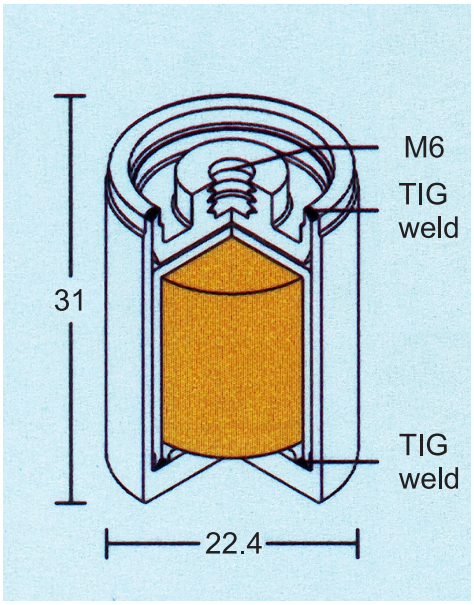

Figure 9.1: *^{241}AmBe calibration source.*

Table 9.2: *The datasheet of Americium-Beryllium neuron source.*

^{241}AmBe neutron source	
Active isotope	^{241}Am
Identification number	759
Activity (2006.08.01)	0.938 Ci
Initial activity (1966.10.01)	1.000 Ci
Neutron fluence conversion ratio	2.2×10^{6} n·s^{-1}
Average neutron energy	5.1 MeV

middle of polyethylene jars of different radii filled with a demineralised water [210]. Three different energy spectra of a water moderated americium-beryllium neutron source are presented in Figure 9.3. The first characteristics has been obtained for the raw source, the jars have been not filled with a water. The second characteristics has been obtained for the moderator thickness equal to 2.0 cm (equivalent to a jar radius of 3.5 cm) when the first jar has been filled with a water. The average neutron energy dropped from 5.1 MeV to 4.0 MeV. When both jars have been filled the average energy dropped to 3.3 MeV (moderator thickness equal to 6.25 cm).

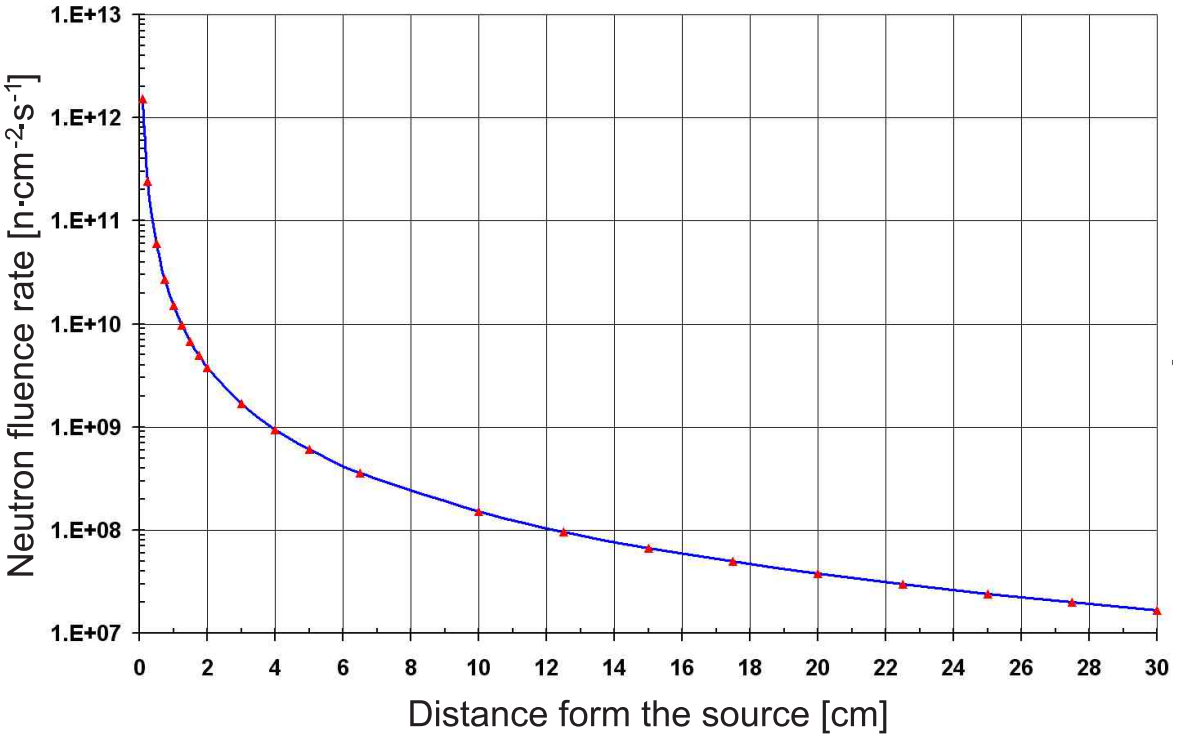

Figure 9.2: *Fluence rate of the $^{241}AmBe(\alpha,n)$ neutron source.*

Table 9.3: *The datasheet of a gamma source ^{137}Cs.*

^{137} Cs gamma source	
Active isotope	^{137}Cs
Identification number	EZ69066
Activity (2006.08.01)	3.315 Ci
Initial activity (1982.05.01)	5.929 Ci
Gamma conversion ratio	34038 (μGy·cm^2)/(mCi·h)
Energy of emitted photons	660 keV

9.3 Cesium gamma source

A strong gamma source has been used during RadFETs irradiations. The gamma source is kept in well-shielded lead castle, see Figure 9.4. The source can be turned on using a remote controller. The remote controller is applied to reduce the dose absorbed by personnel during experiments. The cesium source emits gamma photons with energy equal to 660 keV. The physical half-life is equal to 30.22 years, therefore the current activity of the source is reduced to 3.315 Ci. The most important parameters of the source are depicted in Table 9.3.

The dose rate of the source decreases with a distance. Therefore, the absorbed dose can be modified by exposure time or the distance between a target and the source. The calculated dose rate for distances up to 1 m are depicted in Figure 9.5.

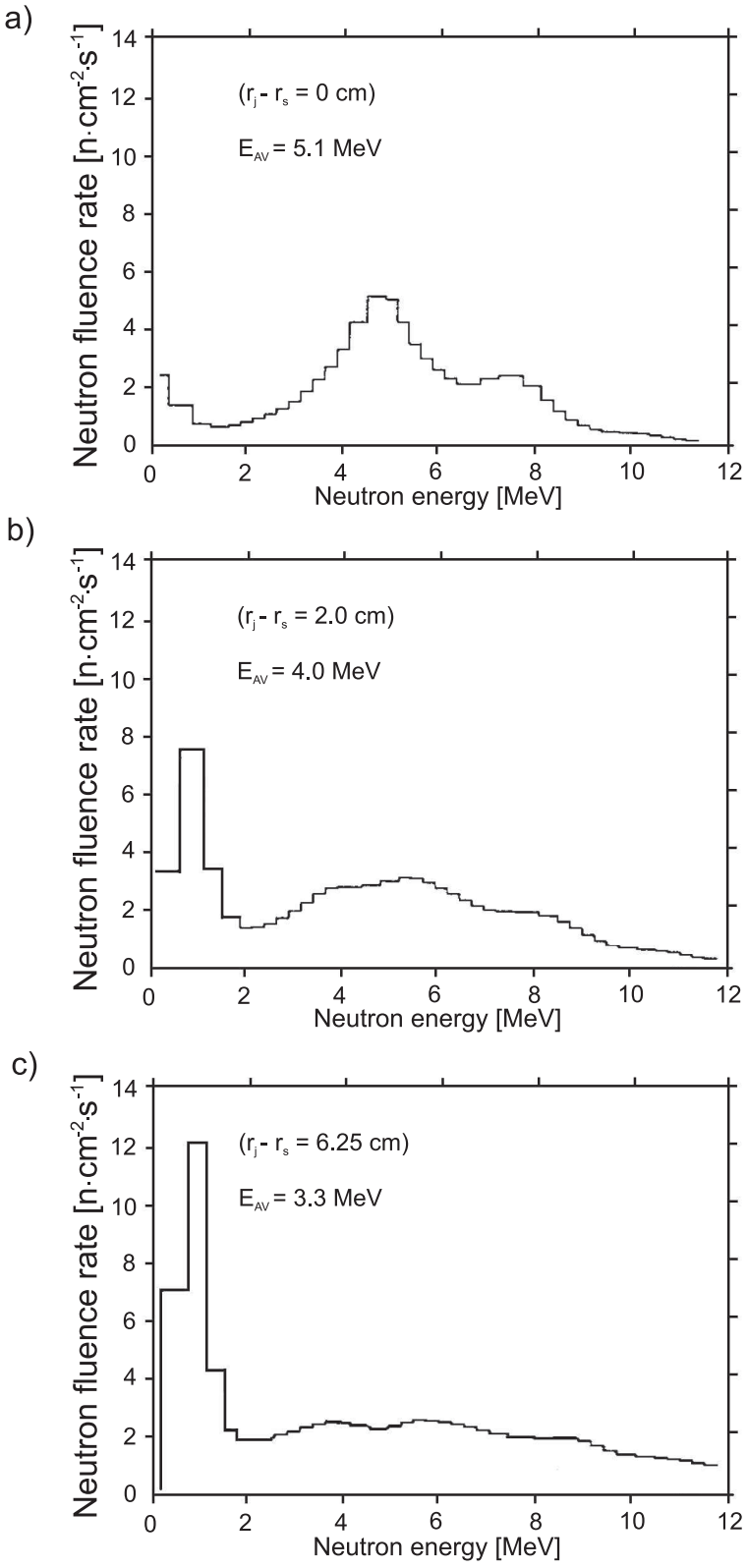

Figure 9.3: *Neutron spectra of ^{241}AmBe source slowed down using a demineralised light water moderator with layer thickness of a) 0 cm, b) 2.0 cm, c) 6.25 cm [210].*

Figure 9.4: *The ^{137}Cs gamma source.*

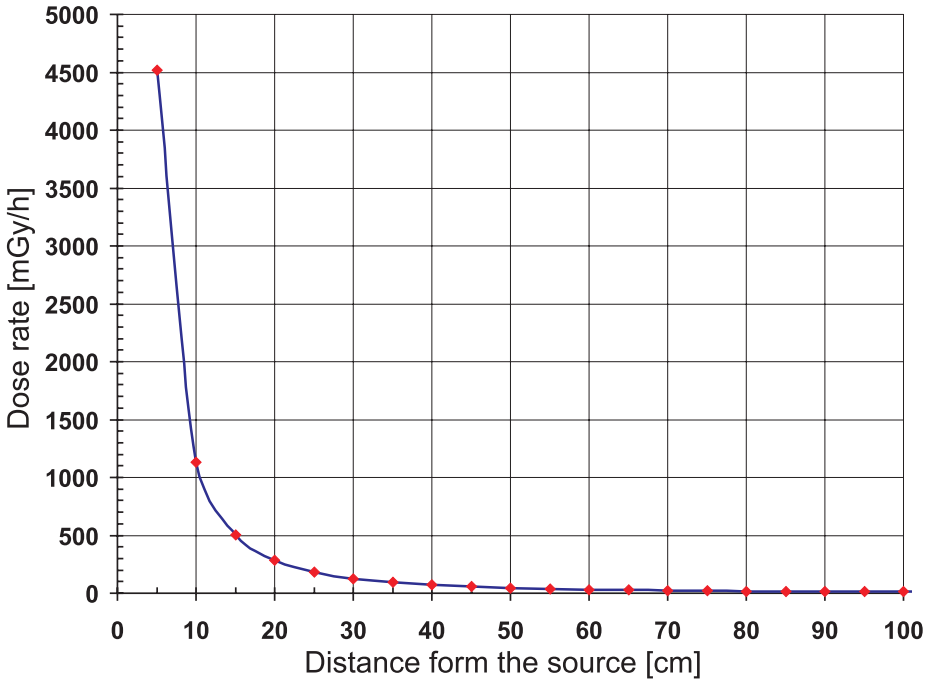

Figure 9.5: *The dose rate of the cesium gamma source.*

Table 9.4: *Specification of neutron attenuator.*

Active Components	
Hydrogen atom density per cubic cm	2.7×10^{22}
Natural isotope distribution	99.98 % ^{1}H
Boron atom density per cubic cm	2.32×10^{22}
Natural isotope distribution	19.6 % ^{10}B and 80.4 % ^{11}B
Weight percent of all isotopes of boron	25.35 %
Total Density	1.64 g·cm^{-3}
Radiation Properties	
Macroscopic thermal neutron cross-section	17.50 cm^{3}
Gamma resistance	1.0×10^{8} Gy
Neutron resistance	5.0×10^{18} n·cm^{-2}

Table 9.5: *Units used to quantify radiation.*

Unit name	**SI units**	**Conventional units**	**Conversion Factor**
Activity	Becquerel (Bq)	Curie (Ci)	1 Bq = 2.7×10^{-11} Ci
Absorbed dose	Gray (Gy)	rad	1 Gy = 100 rad
Equivalent dose	Sievert (Sv)	rem	1 Sv = 100 rem

Thermal neutron attenuator foil

FLEX/BORON foil produced by Thermo company has been used as a thermal neutron attenuator. This is a flexible sheet material with a very high boron concentration (2.32×10^{22} boron atoms per cm^{3}). The sheets contain 25.3 % weight-percent boron (natural isotope distribution) uniformly distributed throughout a silicone elastomer sheet. The specification of the thermal neutron attenuator is presented in Table 9.4.

Units used to describe radiation

Many various units are used to quantify activity, dose, dose equivalent, and exposure. Despite, that the International System of units supply new units the conventional are still being used. The comparison of conventional and SI units used to quantify activity, absorbed and equivalent doses are presented in Table 9.5.

Publications with author's contribution

[1-A] B. Mukherjee, D. Makowski, and S. Simrock. Dosimetry of high energy electron linac produced photoneutrons and the bremsstrahlung gamma rays using TLD-500 and TLD-700 dosimeter pairs. *Nuclear Instruments and Methods in Physics Research Section A: Accelerators, Spectrometers, Detectors and Associated Equipment*, 545(3):830–841, 2005, ISSN 0168-9002.

[2-A] D. Makowski, M. Grecki, A. Napieralski, S. Simrock, and B. Mukherjee. A distributed system for radiation monitoring at linear accelerators. *IEEE Transactions on Nuclear Science (TNS)*, 53(4):2008–2015, 2006, ISSN: 0018-9499.

[3-A] A. Napieralski, M. Grecki, P. Sękalski, D. Makowski, M. Wójtowski, W. Cichalewski, B. Kosęda, and B. Świercz. Przegląd prac Politechniki Łódzkiej realizowanych w programie CARE. *Elektronika - Konstrukcje, Technologie, Zastosowania*, (2-3):78–79, 2005, ISSN 0033-2089.

[4-A] W. Giergusiewicz, W. Jałmużna, K. Poźniak, N. Ignashin, M. Grecki, D. Makowski, T. Jeżyński, K. Perkuszewski, K. Czuba, S. Simrock, and R. Romaniuk. Low Latency Control Board for LLRF System – SIMCON 3.1. *Proceedings of SPIE Vol. 5948, Photonics Applications in Industry and Research IV*, pages 710–715, 2005, ISBN 0-8194-5955-0.

[5-A] B. Mukherjee, D. Makowski, D. Rybka, M. Grecki, and S. Simrock. Interpretation of the Single Event Upset in Static Random Access Memory chips induced by low energy neutrons. *12th Mixed Design of Integrated Circuits and Systems, MIXDES*, pages 795–798, 2005, ISBN 83-919289-9-3.

[6-A] B. Mukherjee, D. Makowski, D. Rybka, O. Kroeplin, S. Simrock, and H. J. Eckoldt. External Radiation Shielding for the Protection of Electronic Devices Operating in the FLASH Facility Tunnel at DESY. *13th Mixed Design of Integrated Circuits and Systems, MIXDES*, pages 65–68, 2006, ISBN 83-922632-1-9.

[7-A] B. Świercz, D. Makowski, and A. Napieralski. Research of fault-tolerant computing using COTS elements. *2006 NSTI Nanotechnology Conference and Trade Show Nanotech 2006*, vol. 3, pages 94–97, 2006, ISBN 0-9767985-8-1.

[8-A] D. Makowski, B. Świercz, and A. Napieralski. A Novel Approach for Operating Systems Protection Against Single Event Upset. *13th Mixed Design of Integrated Circuits and Systems, MIXDES*, pages 61–64, 2006, ISBN 83-922632-1-9.

[9-A] B. Świercz and D. Makowski. Wpływ promieniowania neutronowego na pracę komputera PC. *Mikroelektronika i Informatyka, KTMiI P.L*, pages 203–210, wrzesien 2005, ISBN 83-922632-0-0.

[10-A] B. Świercz, D. Makowski, and A. Napieralski. The IAradSim — IA32 architecture under a high radiation environment simulator. *2005 NSTI Nanotechnology Conference and Trade Show Nanotech 2005*, pages 411–414, 2005, ISBN 0-9767985-2-2.

[11-A] B. Świercz, D. Makowski, and A. Napieralski. The sCore – operating system for research of fault-tolerant computing. *12^{th} Mixed Design of Integrated Circuits and Systems, MIXDES 2005*, pages 821–828, 2005, ISBN 83-919289-9-3.

[12-A] M. Wojtczak, D. Makowski, G. Jabłoński, M. Grecki, and S. Simrock. DSP-based system for advanced radiation tolerant algorithms evaluation. *Proceedings of SPIE Vol. 6159, Photonics Applications in Astronomy, Communications, Industry, and High-Energy Physics Experiments IV*, pages 139–146, 2005, ISBN 0-8194-6211-4.

[13-A] D. Makowski, M. Grecki, and G. Jabłoński. Application of a genetic algorithm to design of radiation tolerant programmable devices. *11^{th} Mixed Design of Integrated Circuits and Systems, MIXDES 2004*, pages 463–467, 2004, ISBN 83-919289-7-7.

[14-A] D. Makowski, B. Mukherjee, M. Grecki, and S. Simrock. SEE induced in SRAM operating in a superconducting electron linear accelerator environment. *Proceedings of SPIE Vol. 5775, Photonics Applications in Astronomy, Communications, Industry, and High-Energy Physics Experiments IV*, pages 95–102, 2004, ISBN 0-8194-5756-6.

[15-A] D. Makowski, M. Grecki, B. Mukherjee, S. Simrock, B. Świercz, and A. Napieralski. The application of SRAM chip as a novel neutron detector. *2005 NSTI Nanotechnology Conference and Trade Show Nanotech 2005*, pages 419–422, 2005, ISBN 0-9767985-2-2.

[16-A] D. Makowski, M. Grecki, B. Mukherjee, S. Simrock, B. Świercz, and A. Napieralski. SRAM-based passive dosimeter for accelerator environments. *7^{th} European Workshop on Diagnostics and Instrumentation for Particle ACcelerators, DIPAC2005*, June 2005.

[17-A] B. Mukherjee, D. Makowski, A. Kalicki, D. Rybka, M. Grecki, and S. Simrock. A neutron irradiation device for the testing of microelectronic components to be used in the radiation environment of high-energy particle accelerators at DESY. *12^{th} Mixed Design of Integrated Circuits and Systems, MIXDES*, pages 767–770, 2005, ISBN 83-919289-9-3.

[18-A] D. Makowski and A. Napieralski. Radiation monitoring system for X-FEL. *Special Issue of Measurement Science and Technology on Metrological aspects of Accelerator Technology and High Energy Physics Experiments*, December 2006, in print.

[19-A] D. Makowski, M. Grecki, B. Mukherjee, S. Simrock, B. Świercz, and A. Napieralski. The application of SRAM chip as a novel neutron detector. *Journal of Experimental Nanoscience*, 1(2), pages 261 – 268, June 2006, ISSN 1745-8080.

[20-A] D. Makowski, M. Grecki, B. Mukherjee, S. Simrock, and B. Świercz. Radiation tolerant system for neutron fluence measurement. *12th Mixed Design of Integrated Circuits and Systems, MIXDES*, pages 803–809, 2005, ISBN 83-919289-9-3.

[21-A] D. Makowski, M. Grecki, A. Napieralski, S. Simrock, and B. Mukherjee. A distributed system for radiation monitoring at linear accelerators. *RADiation and its Effects on Component and Systems RADECS*, page in print, September 2005.

[22-A] D. Makowski, G. Jabłoński, A. Napieralski, S. Simrock, B. Mukherjee and M. Grecki, . A readout for a cost-effective neutron fluence monitoring system. *RADiation and its Effects on Component and Systems RADECS*, page in print, September 2006.

[23-A] D. Makowski, M. Grecki, B. Mukherjee, B. Świercz, S. Simrock, and A. Napieralski. The Radiation Tolerant Readout System for SRAM-based Neutron Detector. *13th Mixed Design of Integrated Circuits and Systems, MIXDES*, pages 95–100, 2006, ISBN 83-922632-1-9.

[24-A] D. Makowski, G. Jabłoński, J. Mielczarek, A. Napieralski, and M. Grecki. FPGA–based Neutron Radiation Tolerant Microcontroller. *2006 NSTI Nanotechnology Conference and Trade Show Nanotech 2006*, vol. 3, pages 90–93, 2006, ISBN 0-9767985-8-1.

[25-A] D.Makowski, B.Świercz, and M.Grecki A.Napieralski. Projektowanie systemów niewrażliwych na wpływ promieniowania na potrzeby akceleratora X-FEL. *Elektronika - Konstrukcje, Technologie, Zastosowania*, (7):21–25, 2005, ISSN 0033-2089.

[26-A] D. Makowski, M. Grecki, B. Mukherjee, and S. Simrock. System do pomiaru neutronów. *Mikroelektronika i Informatyka, KMiTI P.Ł.*, pages 95–103, maj 2004, ISBN 83-919289-5-0.

[27-A] D. Makowski, B. Mukherjee, and A. Napieralski. An application of RadFET for ionizing radiation dosimetry. *Wilga 2006*, June 2006, in print.

[28-A] D. Makowski, S. Simrock, M. Grecki, B. Mukherjee, and A. Napieralski. Online gamma radiation and neutron fluence monitoring. *LLRF05: Workshop on Low Level RF, CERN*, pages 123–127, October 2005.

Bibliography

[1] R. Brinkmann, K. Flottmann, J. Rossbach, P. Schmuser, N. Walker, and H. Weise. Technical design report, PART II-The accelerator. *Deutsche Elektronen-Synchrotron DESY*, 2001.

[2] M. Altarelli at al. X-Ray Free Electron Laser - technical design report. Technical report, Deutsche Elektronen-Synchrotron, May 2006.

[3] A. Schwarz. The European X-Ray free electron laser project at DESY. *26^{th} International Free-Electron Laser Conference*, pages 85–89, August 2004.

[4] G. Materlik and Th. Tschentscher. Technical design report, PART V-The X-Ray Free Electron Laser. *Deutsche Elektronen-Synchrotron DESY*, 2001.

[5] A. Gamp. From the TESLA Test Facility to the VUV-FEL user facility. *12^{th} Mixed Design of Integrated Circuits and Systems MIXDES*, pages 789–793, June 2005.

[6] Deutsche Elektronen-Synchrotron. X-Ray Free Electron Laser Interim Report of the Scientific and Technical Issues (XFEL-STI) Working Group on a European XFEL Facility in Hamburg. Technical report, Deutsche Elektronen-Synchrotron, January 2005.

[7] F. Richard, J. Schneider, D. Trines, and A. Wagner. Technical design report, PART I-Executive summary. *Deutsche Elektronen-Synchrotron DESY*, 2001.

[8] R. Heuer, D. Miller, F. Richard, and P. Zerwas. Technical design report, PART III-Physics at an e+/e- linear collider. *Deutsche Elektronen-Synchrotron DESY*, 2001.

[9] G. Behnke, S. Bertolucci, R. Heuer, and R. Settles. Technical design report, PART IV-A detector for TESLA. *Deutsche Elektronen-Synchrotron DESY*, 2001.

[10] R. Klanner, V. Telnov, U. Katz, M. Klein, A. Levy, R. Kaiser, W. Nowak, E. De-Sanctis, J. Laget, and K. Rith. Technical design report, PART VI-Appendices. *Deutsche Elektronen-Synchrotron DESY*, 2001.

[11] W. Shi. SASE X-Ray Free Electron Laser in DESY. *Journal of the Society of Chinese Physists*, 6:5 –16, December 2000.

[12] R. Brinkmann. Accelerator Layout of the XFEL. *XXII International Linear Accelerator Conference*, 1:2–7, August 2004.

[13] S. Simrock. State of the art in RF control. *LINAC 2004 - Proceedings, Germany*, August 2004.

[14] T. Schilcher. *Vector Sum Control of Pulsed Accelerating Fields in Lorents Force Detuned Superconducting Cavities*. PhD thesis, University of Hamburg, 2000.

[15] R.J. Sheu, J.P.Wang, C.R. Chen, J. Liu, F.D. Chang, and S.H. Jiang. Network-based real-time radiation monitoring system in Synchrotron Radiation Research Center. *Health Phys.*, 2003.

[16] J.D. Cossairt. *Radiation Physics for Personnel and Environmental Protection*. Fermi-National Accelerator Laboratory, 2001.

[17] A. Fasso, M. Silari, and L. Ulrici. Predicting induced radioactivity at high-energy electron accelerators. *9^{th} International Conference on Radiation Shielding*, 1999.

[18] M. Pisharody, E. Semones, and P.K. Job. Dose Measurement of Bremsstrahlung-Produced Neutrons at the Advanced Photon Source. Technical report, Argonne National Laboratory, Experimental Facilities Division Advanced Photon Source, August 1998.

[19] G. Barbottin and A. Vapaille. *Instabilities in Silicon Devices, New Insulators, Devices and Radiation Effects*. Elsevier, 1999.

[20] A. Jorio, A. Zounoubi, Z. Elachheb, C. Carlone, and S. M. Khann. Displacement damages created by γ particles radiation in n type GaAs. *M. J. of Condensed Matter*, 2(1), 1999.

[21] G. Messenger and M. Ash. *The Effects of Radiation on Electronic Systems*. Van Nostrand Reinhold Company Inc., 1986.

[22] L. Adams A. Holmes-Siedle. *Handbook of Radiation Effects*. Oxford University Press, 2004.

[23] F. Giustino. *Radiation Effects on Semiconductor Devices, Study of the Enhanced Low Dose Rate Degradation*. PhD thesis, Politechnico di Torino, 2001.

[24] R.A.B. Devine. The structure of SiO_2, its defects and radiation hardness. *IEEE Transactions on Nuclear Science*, 41(3):452–459, 1994.

[25] F. Wrobel. Fundamentals of Radiation-Mater interaction. *New Challenges for Radiation Tolerance Assessment, RADECS 2005*, pages 5–31, 2005.

[26] D. M. Fleetwood. Emerging issues for total ionizing dose effects on microelectronics. *New Challenges for Radiation Tolerance Assessment, RADECS 2005*, pages 33–46, 2005.

[27] C.E. Barnes, D.M. Fleetwood, D.C. Shaw, and P.S. Winokur. Post irradiation effects (PIE) in integrated circuits. *IEEE Transactions on Nuclear Science*, 39(3):328–341, 1992.

[28] H.L. Hughes and J.M. Benedetto. Radiation effects and hardening of MOS technology: devices and circuits. *IEEE Transactions on Nuclear Science*, 50(3):500–521, 2003.

[29] O. Calvo, M. Gonzalez, C. Romero, E. Garcia-Moreno, E. Isern, M. Roca, and J. Segura. Integrated CMOS linear dosimeters. In *Integrated Circuit Design, 1998. Proceedings. XI Brazilian Symposium on*, pages 78–81, 1998.

[30] T.R. Oldham and F.B. McLean. Total ionizing dose effects in MOS oxides and devices. *IEEE Transactions on Nuclear Science*, 50(3):483–499, 2003.

[31] A. Paccagnell, A. Candelori, A. Milani, E. Formigoni, G. Ghidini, F. Pellizzer, D. Drera, P.G. Fuochi, and M. Lavale. Breakdown properties of irradiated MOS capacitors. *IEEE Transactions on Nuclear Science*, 43(6):2609–2616, 1996.

[32] M. Da Rold, A. Paccagnella, A. Da Re, G. Verzellesi, N. Bacchetta, R. Wheadon, G.-F. Dalla Betta, A. Candelori, G. Soncini, and D. Bisello. Radiation effects on breakdown characteristics of multiguarded devices. *IEEE Transactions on Nuclear Science*, 44(3):721–727, 1997.

[33] T.L. Meisenheimer and D.M. Fleetwood. Effect of radiation-induced charge on 1/f noise in MOS devices. *IEEE Transactions on Nuclear Science*, 37(6):1696–1702, 1990.

[34] Z. Li. Experimental comparisons among various models for the reverse annealing of the effective concentration of ionized space charges (neff) of neutron irradiated silicon detectors. *IEEE Transactions on Nuclear Science*, 42(4):224–234, 1995.

[35] Z. Li, W. Chen, L. Dou, V. Eremin, H.W. Kraner, C.J. Li, G. Lindstroem, and E. Spiriti. Study of the long term stability of the effective concentration of ionized space charges (neff) of neutron irradiated silicon detectors fabricated by various thermal oxidation processes. *IEEE Transactions on Nuclear Science*, 42(4):219–223, 1995.

[36] O. Gilard and G. Quadri. Radiation effects on electronics: displacement damages. *New Challenges for Radiation Tolerance Assessment, RADECS 2005*, pages 47–69, 2005.

[37] R.D. Schrimpf. Recent advances in understanding total-dose effects in bipolar transistors. In *Radiation and its Effects on Components and Systems, 1995. RADECS 95., Third European Conference on*, pages 9–18, 1995.

[38] K. Makino, M. Berz, D. Errede, and C.J. Johnstone. Nonlinear transfer map treatment of beams through systems with absorbing material. In *Physics and Control, 2003. Proceedings. 2003 International Conference*, volume 3, 2003.

[39] A.A. Hahn and J.R. Zagel. Observation of Bethe-bloch ionization using the booster ion profile monitor. In *Particle Accelerator Conference, 1999. Proceedings of the 1999*, volume 1, pages 468–470, 1999.

[40] C. Detcheverry, C. Dachs, E. Lorfevre, C. Sudre, G. Bruguier, J.M. Palau, J. Gasiot, and R. Ecoffet. SEU critical charge and sensitive area in a submicron CMOS technology. *IEEE Transactions on Nuclear Science*, 44(6):2266–2273, 1997.

[41] K. Label and L. Cohn. Radiation testing and evaluation issues for modern integrated circuits. *New Challenges for Radiation Tolerance Assessment, RADECS 2005*, pages 71–93, 2005.

[42] Actel. Effects of neutrons on programmable logic. *White Paper*, December 2002.

[43] A.V. Sannikov. Single event upsets in semiconductor devices induced by highly ionizing particles. *Radiation Protection Dosimetry*, 110(1–4):399–403, 2004.

[44] R. B. Katz. Single event upset (SEU). *Technical Report, 2005*, 2005.

[45] A. Candelori. Radiation effects on detectors and electronic devices and systems (part II). *Istituto Nazionale di Fisica Nucleare and Dipartimento di Fisica*, 2003.

[46] D.N. Nguyen and L.Z. Scheick. SEE and TID of emerging non-volatile memories. In *Radiation Effects Data Workshop, 2002 IEEE*, pages 62–66, 2002.

[47] F.Faccio. COTS for the LHC radiation environment: the rules of the game. *6^{th} Workshop on Electronics for LHC Experiments, 2000*, 2000.

[48] E. Mikkola, B. Vermeire, H.J. Barnaby, H.G. Parks, and K. Borhani. SET tolerant CMOS comparator. *IEEE Transactions on Nuclear Science*, 51(6):3609–3614, 2004.

[49] Y. Boulghassoul, J.D. Rowe, and L.W. Massengill. Applicability of circuit macromodeling to analog single-event transient analysis. *IEEE Transactions on Nuclear Science*, 50(6):2119–2125, 2003.

[50] J.M. Benedetto, P.H. Eaton, D.G. Mavis, M. Gadlage, and T. Turflinger. Variation of Digital SET Pulse Widths and the Implications for Single Event Hardening of Advanced CMOS Processes. *IEEE Transactions on Nuclear Science*, 52(6):2114–2119, 2005.

[51] Y. Boulghassoul, L.W. Massengill, A.L. Sternberg, and B.L. Bhuva. Effects of Technology Scaling on the SET Sensitivity of RF CMOS Voltage-controlled Oscillators. *IEEE Transactions on Nuclear Science*, 52(6):2426–2432, 2005.

[52] P. Mongkolkachit and B. Bhuva. Design technique for mitigation of alpha-particle-induced single-event transients in combinational logic. *IEEE Transaction on Device and Materials Reliability*, 3(3):89–92, 2003.

[53] S.D. LaLumondiere, R. Koga, P. Yu, M.C. Maher, and S.C. Moss. Laser-induced and heavy ion-induced single-event transient (SET) sensitivity measurements on 139-type comparators. *IEEE Transactions on Nuclear Science*, 49(6):3121–3128, 2002.

[54] A.S. Sedra and K.C. Smith. *Microelectronics Circuits*. Oxford University Press, 1998.

[55] G. Bruguier and J.-M. Palau. Single particle-induced latchup. *IEEE Transactions on Nuclear Science*, 43(2):522–532, 1996.

[56] J.L. Titus and C.F. Wheatley. Experimental studies of single-event gate rupture and burnout in vertical power MOSFETs. *IEEE Transactions on Nuclear Science*, 43(2):533–545, 1996.

[57] J.R. Brews, M. Allenspach, R.D. Schrimpf, K.F. Galloway, J.L. Titus, and C.F. Wheatley. A conceptual model of a single-event gate-rupture in power MOSFETs. *IEEE Transactions on Nuclear Science*, 40(6):1959–1966, 1993.

[58] J.L. Titus, C.F. Wheatley, K.M. Van Tyne, J.F. Krieg, D.I. Burton, and A.B. Campbell. Effect of ion energy upon dielectric breakdown of the capacitor response in vertical power MOSFETs. *IEEE Transactions on Nuclear Science*, 45(6):2492–2499, 1998.

[59] M.N. Darwish, M.A. Shibib, M.R. Pinto, and J.L. Titus. Single event gate rupture of power DMOS transistors. In *Electron Devices Meeting, 1993. Technical Digest., International*, pages 671–674, 1993.

[60] R. Koga and W.A. Kolasinski. Heavy ion induced snapback in CMOS devices. *IEEE Transactions on Nuclear Science*, 36(6):2367–2374, 1989.

[61] Y. Fong and C. Hu. High-current snapback characteristics of MOSFETs. *"IEEE Trans. Electron Devices"*, 37(9):2101–2103, 1990.

[62] A.H. Johnston. Scaling and Technology Issues for Soft Error Rates. 4^{th} *annual Research Coference on Reliability*, pages 152–157, 2000.

[63] R.C. Lacoe, J.V. Osborn, D.C. Mayer, S. Brown, and D.R. Hunt. Total-dose radiation tolerance of a commercial 0.35 μm CMOS process. In *Radiation Effects Data Workshop, 1998. IEEE*, pages 104–110, 1998.

[64] M. Manghisoni, L. Ratti, V. Re, V. Speziali, G. Traversi, and A. Candelori. Comparison of ionizing radiation effects in 0.18 and 0.25 μm CMOS technologies for analog applications. *IEEE Transactions on Nuclear Science*, 50(6):1827–1833, 2003.

[65] K. Chakraborty and P. Mazumder. *Fault-Tolerance and Reliability Techniques for High-density Random Access Memories*. Prentice Hall, 2002.

[66] G. Anelli. Trends in CMOS technologies and radiation tolerant design. In *Nuclear Science Symposium Conference Record, 2000 IEEE*, volume 1, 2000.

[67] A.H. Johnston, G.M. Swift, and B.G. Rax. Total dose effects in conventional bipolar transistors and linear integrated circuits. *IEEE Transactions on Nuclear Science*, 41(6):2427–2436, 1994.

[68] J.R. Schwank, V. Ferlet-Cavrois, M.R. Shaneyfelt, P. Paillet, and P.E. Dodd. Radiation effects in SOI technologies. *IEEE Transactions on Nuclear Science*, 50(3):522–538, 2003.

[69] A. Scarpa, A. Paccagnella, F. Montera, G. Ghibaudo, G. Pananakakis, G. Ghidini, and P.G. Fuochi. Ionizing radiation induced leakage current on ultra-thin gate oxides. *IEEE Transactions on Nuclear Science*, 44(6):1818–1825, 1997.

[70] D. Bisello, A. Candelori, A. Kaminski, D. Pantano, R. Rando, J. Wyss, A. Andrighetto, and V. Cindro. Neutron irradiation effects on standard and oxygenated silicon diodes. *IEEE Transactions on Nuclear Science*, 49(3):1027–1034, 2002.

[71] A. H. Johnston. Radiation effects in advanced microelectronics technologies. In *Radiation and Its Effects on Components and Systems RADECS 97*, pages 1–16, 1998.

[72] H.F. Benz, J.W. Gambles, S.R. Whitaker, K.J. Hass, G.K. Maki, and Pen-Shu Yeh. Low power radiation tolerant VLSI for advanced spacecraft. In *Aerospace Conference Proceedings, 2002. IEEE*, volume 5, pages 5–2401, 2002.

[73] J.W. Gambles, K.J. Hass, and S.R. Whitaker. Radiation Hardness of Ultra Low Power CMOS VLSI. *11^{th} NASA Symposium on VLSI Design, USA, 2003*, 2003.

[74] L. Miles, J. Gambles, G. Maki, W. Ryan, and S. Whitaker. A 1 Gb/s Low-Density Parity-Check Encoder. *12^{th} NASA Symposium on VLSI Design, USA*, 2005.

[75] H. Hatano. Radiation hardened high performance CMOS VLSI circuit designs. *Circuits, Devices and Systems, IEEE Proceedings*, 139(3):287–294, 1992.

[76] R. Szczygieł. *Projektowanie bloków cyfrowych układów ASIC do odczytu detektorów pozycyjnych eksperymentu ATLAS pod kątem odporności radiacyjnej*. PhD thesis, Instytut Fizyki Jądrowej im. Henryka Niewodniczańskiego Polskiej Akademii Nauk, 2006.

[77] O. Musseau. Single-Event Effects in SOI Technologies and Devices. *IEEE Transactions on Nuclear Science*, 43(2):603–613, 1996.

[78] G. M. Anelli. *Conception et caracterisation de circuits integres resistants aux radiations pour les detecteurs de particules du LHC en technologies CMOS submicroniques profondes*. PhD thesis, Institut National Polytechnique de Grenoble, 2000.

[79] F. Faccio, K. Kloukinas, A. Marchioro, T. Calin, J. Cosculluela, M. Nicolaidis, and R. Velazco. Single event effects in static and dynamic registers in a 0.25 μm CMOS technology. *IEEE Transactions on Nuclear Science*, 46(6):1434–1439, 1999.

[80] S.E. Kerns, L.W. Massengill, D.V. Jr. Kerns, M.L. Alles, T.W. Houston, H. Lu, and L.R. Hite. Model for CMOS/SOI single-event vulnerability. *IEEE Transactions on Nuclear Science*, 36(6):2305–2310, 1989.

[81] Quming Zhou and K. Mohanram. Transistor sizing for radiation hardening. In *Reliability Physics Symposium Proceedings, 2004. 42nd Annual. 2004 IEEE International*, pages 310–315, 2004.

[82] Quming Zhou and K. Mohanram. Gate sizing to radiation harden combinational logic. *"IEEE Trans. Computer-Aided Design"*, 25(1):155–166, 2006.

[83] K. Mohanram and N.A. Touba. Partial error masking to reduce soft error failure rate in logic circuits. In *Defect and Fault Tolerance in VLSI Systems, 2003. Proceedings. 18^{th} IEEE International Symposium on*, pages 433–440, 2003.

[84] K. Mohanram and N.A. Touba. Cost-effective approach for reducing soft error failure rate in logic circuits. In *Test Conference, 2003. Proceedings. ITC 2003. International*, volume 1, pages 893–901, 2003.

[85] K. Mohanram, E.S. Sogomonyan, M. Gossel, and N.A. Touba. Synthesis of low-cost parity-based partially self-checking circuits. In *On-Line Testing Symposium, 2003. IOLTS 2003. 9th IEEE*, pages 35–40, 2003.

[86] J. Spann, V. Kushner, T.J. Thornton, J. Yang, A. Balijepalli, H.J. Barnaby, X.J. Chen, D. Alexander, W.T. Kemp, S.J. Sampson, and M.E. Wood. Total Dose Radiation Response of CMOS Compatible SOI MESFETs. *IEEE Transactions on Nuclear Science*, 52(6):2398–2402, 2005.

[87] G. Gasiot, V. Ferlet-Cavrois, P. Roche, P. Flatresse, C. D'Hose, O. Musseau, and J. du Port de Poncharra. Comparison of the sensitivity to heavy ions of 0.25 μm bulk and SOI technologies. In *Radiation and Its Effects on Components and Systems, 2001. 6th European Conference on*, pages 211–216, 2001.

[88] H. Kaakani. Radiation hardened memory development at Honeywell. In *Aerospace Conference, 2001, IEEE Proceedings.*, volume 5, pages 2273–2279, 2001.

[89] Bing Zhao and A. Leuciuc. Single event transients characterization in SOI CMOS comparators. *IEEE Transactions on Nuclear Science*, 51(6):3360–3364, 2004.

[90] M. Alles, B. Dolan, H. Hughes, P. McMarr, P. Gouker, and M. Liu. Evaluating manufacturability of radiation-hardened SOI substrates. In *SOI Conference, 2001 IEEE International*, pages 131–132, 2001.

[91] K. Hirose, H. Saito, Y. Kuroda, S. Ishii, Y. Fukuoka, and D. Takahashi. SEU resistance in advanced SOI-SRAMs fabricated by commercial technology using a rad-hard circuit design. *IEEE Transactions on Nuclear Science*, 49(6):2965–2968, 2002.

[92] B. Jun, D.M. Fleetwood, R.D. Schrimpf, X. Zhou, E.J. Montes, and S. Cristoloveanu. Charge separation techniques for irradiated pseudo-MOS SOI transistors. *IEEE Transactions on Nuclear Science*, 50(6):1891–1895, 2003.

[93] S. Parke. Comparison of existing and proposed SOI MOSFET device structures for minimizing total dose radiation damage. In *Aerospace Conference, 2004. Proceedings. 2004 IEEE*, volume 4, pages 2427–2430, 2004.

[94] J.R. Ffarmasank, P.E. Dodd, M.R. Shaneyfelt, G. Vizkelethy, B.L. Draper, T.A. Hill, D.S. Walsh, G.L. Hash, B.L. Doyle, and F.D. McDaniel. Charge collection in SOI capacitors and circuits and its effect on SEU hardness. *IEEE Transactions on Nuclear Science*, 49(6):2937–2947, 2002.

[95] T.P. Ma and P. V. Dressendorfer. *Ionizing radiation effects in MOS devices and circuits*. Wiley, 1989.

[96] F. Lima. Single event upset mitigation techniques for programmable devices. Technical report, Federal University of Rio Grande do Sul, December 2000.

[97] F. Lima. *Designing Single Event Upset Mitigation Techniques for Large SRAM-based FPGA Devices*. PhD thesis, Federal University of Rio Grande do Sul, February 2002.

[98] M.N. Liu and S. Whitaker. Low power SEU immune CMOS memory circuits. *IEEE Transactions on Nuclear Science*, 39(6):1679–1684, 1992.

[99] D. Wiseman, J. Canaris, S. Whitaker, J. Venbrux, K. Cameron, K. Arave, L. Arave, M.N. Liu, and K. Liu. Design and Testing of SEU/ SEL Immune Memory and Logic Circuits in a Commercial CMOS Process. In *Radiation Effects Data Workshop, 1993., IEEE*, pages 51–55, 1993.

[100] R. Velazco, D. Bessot, S. Duzellier, R. Ecoffet, and R. Koga. Two CMOS memory cells suitable for the design of SEU-tolerant VLSI circuits. *IEEE Transactions on Nuclear Science*, 41(6):2229–2234, 1994.

[101] W. Heidergott. SEU tolerant device, circuit and processor design. In *Design Automation Conference, 2005. Proceedings. 42nd*, pages 5–10, 2005.

[102] B. Nicolescu and R. Velazco. Detecting soft errors by a purely software approach: method, tools and experimental results. In *Design, Automation and Test in Europe Conference and Exhibition, 2003*, pages 57–62, 2003.

[103] P.P. Shirvani and E.J. McCluskey. Fault-tolerant Systems in a Space Environment the CRC AGROS Project. Technical report, Stanford University, 1998.

[104] P.P. Shirvani, N.R. Saxena, and E.J. McCluskey. Software-implemented EDAC protection against SEUs. *IEEE Transactions on Reliability*, 49(3):273–284, 2000.

[105] P.K. Samudrala, J. Ramos, and S. Katkoori. Selective Triple Modular Redundancy (STMR) based single-event upset (SEU) tolerant synthesis for FPGAs. *IEEE Transactions on Nuclear Science*, 51(5):2957–2969, 2004.

[106] R. Katz, R. Barto, P. McKerracher, B. Carkhuff, and R. Koga. SEU hardening of field programmable gate arrays (FPGAs) for space applications and device characterization. *IEEE Transactions on Nuclear Science*, 41(6):2179–2186, 1994.

[107] P. Brinkley, A. Carmichael, and C. Carmichael. SEU mitigation design techniques for the XQR4000XL. Technical report, Xilinx, 2000.

[108] Yanmei Li, Dongmei Li, and Zhihua Wang. A new approach to detect-mitigate-correct radiation-induced faults for SRAM-based FPGAs in aerospace application. In *National Aerospace and Electronics Conference, 2000. NAECON 2000. Proceedings of the IEEE 2000*, pages 588–594, 2000.

[109] S. Bharthipudi. *Comparison of Numerical result checking mechanisms for FFT Computations under faults*. PhD thesis, Georgia Institute of Technology, 2003.

[110] C. Carmichael. Triple module redundancy design techniques for Virtex FPGAs. Technical report, Xilinx, 2001.

[111] F. Lima, L. Carro, and R. Reis. Designing fault tolerant systems into SRAM-based FPGAs. *Proc. ACM/IEEE Design Automation Conf, 2003*, pages 650–655, 2003.

[112] J.R. Jr. Samson, L. DeLa Torre, P. Wiley, T. Stottlar, and J. Ring. A comparison of algorithm-based fault tolerance and traditional redundant self-checking for SEU mitigation. In *Digital Avionics Systems, 2001. DASC. The 20th Conference*, volume 2, pages 1–8, 2001.

[113] A. Tiwari and K.A. Tomko. Enhanced reliability of finite-state machines in FPGA through efficient fault detection and correction. *IEEE Transactions on Reliability*, 54(3):459–467, 2005.

[114] P. Penfield. Information and entropy. Technical report, Massachusetts Institute of Technology, 2004.

[115] R. H. Morelos-Zaragoza. *The Art of Error Correcting and Coding*. Wiley, 2002.

[116] M.L. Shooman. *Reliability of Computer Systems and Networks: Fault Tolerance, Analysis, and Design*. John Wiley and Sons, Inc., 2003.

[117] M. Purser. *Introduction to error-correcting codes*. Artech House, 1995.

[118] C. Carmichael. Correcting Single-Event Upsets Through Virtex Partial Configuration. Technical report, Xilinx, 2000.

[119] J. Mielczarek. Design of Radiation Tolerant Transmission Channel Circuit. Master's thesis, M.Sc. thesis, Technical University of Łódź, 2005.

[120] S. Petrizzelli. Appunti di Elettronica Digitale Circuiti per il codice Hamming. *Appunti di Elettronica Digitale*, pages 1–6, 1993.

[121] F.G. de Lima, E. Cota, L. Carro, M. Lubaszewski, R. Reis, R. Velazco, and S. Rezgui. Designing a radiation hardened 8051-like micro-controller. In *Integrated Circuits and Systems Design, 2000. Proceedings. 13th Symposium on*, pages 255–260, 2000.

[122] F. Lima, L. Carro, R. Velazco, and R. Reis. Injecting multiple upsets in a SEU tolerant 8051 micro-controller. In *On-Line Testing Workshop, 2002. Proceedings of the Eighth IEEE International*, 2002.

[123] M. Wojtczak. DSP-based System for Advanced Radiation Tolerant Algorithms Evaluation. Master's thesis, M.Sc. thesis, Technical University of Łódź, 2005.

[124] L. Schiano, M. Ottavi, F. Lombardi, S. Pontarelli, and A. Salsano. On the analysis of Reed Solomon coding for resilience to transient/permanent faults in highly reliable memories. In *Design, Automation and Test in Europe, 2005. Proceedings*, pages 580–585, 2005.

[125] S. Tam. Multiple Bit Error Correction. Technical report, Xilinx, 2004.

[126] R.J. McEliece. *The Theory of Information Coding*. Cambridge University Press, 2002.

[127] A.M. Saleh, J.J. Serrano, and J.H. Patel. Reliability of scrubbing recovery-techniques for memory systems. *IEEE Transactions on Reliability*, 39(1):114–122, 1990.

[128] G. C. Yang. Reliability of semiconductor RAMs with soft-error scrubbing techniques. In *Design, Automation and Test in Europe, 2005. Proceedings*, volume 142, pages 337–344, 1995.

[129] D. Yu-Lam, J. Lan, L. McMurchie, and C. Sechen. SEE-hardened-by-design area-efficient SRAMs. In *Aerospace, 2005 IEEE Conference*, pages 1–7, 2005.

[130] A. Benso, S. Di Carlo, G. Di Natale, and P. Prinetto. A watchdog processor to detect data and control flow errors. In *On-Line Testing Symposium, 2003. IOLTS 2003. 9th IEEE*, pages 144–148, 2003.

[131] Chung-Yu Liu. A study of flight-critical computer system recovery from space radiation-induced error. In *Digital Avionics Systems, 2001. DASC. The 20th Conference*, volume 1, pages 1–1, 2001.

[132] H.N. Becker, T.F. Miyahira, and A.H. Johnston. Latent damage in CMOS devices from single-event latchup. *IEEE Transactions on Nuclear Science*, 49(6):3009–3015, 2002.

[133] J.J. Wang, R.B. Katz, J.S. Sun, B.E. Cronquist, J.L. McCollum, T.M. Speers, and W.C. Plants. SRAM-based re-programmable FPGA for space applications. *IEEE Transactions on Nuclear Science*, 46(6):1728–1735, 1999.

[134] M. Stettler, M. Caffrey, P.Graham, and J. Krone. Radiation effects and mitigation strategies for modern FPGAs. *10th Workshop on Electronics for LHC and future Experiments*, pages 650–655, 2004.

[135] L. Sterpone and M. Violante. Analysis of the robustness of the TMR architecture in SRAM-based FPGAs. *IEEE Transactions on Nuclear Science*, 52(5):1545–1549, 2005.

[136] L. Jones. Single Event Upset (SEU) Detection and Correction Using Virtex-4 Devices. Technical report, Xilinx, 2006.

[137] Altera. Error Detection and Recovery Using CRC in Altera FPGA Devices. Technical report, Altera, 2006.

[138] J. Lohn, G. Larchev, and R. DeMara. Evolutionary fault recovery in a Virtex FPGA using a representation that incorporates routing. *International Parallel and Distributed Processing Symposium (IPDPS'03)*, April 2003.

[139] S. Vigander. Evolutionary fault repair of electronics in space applications. Master's thesis, University of Sussex, February 2001.

[140] R.O. Canham and A.M. Tyrrell. Evolved fault tolerance in evolvable hardware. In *Evolutionary Computation, 2002. CEC '02. Proceedings of the 2002 Congress on*, volume 2, pages 1267–1271, 2002.

[141] R. F. DeMara, J. D. Lohn, and G. Larchev. A genetic representation for evolutionary fault recovery in FPGAs, NASA Ames Research Center.

[142] H. E. Johns and J. R. Cunningham. *The Physics of Radiology*. Charles C Thomas Pub Ltd, 1983.

[143] A.B. Rosenfeld, M.I. Reinhard, D. Marinaro, P. Ihnat, G. Taylor, L. Peak, N. Freeman, D. Alexiev, and M. Lerch. A system for radiation damage monitoring. *IEEE Transactions on Nuclear Science*, 46(6):1766–1773, 1999.

[144] T.E. Mason. Neutron detectors for materials research. Technical report, OAK Ridge National Laboratory, 2000.

[145] W. Beezhold, D.E. Beutler, J.C. Garth, and P.J. Griffin. A review of the 40-year history of the NSREC's dosimetry and facilities session (1963-2003). *IEEE Transactions on Nuclear Science*, 50(3):635–652, 2003.

[146] K.K. Aglincew. *Dozymetria promieniowania jonizującego*. PWN, 1961.

[147] R.G. Jaeger. *Dozymetria i ochrona przed promieniowaniem*. PWN, 1962.

[148] P.D. Bradley. *The development of a Novel Silicon Microdosimeter for LET Radiation Therapy*. PhD thesis, University of Wollongong, 2000.

[149] A.F. Fernandez, B. Brichard, H. Ooms, R. Van Nieuwenhove, and F. Berghmans. Gamma dosimetry using red 4034 Harwell dosimeters in mixed fission neutrons and gamma environments. *IEEE Transactions on Nuclear Science*, 52(2):505–509, 2005.

[150] A.J. Peurrung. Recent developments in neutron detection. *Nuclear Instruments and Methods in Physics Research A*, 443(2-3):400–415, 2000.

[151] M. Miglierini. Detectors of radiation. In *Course on Reactor Physics Experiments*, pages 1–14, 2004.

[152] J.G. Webster. *Measurement, Instrumentation, and Sensors Handbook*. CRC Press LLC, 1999.

[153] E.B. Podgorska. *Radiation Oncology Physics: A Handbook for Teachers and Students*. International Atomic Energy Agency, 2005.

[154] M. Magheb. Gamma and X-rays detection. *Nuclear, Plasma and Radiological Engineering*, 2006.

[155] T. Ranger. Radiation detectors in nuclear medicine. *Imaging and Therapeutic Technology*, 19:481–502, 1999.

[156] Photonis. Fundamentals of neutron and gamma detectors. Technical report, Photonis, 1998.

[157] C. Wernli. External dosimetry: operational quantities and their measurement. *11^{th} International Congress of the International Radiation Protection Association (IRPA)*, pages 2–17, 2004.

[158] Centronic. BF_3 proportional counters. Technical Report 311/01-issue 3, Centronic Radiation Detectors, 2002.

[159] G. Fehrenbacher, F. Gutermuth, and T. Radon. Active neutron dose meters for the application at high energy particle accelerators. *GSI Scientific Report*, 1(1):221–222, 2003.

[160] Berthold. Wide energy neutron detector. Technical report, Berthold technologies, 2002.

[161] T. Nakamura. Recent development of advanced neutron detection technology. *Journal of Nuclear and Radiochemical Sciences*, 4(2):R15–R24, 2003.

[162] J.Barthe. Electronic dosimeters based on solid state detectors. *Nuclear Instruments and Methods in Physics Research B*, 184(3), May 2001.

[163] R.A. Price, C. Benson, M.J. Joyce, D.J. Kestell, and J. Silvie. Novel developments in the MOSFET dosimeter for neutron dosimetry applications. *Radiation Protection Dosimetry*, 110(1–4):283–290, 2004.

[164] F. Errico, M. Luszik-Bhadra, and T. Lahaye. State of the art of electronic personal dosimeters for neutrons. *Nuclear Instruments and Methods in Physics Research A*, pages 411–414, 2003.

[165] F. Errico, G. Curzio, R. Ciolini, A. Del Gratta, and R. Nath. A neutron dosemeter for nuclear criticality accidents. *GSI Scientific Report*, 110(1–4):487–490, 2004.

[166] M.A. Oliver. PIN diode and neutron spectrum measurements at the Army Pulse Radiation Facility. *IEEE Transactions on Nuclear Science*, 41(6):2132–2138, 1994.

[167] D.R. Roth, R.H. Maurer, J.D. Kinnison, P.J. McNulty, and M.W. Savage. Charged particle and neutron solid state detectors comparison. In *Nuclear Science Symposium, 1998. Conference Record. 1998 IEEE*, volume 1, pages 694–697, 1998.

[168] C.H. Mesquita, T.M. Filho, and M.M. Hamada. Development of neutron detector using the PIN photodiode with polyethylene (n,p) converter. *IEEE Transactions on Nuclear Science*, 50(4):1170–1174, 2003.

[169] B. Barelaud, F. Nexon-Mokhtari, C. Barrau, J.L Decossas, J.C. Vareille, and G.J. Sarrabayrouse. Study of an integrated electronic monitor for neutron fields. *Radiation Protection Dosimetry*, 61(1):153–158, 1995.

[170] J. Morin, J.C. Arnoud, J. David, and P. Zyromski. Measuring 1 MeV(Si) equivalent neutron fluences with PIN silicon diodes. In *Radiation and its Effects on Components and Systems, 1993.,RADECS 93., Second European Conference on*, pages 20–26, 1993.

[171] M. Tavlet and M.E. Leon Florian. Dose and neutron-fluence measurements in mixed gamma-neutron fields by means of semi-conductor dosimeters. In *Radiation and its Effects on Components and Systems, 1993.,RADECS 93., Second European Conference on*, pages 27–32, 1993.

[172] A.B. Rosenfeld, M. Yudelev, M.L.F. Lerch, I. Cornelius, P. Griffin, V.L. Perevertailo, I.E. Anokhin, O.S. Zinets, V.I. Khivrich, M. Pinkovskaya, D. Alexiev, and M. Reinhard. Neutron dosimetry with planar silicon P-I-N diodes. *IEEE Transactions on Nuclear Science*, 50(6):2367–2372, 2003.

[173] A. Rosenfeld, V. Khivrich, V. Kuts, M. Tavlet, L. Malfante, and C. Munoz-Ferrada. Use of Ukrainian semiconductor dosimeters in a CERN particle accelerator field. *IEEE Transactions on Nuclear Science*, 41(4):1009–1013, 1994.

[174] M.G. Buehler, B.R. Blaes, G.A. Soli, N. Zamani, and K.A. Hicks. Dose Measurement of Bremsstrahlung-Produced Neutrons at the Advanced Photon Source. Technical report, Jet Propulsion Laboratory, California Institute of Technology, October 1992.

[175] G. Soli, B. Blaes, M. Buehler, P. Jones, J.M. Ratliff, and H. Garrett. Clementine dosimetry. *JOURNAL OF SPACECRAFT AND ROCKETS 1995*, 32(6):1065–1070, 1995.

[176] Y.H. Shin, K.W. Min, J.G. Rhee, D.H. Lee, S.H. Kim, H.S. Kim, S.D. Park, D.K. Sung, and S.D. Choi. Analysis of anomalous TDE data on-board the KITSAT-1. *IEEE Transactions on Nuclear Science*, 46(6):1586–1594, 1999.

[177] R.L. Pease, M. Simons, and P. Marshall. Comparison of pMOSFET total dose response for Co-60 gammas and high-energy protons. *IEEE Transactions on Nuclear Science*, 48(3):908–912, 2001.

[178] W. Hajdas, J. Bialkowski, U. Wyser, L. Adams, A. Mohammadazdeh, R. Nickson, and B. O'Connell. Sensitivity of the SREM RADFET dosimeters for STRV-1c to various proton and gamma radiation environments. In *Radiation and Its Effects on Components and Systems, 1999. RADECS 99. 1999 Fifth European Conference on*, pages 110–113, 1999.

[179] A. Haran and A. Jaksic. The role of fixed and switching traps in long-term fading of implanted and unimplanted gate oxide RADFETs. *IEEE Transactions on Nuclear Science*, 52(6):2570–2577, 2005.

[180] A. Haran, A. Jaksic, N. Refaeli, A. Eliyahu, D. David, and J. Barak. Temperature effects and long term fading of implanted and unimplanted gate oxide RADFETs. *IEEE Transactions on Nuclear Science*, 51(5):2917–2921, 2004.

[181] F. Ravotti, M. Glaser, M. Moll, Ch. Ilgner, B. Camanzi, and A.G. Holmes-Siedle. Response of RadFET Dosimeters to high Fluences of fast Neutrons. *IEEE Transactions on Nuclear Science*, 52(4):959–965, 2005.

[182] A.B. Rosenfeld, M.C. Carolan, G.I. Kaplan, B.J. Allen, and V.I. Khivrich. MOSFET dosimeters: the role of encapsulation on dosimetric characteristics in mixed gamma-neutron and megavoltage X-ray fields. *IEEE Transactions on Nuclear Science*, 42(6):1870–1877, 1995.

[183] L.Z. Scheick and G.M. Swift. Dose and microdose measurement based on threshold shifts in MOSFET arrays in commercial SRAMs. *IEEE Transactions on Nuclear Science*, 49(6):2810–2817, 2002.

[184] T.H. Hau H.P. Chou, T.C. Chou. Evaluation of high density DRAMs as a nuclear radiation detector. *Applied Radiation and Isotopes*, 48(10–12):1601–1604, 1997.

[185] M. M. Haque and M. H. Ali. Neutron dosimetry employing soft errors in dynamic random access memories. *Physics in Medicine and Biology*, 39(9):1195–1202, 1989.

[186] J. C. Lund, F. Sinclair, and G. Entine. Neutron dosimeter using a dynamic random access memory as a sensor. *IEEE Trans. Nucl. Sci.*, 33(1):620–623, 1986.

[187] J.L.Davis. Use of computer memory chips as the basis for a digital ALBEDO neutron dosimeter. *Health Physics Society 49^{th} Annual Meeting*, 1985.

[188] G.W. Phillips, R.A. August, A.B. Campbell, M.E. Nelson, J.L. Price, N.A. Guardala, and M. Moscovitch. Feasibility of a neutron detector-dosemeter based on single-event upsets in dynamic random-access memories. *Radiat Prot Dosimetry.*, 101(1–4):129–132, 2002.

[189] B.R. Blaes and M.G. Buehler. SEU/SRAM as a process monitor. In *Microelectronic Test Structures, 1993. ICMTS 1993. Proceedings of the 1993 International Conference on*, pages 57–62, Sitges, Spain, March 1993.

[190] E.G. Stassinopoulos, C.A. Stauffer, and G.J. Brucker. Miniature high-let radiation spectrometer for space and avionics applications. *Nuclear Instruments and Methods in Physics Research A*, 416(2):531–535, 1998.

[191] O. Schroder and T. Schmitz. The application of commercial semiconductor chips for personal neutron dosimetry. *Radiation Protection Dosimetry*, 61(1):9–12, 1995.

[192] O. Schroder, T. Schmitz, and M. Pierschel. Microdosimetric dosemeters for individual monitoring based on semiconductor detectors. *Radiation Protection Dosimetry*, 52(1):431–434, 1994.

[193] Z.W. Bell, M.A. Miller, L. Maya, G.M. Brown, and F.V. Jr. Sloop. Boron-loaded silicone rubber scintillators. *IEEE Transactions on Nuclear Science*, 51(4):1773–1776, 2004.

[194] F. Ravotti, M. Glaser, K. Idri, J.-R. Vaille, H. Prevost, and L. Dusseau. Optically stimulated luminescence materials for wide-spectrum neutron measurements at CERN. *IEEE Transactions on Nuclear Science*, 52(5):1568–1573, 2005.

[195] M. Bliss, R.A. Craig, P.L. Reeder, and D.S. Sunberg. Real-time dosimetry for boron neutron-capture therapy. *IEEE Transactions on Nuclear Science*, 42(4):639–643, 1995.

[196] L. Walker, R. Olsher, G. Cooper, and R. Busch. A modified bonner sphere technique for measuring the high energy neutron spectrum with multiple activation foils. *Health Physics Society 49^{th} Annual Meeting*, 2004.

[197] M. Loughlin, R. Forrest, and J. Edwards. Neutron activation studies on jet. *21^{st} Symposium on Fusion Technology*, 2000.

[198] J. Liu, T. Jenkins, R. McCall, and N. Ipe. Neutron dosimetry at SLAC. Technical Report SLAC-TN-91-3, Stanford Linear Accelerator Center, 1991.

[199] R.A. Noulty H. Ing and and T.C. McLean. Bubble detectors – a maturing technology. *Radiation Measurement*, 27(1):1–11, 1997.

[200] R.A. Noulty H. Ing and, E.T.H. Clifford, J.S. Gamero, and D.R. Cameron. A novel neutron area-monitor based on the bubble detector. *Radiation Protection Dosimetry*, 85(1):101–104, 1999.

[201] F. Vanhavere. The bubble detector for the determination of neutron dose equivalent. Technical Report SLAC-TN-91-3, NPL Belgian Nuclear research Centre SCK-CEN, 2003.

[202] K. Arshak and O. Korostynska. Gamma radiation dosimetry using tellurium dioxide thin film structures. *Sensors*, (2):347–355, 2002.

[203] H. Henschel, M. Korfer, J. Kuhnhenn, U. Weinand, and F. Wulf. Fibre optic radiation sensor systems for particle accelerators. *Nuclear Instruments and Methods in Physics Research A*, 526(3):537–550, 2004.

[204] T.Wijnands and C.Pignard. On-line radiation monitoring in the LHC tunnel and underground areas with SEU counters, RADFETs and PIN diodes. *4th RADWG-RADMON Radiation workshop*, December 2004.

[205] T. Wijnands, C. Pignard, J-C Michelon, A. Tsoulou, and A. Presland. On Line Silicon Dosimeter for LHC Machine electronics. *5th LHC Radiation Workshop at CERN*, 2005.

[206] M. K. Park, G. S. Lee, J. T. Noh, J. Y. Huang, and I. S. Ko. The Interlock System for U7 Undulator in PLS. *1st Asian Particle Accelerator Conference, Japan*, March 1998.

[207] K. A. LaBel. Radiation Effects and Analysis. Technical report, NASA Goddard Space Flight Center, 2000.

[208] M. Dentan. ATLAS TILE CAL Radiation Hardness Assurance. Technical report, CERN, 2002.

[209] R. Katz. A scientific study of the problems of digital engineering for space flight systems, with a view to their practical solution. Technical report, NASA Office of Logic Design, 2005.

[210] B. Mukherjee. Development of a simple neutron irradiation facility with variable average energy using a light water moderated ^{241}AmBe source. *Nuclear Instruments and Methods in Physics Research A*, 363(1):616–618, 1995.

[211] R. C. Baumann and E. B. Smith. Neutron-Induced Boron Fission as a Major Source of Soft Errors in Deep Submicron SRAM Devices. *38th Annual International Reliability Physics Symposium, San Jose, California*, pages 152–157, 2000.

[212] H. P. Chou, T.C. Chou, and T.H. Hau. Evaluation of high density DRAMs as a nuclear radiation detector. *Applied Radiation and Isotopes*, pages 1601–1604, October 1997.

[213] Hans Weise. Introduction to linac 2/PIA and linac. Technical report, Deutsche Elektronen–Synchrotron DESY, 2003.

[214] A. Jaksic, G. Ristic, M. Pejovic, A. Mohammadzadeh, C. Sudre, and W. Lane. Gamma-ray irradiation and post-irradiation responses of high dose range RADFETs. In *Radiation and Its Effects on Components and Systems, 2001. 6th European Conference on*, pages 57–65, 2001.

[215] M. Caffrey, P. Graham, E. Johnson, M. Wirthlin, and C. Carmichael. Single-event upset in SRAM FPGAs. Technical report, National Laboratory, 2002.

[216] P. Alfke. Metastable Recovery in Virtex-II Pro FPGAs. Technical report, Xilinx, 2005.

[217] ACTEL. APA750 and A54SX32A LANSCE Neutron Test Report. Technical report, ACTEL, 2003.

[218] E. Dupont, O. Lauzeral, R. Gaillard, and M. Olmos. Radiation Results of the SER test of Actel, Xilinx and Altera FPGA instances. Technical report, Xilinx and Altera FPGA instances, 2004.

[219] T. Speer, J. J. Wang, B. Cronquist, J. McCollum, and H. Tseng. 0.25 μm FLASH memory-based FPGA for Space Applications. In *Military and Aerospace Applications of Programmable Devices and Technologies Conference MAPLD*, 1999.

[220] J. J. Wang. Radiation Effects in Field Programmable Gate Arrays. In 9^{th} *Workshop on Electronics for LHC Experiments*, 2003.

[221] Synplicity. Designing safe VHDL state machines with Synplify. Technical report, Synplicity, 1999.

[222] A.M. Ougouag, J.G. Williams, M.B. Danjaji, S. Yang, and J.L. Meason. Differential displacement kerma cross sections for neutron interactions in si and gaas. *IEEE Transactions on Nuclear Science*, 37(6):2219–2228, 1990.

[223] C.S. Sims and G.G. Killough. Neutron fluence-to-dose equivalent convertion factors: a comparison of data sets and interpolation methods. *Radiat Prot Dosimetry.*, 5(1):45–48, 1983.

[224] Bubble detector - technical specifications. Technical report, BTI Bubble Technology Industries, October 2005.

[225] B. Mukherjee. Prediction of radiation field characteristics in high energy electron accelerator environment and relevant mitigation strategy for microelectronics. Technical report, Deutsche Elektronen-Synchrotron DESY, 2006.